# A STUDY ON THE EFFECTS OF CEMENTLESS TOTAL KNEE ARTHROSCOPY IMPLANTS' SURFACE MORPHOLOGY WITH FINITE ELEMENT ANALYSIS

A Thesis
Presented to
the Faculty of California Polytechnic State University,
San Luis Obispo

In Partial Fulfillment
of the Requirements for the Degree
Master of Science in Mechanical Engineering

by
Peter Joseph Hunt III
December 2022

COMMITTEE MEMBERSHIP

| | |
|---|---|
| TITLE: | A Study on The Effects of Cementless Total Knee Arthroscopy Implants' Surface Morphology with Finite Element Analysis |
| AUTHOR: | Peter Joseph Hunt III |
| DATE SUBMITTED: | December 2022 |
| COMMITTEE CHAIR: | Mohammad Noori, PhD.<br>Professor of Mechanical Engineering |
| COMMITTEE MEMBER: | Scott Hazelwood, Ph.D.<br>Professor of Biomedical Engineering |
| COMMITTEE MEMBER: | Eltahry Elghandour, PhD.<br>Professor of Mechanical Engineering |

ABSTRACT

A Study on The Effects of Cementless Total Knee Arthroscopy Implants' Surface Morphology with Finite Element Analysis

Peter Joseph Hunt III

Total knee arthroscopy is one of the most performed and most successful orthopedic surgeries, with nearly a million procedures performed in 2020 in the United States alone. Due to changing patient demographics, the use of cementless fixation for implant stability is becoming more prevalent amongst recipients. Cementless implants rely on the surface morphology of a porous coating to bond implant to bone; the quality of this bond is dependent on an interference fit and the roughness, or coefficient of friction, between implant and bone. Stress shielding is a comparison of the properties in implanted bone to natural bone; it is a commonly used measurable when using a finite element model to optimize implant design. The purpose of this study is to investigate how different coating types (coefficients of friction) and the location of their application affect the stress shielding response in the tibia.

A finite element model was constructed to investigate the impact of these variables. The results concluded that the stress distribution in an implanted tibia is dependent on the coefficient of friction applied at the tip of the stem. Lower friction coefficients applied to the stem tip resulted in higher compressive stresses, and higher friction coefficients resulted in lower compressive stresses. Thus, lower friction coefficients provided more favorable stress shielding responses, however, at the expense of stress concentrations of greater magnitude.

# ACKNOWLEDGMENTS

I would like to thank my thesis advisor, Dr. Mohammad Noori, for his continued guidance throughout this study. I am appreciative of the freedom you afforded me to delve into a topic which interested me, because it allowed me to define the research path for this thesis. I'd also like to thank the other members of my thesis committee - Dr. Scott Hazelwood for his advice and assistance interpreting the results of this study, and Dr. Eltahry Elghandour for his suggestions regarding modeling bone. In additional, I'd like to thank Dr. Britta Berg-Johansen, who provided expertise on stress shielding, and put me in contact with Cal Poly alumni Dr. Dimitri Delagrammaticas, who was kind enough to let me visit his operation room to view a knee replacement case.

TABLE OF CONTENTS

Page

LIST OF TABLES

Table Page

LIST OF FIGURES

Figure Page

# Chapter 1: Introduction

Since its formative years in the 1970's, total knee arthroplasty (TKA) has evolved into a multi-billion-dollar industry with nearly a million procedures performed in 2020 in the United States alone [1]. It is one of the most performed and most successful orthopedic surgeries, with most studies reporting 80-100% patient satisfaction [2]. The demand for TKA is increasing exponentially, with a predicted increase in annual procedures by 80% to 2030, and 221% to 2040 [3].

Patient demographics for TKA are trending younger and heavier [4], [5]. These shifts have changed the way implant performance is evaluated, as factors such as increased mechanical stress due to obesity and patient demand to maintain an active lifestyle are key parameters for next-generation TKA implants.

There are two primary methods of fixing an implant – cemented and cementless fixation. Currently in TKA procedures, cemented fixation is considered the gold-standard. However, with the TKA patient demographic transitioning younger and heavier, cementless fixation is growing in popularity as its theoretical advantages mitigate the new risks presented [6]. Cementless implants rely on a porous or roughened surface to promote osseointegration – bone ingrowth into a metal implant. Cementless fixation offers the potential to achieve biologic fixation via osseointegration, which, when present, correlates to a decrease in the likelihood of implant loosening and an increase in survivorship [7].

Aseptic loosening has long been one of the leading complications associated with TKA. Its primary causes include osteolysis, which is the destruction of periprosthetic

bone caused by wear-induced debris, and stress shielding, which is when an implant alters the natural load distribution in bone, leading to decreases in bone density [8], [9]. A reduction of bone tissue or a decrease in bone density can potentially lead to weakened fixation and eventually implant loosening. Mitigating the potential occurrence for both osteolysis and stress shielding is critical in implant design; however, this study will focus on the effects of stress shielding. Thus, the goal of this study is to evaluate different surface morphologies for cementless TKA implants to reduce stress shielding.

## 1.1 Knee Anatomy

The knee is a complex hinge joint whose primary function is to distribute body weight; consequently, it is one of the most stressed joints in the body. As a hinge joint, the knee allows for flexion and extension in the sagittal plane and rotation about the transverse plane. The responsibility of distributing load is achieved in tandem through muscles, ligaments, and joint surfaces [10].

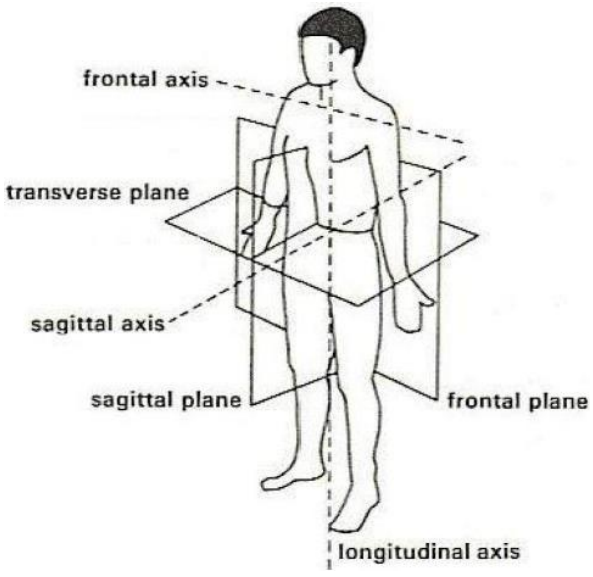


Figure 1.1: The body planes and axes [11].

## 1.2 Bones and Tissue of the Knee Joint

Three bones comprise the knee joint; they are the femur, tibia, and patella. The femur and the tibia primarily support body weight, while the patella provides protection to the joint and aids with ensuring smooth flexion and extension. The bones articulate with each other at joint surfaces (tibiofemoral and patellofemoral joints). The tibiofemoral joint allows for articulation between the femur and tibia, and the patellofemoral joint allows for articulation between the patella and femur.

Soft tissue in the knee helps to stabilize and strengthen the joint. Four main ligaments in the knee connect the bones together; they are the anterior cruciate. posterior cruciate, medial collateral, and lateral collateral ligaments. Tendons attach the two main muscle groups, the quadriceps and hamstrings, to bone.

Articulation at the tibiofemoral and patellofemoral joints is aided by cartilage, which provides a smooth, nearly frictionless surface for the bones to interact with each other. Articular and meniscus cartilage are present in the knee joint. Articular cartilage covers the ends of bones and is found in the knee joint covering the distal end of the femur, proximal end of the tibia, and the posterior side of the patella. There are two menisci in the knee: one on the medial side and the other on the lateral side. They sit at the tibiofemoral joint, filling the gaps between the articular cartilage within the joint. Along with assisting with smooth articulation, the meniscus also increase stability, absorb shock, and distribute load [12].

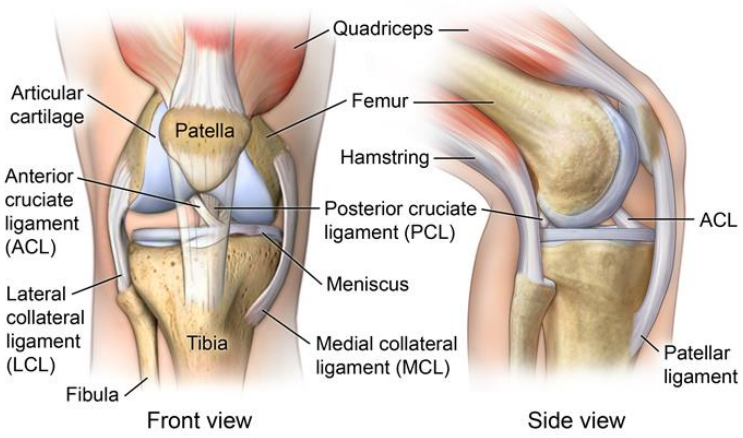


Figure 1.2: The anatomy of the knee [13].

As with all natural biologic materials, bone is a non-homogenous composite, having evolved to provide structural support for organisms. Categorizing bone's mechanical properties is fittingly complex, as its wide functionality crafted a material that is strong, lightweight, and adaptive [14].

Bone tissue can be broken into two types: cortical and trabecular bone. Cortical and trabecular bone is differentiated by large differences in porosity; cortical bone has a porosity in the range of 5% to 15%, whereas trabecular bone has a porosity in the range of 40% to 95% [15]. Cortical bone, the denser of the two, forms an outer layer to surround and protect the spongy, less dense, trabecular bone. Both types of bone are present in the bones of the knee joint.

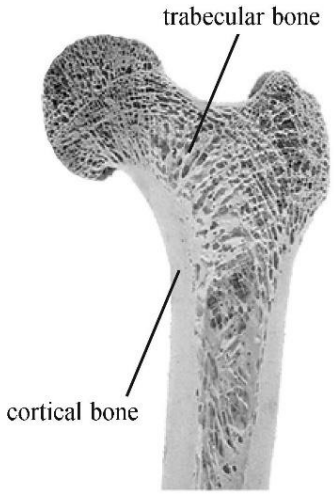


Figure 1.3: Cross-section of the tibia showing the differences in cortical and trabecular bone [16].

Understanding the material properties of cortical and trabecular bone is critical for understanding how bone distributes stress. Cortical bone is anisotropic, with its primary strength being in the longitudinal direction rather than the radial or circumferential direction. Early research indicates that its mechanical properties, such as Young's modulus, ultimate compressive strength, and Poisson's ratio, are related to porosity and mineralization [15]. Trabecular bone, like cortical bone, exhibits anisotropic behavior. Additionally, its mechanical properties are governed by porosity; however, the arrangement and individual properties of trabeculae also contribute to its properties [15].

## 1.3 What is TKA?

The primary indication for TKA is primary, end-stage, tri-compartmental osteoarthritis (OA) [17]. This is a degenerative joint disease where the articular cartilage that protects bones from each other is worn down such that there is bone-on-bone contact. The symptoms of late-stage arthritis are chronic and debilitating; common indicators

include pain, inflammation, and joint instability. Although infrequent, other diagnosis associated with TKA include inflammatory arthritis, fracture (post-traumatic OA and/or deformity), dysplasia (abnormal growth), and malignancy [17].

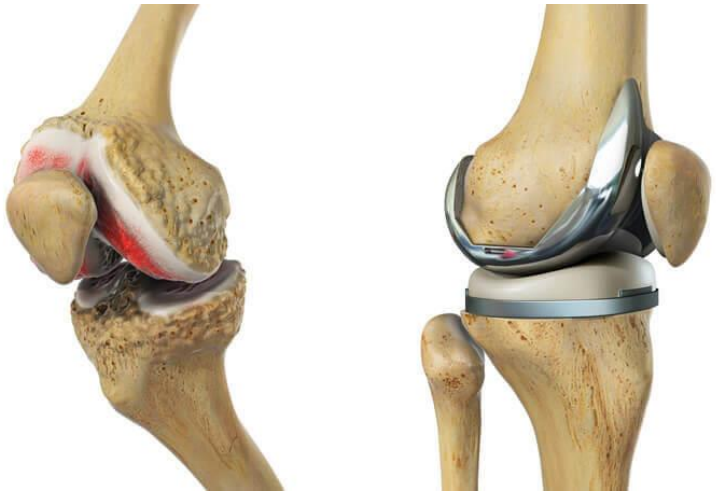

Figure 1.4: Knee with osteoarthritis (left) compared to knee with TKA implant (right) [18].

The objective of TKA is to relieve knee pain by replacing damaged areas within the knee joint. This has long been accomplished with a prosthetic implant, first pioneered in the 1890's when Theophilus Gluck developed a hinged, ivory implant fixed to bone with plaster of Paris [19]. However, it wasn't until the 1970's that a suitable design for the commercialization of TKA was developed.

Since the breakthroughs of the 70's, TKA has enjoyed wide clinical success and commercial profits; there are hundreds of models available to patients. The TKA implants of today vary by design philosophy, material, shape, method of fixation, and which bones of the tibiofemoral joint to resection. Selection of the proper implant involves careful evaluation of the patient, the implant's clinical record, surgeon

familiarity with a specific implant, and cost. All these factors are gauged with the intent of providing the patient with the best knee function and long-term survivability.

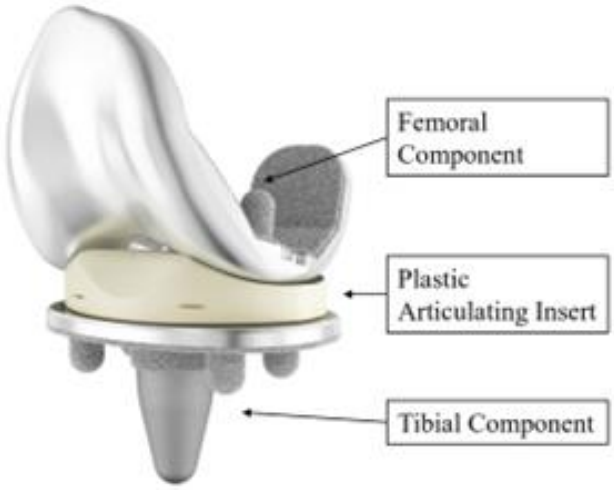


Figure 1.5: Components of a TKA implant. Note that there is no patellar component in this model [20].

## 1.4 Revision TKA

In the event of failure or unsatisfactory performance, revision TKA may be required. A clinical study analyzing the causes for revision TKA found that the most common indications for revision are aseptic loosening followed by infection, with the mean patient age being 72.3 years old and mean time from primary surgery to revision being 5.5 years [21]. Importantly, the revision risk for patients over 70 years of age is low and is reported to be around 5% [22]. Revision TKA does not boast of the favorable outcomes that the primary surgery does. Revision TKA is substantially more difficult because the surgeon must remove the defective implant from the patient, thus raising the risk of complications and making outcomes difficult to predict. It is reasonable to expect that function and survivability will be inferior to that of the primary surgery [23].

## 1.5 Changing Patient Demographics

Patient demographics of TKA recipients have notably shifted in recent years. Once predominately limited to elderly patients, it is projected that by 2030, 55% of all TKAs will be implanted in patients younger than 65 years old [22]. There are many factors contributing to this change - a growing population, increased stresses in the knee resulting from both high levels of obesity and a more active general population, and expanding indications and patterns for treatment may all be viewed as possible explanations for the growing number of TKA recipients in their middle years.

Additionally, younger TKA patients are more likely to require revision surgery than their older counterparts. A 2017 study by Bayliss et al. revealed concerning survivability data amongst younger TKA recipients, finding that males between the ages of 50-59 had a lifetime risk of revision around 35% [24]. The increase in the risk of revision for younger patients can be associated with several factors; alarmingly, aseptic loosening has been shown to be the dominant indicator of revisions within the younger TKA patient population [25]. Thus, younger patients battle two fronts against aseptic loosening – it is already the leading cause of revision and is even more prevalent in the younger age group. It is crucial that modern implant design must account for the new needs of the younger patient demographics.

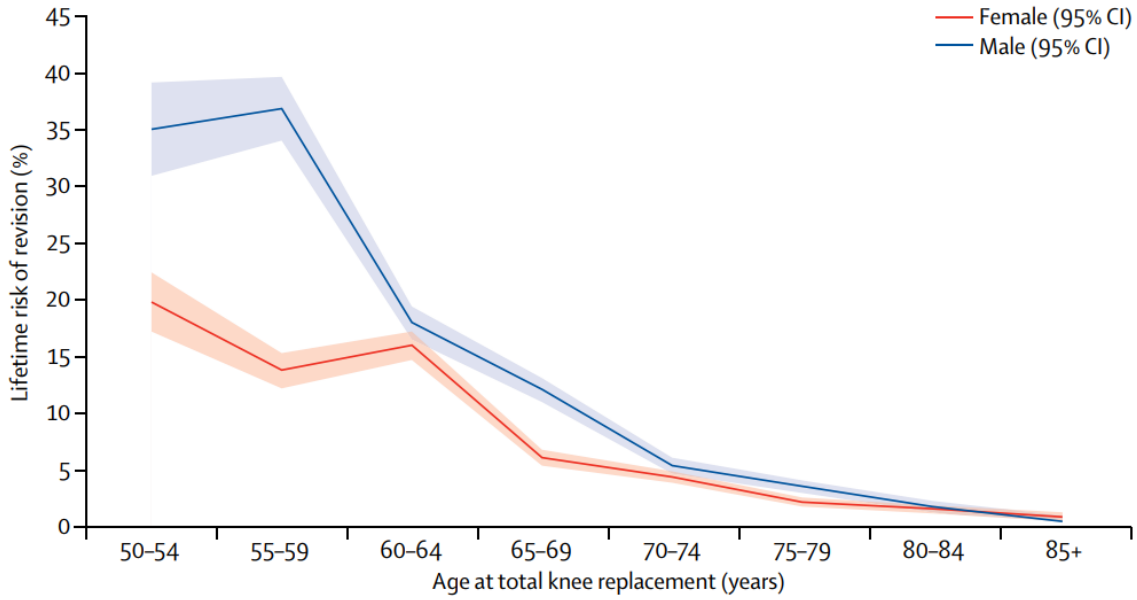


Figure 1.6: Lifetime risk of revision for TKA recipients, separated into 5-year age groups by sex [24].

## 1.6 TKA Procedure

The goal of TKA is to replace damaged components in the knee joint to relive knee pain or improve knee function. Some of the key surgical steps include resectioning the femur, tibia, and sometimes the patella, sizing the resectioned surfaces with trial implants, and finally cementing or press-fitting each component to the resectioned surfaces. These key steps are repeated across all TKA procedures, with variation in each process due to patient needs, surgeon preference, and design intent. TKA surgery usually requires between one to three hours to complete, and recovery is dependent on the individual, although most patients can resume normal activities within 6 weeks of operation.

## 1.7 Fixation Types

As mentioned, current TKA implants differ by design philosophy, material, shape, fixation type, and which bones to resection. The most pertinent design consideration to address the younger and heavier patient demographics is component fixation. There are two primary methods of fixing an implant to bone – cemented and cementless fixation. The debate between the better of these two modes of fixation has been ongoing for decades.

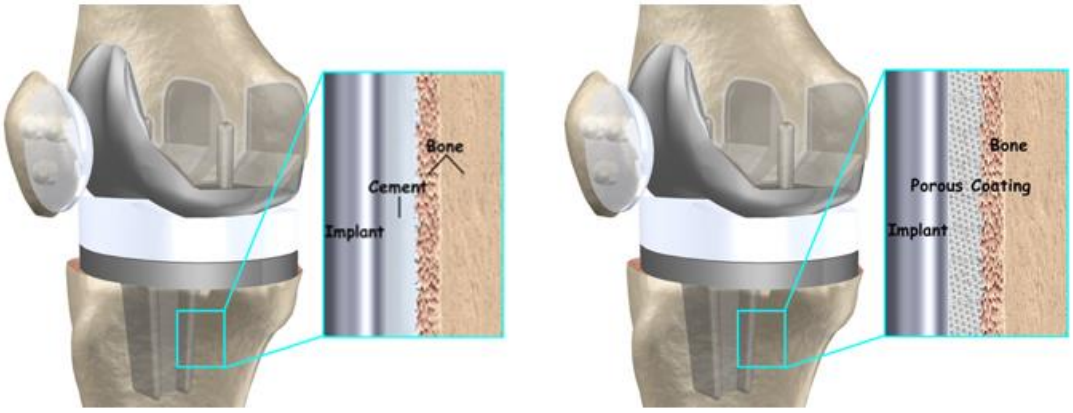


Figure 1.7: Cemented fixation (left) and cementless fixation (right) [26].

### 1.7.1 Cemented

Cemented fixation set the standard for TKA, as it has been in use since its inception. Due to its established effectiveness, it is still the dominant method of fixation. It is accomplished by using a biomaterial to fix the implant to the bone, providing stability by filling the space between bone and implant and providing strength by mechanical interlock of cement to bone and implant.

The demands of the cement are twofold. First, the cement must be strong enough to transfer load. Second, the cement must have a high fatigue strength to support

survivability. The most common material used to meet these demands is polymethyl methacrylate (PMMA).

The clinical history of cemented implants is robust, but there are disadvantages of cemented fixation. Chiefly, the presence of bone cement presents a risk of osteolysis as degradation of the cement can cause particle release. It can be broadly stated that any mechanical failure of the bone cement can ultimately lead to osteolysis and subsequently, aseptic loosening.

### 1.7.2 Cementless

Despite the success of cemented implants, cementless implants have managed to stay relevant due to the potential to achieve biologic fixation. Biologic fixation aims to bond the implant to bone natural via osseointegration – where the bone grows into the implant. Biologic fixation's primary potential benefit is to limit the chances of developing aseptic loosening, thereby increasing survivorship. Other additional benefits of cementless implantation include preservation of bone stock, shorter operative times, ease of revision, and a reduction in the risk of cement degradation and particle release [27].

Cementless fixation is achieved by a porous or roughened surface to promote osseointegration. The altered surfaces are present on specific portions of the implant which are in contact with bone, allowing the matrix structure of bone to grow into and mesh with the implant. To encourage osseointegration, hydroxyapatite (HA) coating is used in most applications and provides a biocompatible surface to enhance bone ingrowth.

Cementless fixation is not without its disadvantages and questions. Namely, it is more expensive than cemented implants, and may only be applicable to patients with appropriate bone quality. Many early studies on cementless TKA were bearish on its ability to achieve the high positive outcomes boasted by cemented fixation; however, more recent studies have reported competitive short-term and mid-term survivorship in comparison to cemented results. As the most recent generation of cementless implants have not been around long enough for the collection of long-term data regarding their outcomes, it remains to be seen if cementless implants will be able to replicate the clinical track record of its cemented counterparts. However, cementless implants have carved out a share in the implant market and will be an important tool as the number of TKA procedures continues to rise.

As developments of cementless implants are relatively recent, there remain questions about its design. One of the topics under debate is the ideal design of the tibial baseplate and the selection of porous surfaces. The discussion of the ideal tibial baseplate revolves around its geometry, as features such as symmetry, stems, keels, and pegs are all present and varying in commercially available TKA implants. Similarly, the porous surfaces vary by surface type, pore size, location on the implant, and properties such as coefficient of friction and porosity.

### 1.8 Primary and Secondary Fixation

Implant to bone fixation can also be described as primary and secondary fixation. Primary fixation is often described as the mechanical method of fixing the implant to bone. For cemented implants, the cement provides the mechanical interlock between implant and bone and is stable as soon as the cement has cured, which usually takes

between 10-20 minutes [28]. For cementless implants, primary fixation is based on a press-fit of the implant into bone and the frictional properties of the surface coating [29]. Additionally, cementless implants require suitable primary fixation, as it is a prerequisite to achieving secondary fixation.

Secondary fixation refers to osseointegration, or as previously mentioned, biologic fixation. Its affects are most prominent for cementless implants, where the method of the mechanical interlock between implant and bone gradually changes from press-fit to bone in-growth facilitated by osseointegration [30]. Achieving biologic fixation takes time and is on the order of months. During the gap of time between primary and secondary fixation, the implant is not fully stable, leaving risk for failure due to aseptic loosening. To improve and speed up the process of biologic fixation, recent developments include increasing porosity of the coating, reducing elastic modulus, and increasing the coefficient of friction [31]. If perfect osseointegration is achieved, the bone and implant are assumed to be rigidly bonded to each other, allowing no relative motion, reducing the relevancy of the coefficient of friction [32]. For this reason, this study will only consider an implant before biologic fixation has occurred.

### 1.9 Aseptic Loosening

Historically, aseptic loosening has been one of the primary failure methods of TKA implants [33]. Aseptic loosening is mainly the result of osteolysis and stress shielding; these effects can destroy and degrade bone [9]. Therefore, reducing the risk of the occurrence of osteolysis and stress shielding is paramount in implant design.

### 1.9.1 Osteolysis

Osteolysis is the destruction of periprosthetic bone at the implant-bone or cement-bone interface. It is the result of wear-induced debris; these microscopic particles are associated with wear of the cement or the plastic articulating insert. Without treatment, osteolysis can progress to aseptic loosening and ultimately implant failure.

Although predominately caused by wear, particle release can also be attributed to micromotion or contamination [34]. When particles are present in proximity to the implant, an anti-inflammatory response is triggered, forming fluids and membranes. The presence of these fluids and membranes can cause bone resorption and deterioration; this biologic process is osteolysis. Essentially, the body's pathologic response to particles weakens the surrounding bone, undermining implant fixation and causing loosening.

Osteolysis is relevant to both cemented and cementless implants since both implant types include a plastic insert, often constructed of polyethylene [33]. However, since cementless implants do not use bone cement, there is less inherent risk of osteolysis.

Due to its relationship with component wear, osteolysis can be viewed as a shortcoming in manufacturing. From this viewpoint, the primary culprit of osteolysis is the polyethylene insert. A 2018 review of the failure methods of total knees included an analysis of failures related to polyethylene degradation, reporting that improvements to polyethylene production decreased the frequency of failures due to polyethylene wear and subsequent osteolysis [33].

### 1.9.2 Stress Shielding

Stress shielding is a mechanical phenomenon which occurs in periprosthetic bone due to a difference in stiffness between the implant and bone. It occurs when an implant alters the natural progression of load transferred in bone, and results in a reduction in bone density, which can lead to weakened implant fixation [35], [36]. The stress shielding effect is relevant to both cemented and cementless implants.

Alteration of the load distribution through bone results in localized increases or decreases in force. When bone experiences a decrease in applied force, it begins to resorb, as the body no longer sees a need to keep the bone. This results in weakened bone of decaying density, potentially leading to weakened fixation and implant loosening.

Another term associated with bone resorption is turnover. Turnover is the process of creating new bone – resorption gets rid of old bone and replaces it with new bone. Due to its low density and proximity to bone marrow and blood flow, trabecular bone has a faster turnover rate than cortical bone [37]. Thus, due to its higher turnover rate, trabecular bone is more susceptible to the effects of stress shielding.

Stress shielding is quantified by comparing the conditions in post-operative bone to the conditions in non-prosthesis bone and can be calculated with a variety of different measures, including von Mises stress, principal stress, strain energy, and density. Since stress shielding is a mechanical measure and the objective of this study is to evaluate different types of surface morphologies, stress shielding will be selected as the evaluation criteria.

## 1.10 Numerical Methods of Measuring Implant Performance

Computer-based finite element models (FEMs) have been utilized to help guide implant design by simulating the stress and displacement in the bone-implant system. Finite element analysis (FEA) is a numerical technique of modelling complex geometry and loads to analyze systems from a static, non-linear, and heat perspective, among other fields. It incorporates the properties of the materials in the model, and if they are homogeneous, non-homogeneous, isotropic or anisotropic. In implant design, FEMs are usually rigid bodies, with the implant being homogeneous and the bone being modeled as either homogeneous, non-homogenous, or isotropic. Often used measurables in implant FEMs are micromotion (motion of implant relative to bone), stress concentrations, and stress shielding.

## 1.11 Intention of this study

The increasing number of younger patients undergoing TKA is raising the risk of revision due to aseptic loosening. Cementless fixation offers the potential to achieve biologic fixation via osseointegration, which, when present, correlates to a decrease in the likelihood of implant loosening and an increase in survivorship. To achieve biologic fixation, it is necessary to achieve suitable primary fixation, which is dependent on factors such as the press-fit and frictional properties of the coating. Cementless fixation is a viable option to address the changing TKA patient demographics, but questions remain about its long-term outcomes, and there is no continuity on the ideal cementless implant design.

There are many unknowns associated with cementless TKA, and therefore the scope of this study will be limited to the design of the tibial component of the implant.

Specifically, the goal of this study is to evaluate different surface morphologies for cementless TKA implants to reduce stress shielding prior to achieving biologic fixation. To do so, ABAQUS will be used to create a FEM simulating a TKA procedure, and a material property comparison study will be conducted to examine how the coefficient of friction of the TKA implant surface coatings and its location effect the stress distribution in the tibia.

# Chapter 2: Background Review of Methodology to define Model Parameters

This chapter will provide an overview of cementless TKA implants and a review of critical parameters to better understand and rationalize the methods utilized for successful development of a TKA FEM.

## 2.1 Current Commercially Available Cementless TKA Implants

This section will discuss some of the commercially available cementless TKA implants, such as DePuy Synthes' Attune Cementless Knee System, Stryker's Triathlon Tritanium, and Zimmer's NexGen Complete Knee Solution. All three of these implants are specifically designed for cementless fixation. Implants that are not specifically designed for cementless fixation, such as DePuy Synthes' Sigma Total Knee, Stryker's Triathlon, and Zimmer's Persona will not be discussed as an analysis of cementless fixation is the objective of this study.

### 2.1.1 DePuy Synthes: Attune Cementless Knee System

Johnson & Johnson's orthopedic company, DePuy Synthes, was founded in the 1890's and is one of the world's leading orthopedic businesses. Its flagship primary knee system is the Sigma Total knee system, and is the most implanted TKR in the world, backed up by a lengthy track record of positive clinical results [27]. The Attune Knee System platform integrates some of the lessons and technologies from previous knee solutions and is one of the largest research and development projects in the history of DePuy Synthes. The Attune Cementless knee system is an addition to the family of Attune Knee Systems, and was developed in response to a younger, more active patient who would benefit from the effects of cementless fixation [28].

The Attune Cementless implant employs J&J's patented Porocoat porous coating to encourage biologic fixation. This coating is applied to the femoral and tibial components. The tibial component is selectively coated with Porocoat - the bottom of the baseplate, the proximal end of the central cone, and the entirety of four pegs, are coated. The tibial baseplate is made of Co-Cr and is 4.0 mm thick [29].

Figure 2.1: DePuy Synthes Attune Cementless [20].

### 2.1.2 Stryker: Triathlon Tritanium

The Tritanium is the latest edition to Stryker's Triathlon Total Knee System portfolio; the Triathlon family of implants has been implanted in over 3 million patients to date [38]. The Tritanium was specifically designed in response to the patient demographics for TKA trending younger and heavier; thus, the Tritanium utilizes cementless fixation. The Tritanium incorporates much of the Triathlon's geometric profile; the primary difference in form between the two models is the Tritanium's addition of four cruciform pegs on the tibial baseplate. Additionally, specific locations of

the Tritanium are coated with Stryker's proprietary 3D printed porous coating technology. This porous structure, which is called Tritanium (and is the namesake for the implant), is constructed of layered titanium powder and applied to the femoral, patellar, and tibial components. The underside of the tibial baseplate, the proximal end of the keel, and the proximal end of each of the cruciform pegs are coated with the porous material [39]. Additionally, the tibia baseplate is constructed of titanium [40].

Figure 2.2: Stryker's Triathlon Tritanium [39].

### 2.1.3 Zimmer: Persona Knee Solution

The Persona family of knee solutions is Zimmer Biomet's flagship knee replacement system. The Persona was designed to be a 'personalized' implant – designed for optimal fit and function to improve patient satisfaction. Rather than a specific cementless model, Zimmer designed the Persona to be versatile such that components are interchangeable. The cementless version of the Persona incorporates the Trabecular Metal Technology, which allows for biologic fixation.

Zimmer's Trabecular Metal Technology is a highly porous biomaterial constructed of tantalum that approximates the mechanical and physical properties of bone [41]. It is the only material used in orthopedics which boasts a modulus of elasticity similar to bone [42]. Unlike the previous porous materials, the Trabecular Metal is not a coating, which allows for a greater amount of ingrowth and an increase in implant stability.

The tibial baseplate geometry of the Persona does not include a central cone or keel, and there are only two hex-shaped pegs on the underside of the baseplate. The geometry of the Persona greatly differs from the geometry of the Attune and Tritanium implants.

Figure 2.3: Zimmer Persona Knee [42].

## 2.2 Bone Model

As stress shielding is a dependent measure of the change in conditions in bone, it is critical that bone's materials properties are correctly assigned. Bone is a non-

homogeneous structure consisting of cortical and cancellous bone. Both types of bone are anisotropic, meaning that the material properties vary depending on the direction.

There are several assumptions authors have made in determining the material properties of bone necessary for a finite element model. Particular disparity exists between capturing the true non-homogeneous and anisotropic behavior of bone. However, it has been well established that bone can be modeled as a linear elastic material [43]–[45].

In a study by Yueh (2020) on the effect of stress shielding in the tibia due to implant design parameters, the bone model was significantly simplified. The tibia was modeled as linear elastic, isotropic, and homogenous, and was assigned material properties consistent with cortical bone; cancellous bone was neglected [46]. Rationale for this bone model was that the goal of this study was to analyze the magnitude of the stress shielding relative to configurations with differing design parameters; therefore, obtaining accurate measurables was not critical. A similar study conducted by Completo et al. (2009) modeled the tibia as linear elastic, isotropic, and homogenous; however, both cortical and cancellous bone were present in the model [44].

A study by Jia et al. (2017) to evaluate the optimal tibial stem length and material modeled bone as linear elastic, isotropic, and non-homogeneous [45]. The non-homogeneity of cancellous and cortical bone modeled the material properties as a function of the apparent density. A CT scan of the left tibia of a 35-year-old male was used to determine the density distribution in the tibia, and empirical equations were used to relate the Young's modulus to the apparent density, creating a mapping of the Young's

modulus throughout the tibia. In this method, cancellous and cortical bone are present in the model, appearing as functions of the apparent density.

Au et al. (2005) created a FEM of the tibia to study periprosthetic stresses [43]. The tibia model included both cortical and cancellous bone, and both types of bone were assumed to be linear elastic, orthotropic, and non-homogeneous. The bone was divided into volumetric blocks, which were assigned specific material properties for different types of bone. In total, twenty-five different materials were defined to represent the non-homogeneous cortical and cancellous bone.

Accurately representing the material properties of bone is a non-trivial but crucial part of creating a relevant FEM. An overarching study by Baca et al. (2008) aimed to compare several different bone material models used for FE analysis on "global" and "small" domains of the femur [47]. The bone material models were: (i) isotropic homogeneous (IH), (ii) isotropic inhomogeneous (IIH), and (iii) orthotropic inhomogeneous materials (OIH); all models assumed that bone was linear elastic. The IH and IIH models were compared to the OIH model because the OIH model most realistically captures the behavior of bone. The study found that the best bone material model for the "global" domain was the IIH model, and for the "small" domain, the OIH model.

## 2.3 Stress Shielding

Stress shielding can be found experimentally and analytically through FEMs. Common methods of experimentally measuring stress shielding involve direct strain measurements of cadaver bones and radiographic imaging to determine changes in bone mineral density (BMD) [48], [49]. Many different methods of quantifying stress shielding

have been implemented for FEMs. Two separate models created to study stress shielding in shoulder arthroplasty defined stress shielding as the change in compressive strain and relative density [50], [51]. Two independent FEMs which analyze stress shielding in hip arthroplasty defined stress shielding as the change in von Mises strain and strain energy [52], [53]. Models for knee arthroplasty have defined stress shielding as the difference in the principal stress [43], [44], [46] and the difference in bone density [54].

The disparity in methods of determining stress shielding in FEMs is due to the differences in the construction of the bone model. In homogeneous bone models, such as the studies conducted by Yueh (2020) and Completo et al. (2009), strain and stress are used to calculate stress shielding since the density of bone is modeled as a constant [44], [46]. In non-homogeneous bone models, the density of bone is a function, allowing for stress shielding to be quantified by the change in non-prosthesis and implanted bone density [45], [51].

As stated previously, stress shielding is commonly evaluated in trabecular bone because its impacts are enhanced in trabecular bone. Despite this, there is disparity between published FEMs about which bone type stress shielding should be computed in. A study by Completo et al. (2009) evaluated stress shielding in only trabecular bone [44]. Studies by Au et al. (2005) and Jia et al. (2017) measured stress shielding in both trabecular and cortical bone [43], [45]. Finally, a study by Yueh (2020) evaluated the stress shielding in just cortical bone [46].

## 2.4 Bone Implant Interface

For cementless implants, primary fixation is achieved by the press-fit between bone and implant and on the frictional properties of the implant surface [55]. Press-fit fixation

is attained in the surgical procedure, where bone is drilled with dimensions slightly smaller than the external dimensions of the implant, thus compressing the surrounding bone. To prepare the tibia for the insertion of the tibial component, the holes for the keel, cone, and pegs are drilled slightly smaller than the geometry of the implant. It is commonly believed that a larger interference fit increases the fixation; however, if the interference is too great, it may cause inadvertent damage to the bone. Therefore, it is important that each implant design has an acceptable range of interference fits [56]. Experimentally, values of interference fit have ranged from 0.2 – 1.6 mm [56]. For reference, the tibial component of Johnson & Johnson's Sigma PFC knee implant has a nominal interface fit of 0.75 mm [57].

The porous coating which creates the frictional behavior between bone and implant serves two purposes. First, it helps to postoperatively stabilize the implant, and is an aid in achieving primary fixation. Second, the porosity, which is an input to determining the coefficient of friction, provides a structure and a favorable medium to encourage bone ingrowth and osseointegration. As coating is applied to select regions of the implant, the frictional behavior must be considered for coated and uncoated surfaces. A study by Damm et al. (2015) demonstrated that the coefficient of friction depends on the type of coating and the magnitude of contact stress [32]. However, FEM and experimental studies often treat the coefficient of friction as a constant, an assumption made for ease of integration into the FEM [44], [57], [58].

## 2.5 Loading

The loading of the tibia is dictated by the anatomy of the knee. The knee is a complex hinge joint whose loading is equally complex; its six degrees of freedom

accounting for axial, shear, and moment loads [59]. A popular method of determining the loading conditions of the knee is gait analysis. While walking, loads are transferred through several muscles, ligaments, and joint surfaces [10].

The largest of the knee forces occurs at the tibiofemoral joint, whose primary responsibility is to transmit body weight from the femur to the tibia [59], [60]. Load transfer at the tibiofemoral joint is split amongst the medial and lateral compartments of the knee [61]. A study by Fukubayashi and Kurosawa (1980) laid the groundwork for modeling the contact area and pressure distribution for the medial and lateral tibiofemoral loads [62]. This study was conducted with the knee fully extended and found that the contact area and pressure distribution is non-uniform, dependent on the magnitude of the applied load. A more recent study by Zhao et al. (2007) reported on the in-vivo medial and lateral contact forces under gait, step up/down, lunge, and kneel activities, concluding that there was a consistent load split of approximately 55% medial and 45% lateral across all test conditions [61].

Numerous gait analyses have quantitively described the joint contact forces provided by the tibiofemoral joint. Morrison's benchmark study on the mechanics of the knee joint (1970) found that the maximum total joint force at the tibiofemoral joint ranged from 2.06 to 4.0 times body weight, with an average value of 3.03 times body weight [10].

A review of the loading conditions employed by several FE models of the knee reveals the predominant assumptions. The loads applied at the knee vary; some models consider the muscle, ligament, and joint loads [45], while others only consider the joint load [36], [43], [44], [46]. Zhao et al.'s work allows for the medial and lateral pressure

distribution to be modeled as a uniform or point load; this method is more widely used than the non-uniform distribution described by Fukubayashi and Kurosawa due to its simplicity. There is also consensus on the magnitude of the joint load; values around 2000N are commonly used [36], [44], [46].

# Chapter 3: Literature Review

This section will detail clinical, experimental, and FE results related to surface morphologies of cementless TKA implants. The rise of cementless implants has been buoyed by an influx of available literature; however, due to the recency of its ascension, there are numerous holes and opportunities for novel research to be conducted.

## 3.1 Clinical Results

Clinical trials offer the best method of verifying whether a design is satisfactory or not. Until recently, clinical results for the postoperative performance of cementless implants was unsatisfactory compared those of cemented implants; however, advances in technology to the highly porous surfaces have demonstrated favorable short and mid-term results for cementless implants.

One of the earliest clinical studies to report positive results on cementless implants was published by Park and Kim in 2011. They attempted to determine if there was a statistically significant difference in the long-term performance of cemented and cementless implants by randomly assigning a cemented or cementless implant to a cohort of 50 patients. Between 1997 and 1998, patients randomly received a cemented or cementless Zimmer Biomet NexGen prosthesis. Patient follow-up was conducted at an average of 13.6 years postoperatively and included a patient questionnaire to measure pain and function, and a measurement of ability to complete range-of-motion exercises. Park and Kim found no statistically significant difference in the scores between the cemented and cementless components, providing one of the first comprehensive studies which concluded with satisfactory cementless implant results [63].

Rather than these results being conclusive proof of the viability of cementless fixation, Park and Kim's study provided a spark to reignite interest in cementless fixation. The NexGen implant used in their study has been surpassed with current technological improvements, and currently, the clinical results pertinent to the newest generation of cementless implants are beginning to be published.

A 2019 study by Nam et al. compared the clinical outcomes of cemented and cementless versions of the same TKA design. Patient satisfaction scores were collected using several orthopedic scoring methods to measure pain and function at 4-6 weeks, 1 year, and 2 years postoperatively. Their study found that there was no statistically significant difference in the satisfaction scores at any of the postoperative evaluation dates, and that one revision procedure was performed in the cemented cohort, and no revisions were performed in the cementless group [64]. Nam et al. concluded that the short-term satisfaction and survivability of cementless implants are equivalent to those of cemented implants.

Similarly, a 5-year satisfaction and survivability study by Fricka et al. published in 2019 compared the outcomes for cemented and cementless TKA implants. Between 2010 and 2012, 100 participants under the age of 75 were randomly assigned to receive a cementless or cemented implant. At 5-year follow up, patients completed a questionnaire on satisfaction, pain, and function, and an independent surgeon analyzed and scored radiographs. The outcomes of the study found that survivorship, satisfaction, and radiographic findings did not differ by a statistically significant amount, thus demonstrating equivalent performance between cemented and cementless implants at a 5-year follow-up [27].

At this point in the cycle, there has not been enough time to document any long-term results for the current generation of cementless implants. These long-term studies should be available within a few years, and the short-term and mid-term results provide a reason to be excited about the prospects of obtaining positive long-term results for the newest editions of cementless TKA implants.

## 3.2 Experimental Data

The scope of the clinical trials analyzed is far broader than the scope of this thesis; there are no clinical studies which compare the performance of coating location and type applied to a cementless implant. However, several studies have reported experimental findings on different characteristics of cementless implants' surface morphologies which effect primary fixation.

It is well-established that achieving postoperative primary fixation is dependent on the interference fit and coefficient of friction [32], [55], [65], [66] . These parameters are related - theoretically, larger interference fits should lead to higher compressive forces which allow for higher frictional forces. Consequently, higher friction forces would correspond to larger coefficients of friction. A study by Damm et al. (2015) aimed to determine the coefficients of friction between various types of titanium surface morphologies and femoral trabecular bone during press-fit implantation using nominal interferences fit based off clinical data. Damm reported the results of the friction coefficient as a function of the interference fit and the normal stress, providing an empirical relationship between the characteristics of an interference fit and the magnitude of the coefficient of friction. Damm concluded that there is a balance between the two parameters, bound by the notion that an undersized interference fit may not provide

enough frictional forces to achieve primary fixation, and that an oversized interference fit can lead to permanent bone deformation [32].

The succeeding literature reviewed primarily focuses on determining an optimal friction coefficient for coated surfaces to achieve primary fixation. Like Damm's study, the effects of the friction coefficient are typically studied on the femur, as the position of the femoral component causes it to bear more frictional forces than the tibial component.

A cadaveric study by Berahmani et al. (2014) aimed to evaluate the performance of a new highly rough and porous surface structure developed by DePuy Synthes. Cadaveric femurs were implanted with the new and control surface morphologies and compared on their ability to provide primary fixation strength, measured by the force required to loosen the implant. Berahmani found that the novel surface morphology induced a 40% greater average loosening force compared to the control, concluding that the novel surface morphology achieved superior primary fixation and attributed that to higher frictional resistance [65].

Berahmani's finding that a higher coefficient of friction provided superior primary fixation is in line with the theoretical hypothesis. These results are also backed up by other experimental studies, such as a study by Vries' et al. (2022), which stated that it is a necessity to improve implant stability by increasing the roughness of implant surfaces. However, neither study provides explicit guidance on exactly what the higher coefficient of friction should be. It is likely that there is a biocompatible bound on the magnitude of the friction coefficient related to minimizing bone fraction, bone abrasion, and permanent bone deformation.

## 3.3 Numerical Results

There is a limited amount of published FEM's related to the parameters of cementless surface morphologies; however, there are abundant FEM's on TKA implants, several which measure stress shielding as the output.

A study by Post et al. (2022) investigated the optimal values of the interference fit and coefficient of friction for the femoral component of a TKA implant constructed of a novel polyetheretherketone (PEEK) material. To determine which configuration provided the best primary fixation, micromotion and interface gaps were measured, and the performance of the cementless implant cohort was compared to a cementless CoCr implant. Bone was modeled as being a non-homogenous elastic material, and was meshed using tetrahedral elements with a seed size of 2.5 mm. The coefficient of friction was defined on three values – low ($\mu = 0.5$), average ($\mu = 1.0$), and high ($\mu = 1.5$). The interference fits were taken in a range from 250 to 1000 μm to represent common and extreme values. Post concluded that the PEEK femoral component generates higher micromotions and interface gaps compared to the CoCr femoral component when equal interference fits and friction values were applied. However, increasing the interference fit and coefficient of friction for the PEEK design resulted in similar micromotions found with the standard CoCr design [67]. This conclusion agrees with the experimental results obtained by Berahmani and Vries because decrease in micromotion means less relative motion between the implant and bone, a favorable outcome in achieving primary fixation [65], [66].

The succeeding literature reviewed covers sources of tibial stress shielding related to the design parameters of the tibial component of TKA implants. Controversial results

and conclusions are common and may be attributed to wide variation in the methods used to construct the FEMs.

Material selection of the implant has been a particularly controversial topic regarding mitigating tibial stress shielding. Previously, it was thought that the primary contributing factor to stress shielding was the difference in Young's modulus between the implant and bone. This school of thought was disproved by Au et al. in 2007. Au created a FEM with non-homogenous cortical and trabecular bone, meshed with 2-mm, 10-node tetrahedral elements. Young's modulus was varied, and stress shielding was calculated using Von Mises stress at locations along different paths starting at the resectioned plane and moving distally along the tibia (the resectioned plane is the cut plane on the proximal end of the tibia where the tibial component is placed). Au concluded that the Young's modulus mismatch alone is not a sufficient predictor of stress shielding – instead, that stress shielding relies on other parameters, such as the loading condition, loading pattern, and implant-condylar surface geometry [54].

The results of Au's study greatly influenced following studies, as it opened the door for stress shielding to be evaluated on other tibial component design parameters, particularly related to implant geometry. Completo et al. (2009) assessed stress shielding and stress concentrations for titanium and CoCr implants with long and short stems. This study utilized a FEM including linear elastic, isotropic, and homogeneous trabecular and cortical bone, and PMMA bone cement. Similar to Au, stress shielding was calculated distally along the femur; however, stress shielding was calculated with the minimum principal stress at cut planes parallel to the resectioned plane. Completo concluded that the geometry of the implant had a more pronounced effect on stress shielding relative to

implant material, finding that short stems produce minor stress shielding and stress concentration effects compared to longer stems.

Similar to Completo, Jia et al. (2017) investigated the tibial stem length and material to determine the optimal design of the tibial stem to best mitigate stress shielding. Jia modeled three groups of stem lengths and four types of material. The FEM used to analyze this system made use of a CT scan of the tibia to model bone as a non-homogenous material by creating a mapping of the Young's modulus. This method of modeling bone most accurately captures the behavior of bone, and is a significant advancement in assigning bone properties in comparison to the methods used in Au and Completo's studies. However, despite the differences in the bone models, Jia concluded that long stems produced more pronounced stress shielding and stress concentrations than the short stem, in line with the results reported by Completo. But in contrast to Completo's results, Jia found that stem material had a larger impact on stress shielding than stem length; however, this result can be explained by a difference in materials analyzed between the two studies [45].

Another study conducted by Yueh (2020) compared how fixation technique, stem geometry, cement stiffness, and interface condition affected the stress shielding within the tibia. Yueh's FEM modeled bone as being entirely cortical, linear-elastic, isotropic, and non-homogenous. In regard to stem length, Yueh found that stress shielding was present all the way from the resectioned surface to the stem tip, a divergence from the results reported by Completo and Jia [46]. Yueh found that cement stiffness did not have a significant impact on stress shielding, but cemented fixation, in comparison to cementless, induced more stress shielding. The latter result is particularly controversial,

as it is expected that a cementless implant would incur larger stresses on the surrounding bone. However, Yueh assumed that the cementless implant was fully bonded to bone, which indicates that secondary fixation had been achieved and thus the relevance of frictional and interference fit parameters would be diminished.

### 3.4 Holes in Published Literature

Cementless implants have carved out a space alongside cemented implants in the orthopedic prosthetic market, and they will be an important tool in the coming years as the number of TKA procedures increases. Short and mid-term clinical trials for patient satisfaction and survivability has demonstrated comparable results between cemented and cementless implants. Although long term results for the newest generation of TKA implants are currently unavailable, within a few years, long-term clinical results comparing cemented and cementless implants will be published as the patients age.

It has been established that a higher coefficient of friction makes for better primary fixation. Current research on cementless implants is focused on determining the optimal interference fit and coefficient of friction to achieve primary fixation by studying the response in femoral bone.

Limited FEM studies are available on the effects of surface morphology; however, the sole resource analyzed by Post arrived at the conclusion that a higher coefficient of friction improved primary fixation. There is a plethora of FEM related to mitigating stress shielding through design parameters of the tibial component of a TKA implant; in general, it is accepted that a shorter stem reduces stress shielding, but other conclusions are hard draw due to the controversial results reported.

There are significant holes in the literature in regard to the purpose of this study. First, there are no clinical studies published which primarily focus on the properties of surface morphologies of cementless implants. The experimental studies referenced emphasize optimizing primary fixation in the femur – there are no studies which analyzed the relationship between surface morphology and stress shielding, and furthermore, there are no studies investigating the behavior of stress in the tibia when implanted with a cementless implant. Despite the abundance of stress shielding FEMs, there is a scarcity of FEMs related to cementless implants. To the author's knowledge, there is no previous work which has analyzed how the surface morphologies of cementless implants affect stress shielding in post-operative tibial bone prior to achieving biologic fixation.

# Chapter 4: Method

This section will detail the steps taken to create the FEM utilized in this study. As detailed in the steps below, the tibia was pre-processed in MeshLab, processed in SolidWorks, and analyzed in ABAQUS.

a. A part file of a cementless tibial component was created in SolidWorks. This model was adapted from the geometry of DePuy Synthes' Attune Cementless Knee System.
b. An *.stl* of an adult tibia was imported into MeshLab for simplification and creation of the trabecular bone. Operations such as closing holes, smoothing surfaces, and simplifying geometry were conducted to improve the quality of the tibia's geometry. MeshLab exported two *.stl* files: a refined mesh of the full tibia, and a refined mesh of the tibial trabecular bone, created by offsetting the full tibia by 3mm.
c. The two refined *.stl* files were imported to SolidWorks. A part file for the cortical bone was created by subtracting the trabecular bone from the full tibia. Once both bone part files were created, the intact and resectioned tibia assemblies were created.
d. Both tibia assemblies were imported to ABAQUS as *.STEP* files.
e. The material properties were defined and assigned to the tibia and implant.
f. Interactions were defined to simulate the physical relationship between parts in the system.
g. The load and boundary conditions were defined.

h. A convergence study for the intact and resectioned tibias was completed to determine an appropriate seed size.

Key assumptions and the corresponding rationale will be described. Note that hydroxyapatite coating is not included in this model because it is not a structural component of a TKA implant.

## 4.1 Implant Development

The geometry of the implant for this study was based on DePuy Synthes' Attune Cementless Knee System. As stated, this TKA implant is specifically designed for cementless fixation, making it qualified for incorporation to this study.

Although detailed drawings of the Attune's geometry were unavailable, other studies and a sales aid released by Johnson & Johnson provided snippets of the implant's geometry. Digging through other studies found that the tibial baseplate is 4.0-mm thick, and the taper angle of the pegs is 1.72° [56], [68]. Photographs from the sales aid depicted that the pegs were 10-mm long, with a radius of 6-mm [69]. Additionally, the sales aid provided a frontal view of the implant geometry, which was imported to SolidWorks as a sketch, allowing for completion of a part file of the implant.

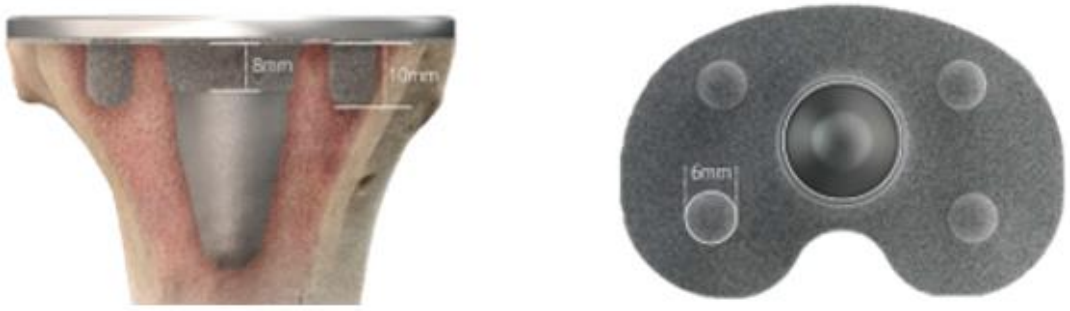


Figure 4.1: Photographs of Attune which provided dimensions used to assist the creation of the implant part file [69].

The implant part file was saved as a *.STEP* file for later importation to ABAQUS. To reduce the complexity of the part and to ease subsequent analysis in ABAQUS, all fillets were removed from the part. The final geometry of the implant used in this study is shown in Figure 4.2 below.

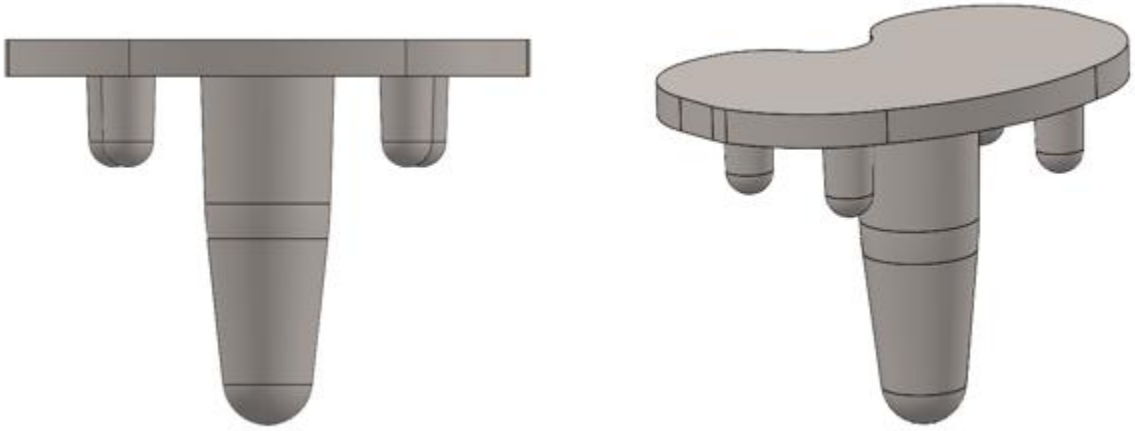

Figure 4.2: The final geometry of the implant used in this study.

## 4.2 Tibia Mesh Simplification and Creation of Trabecular Bone

An *.stl* file of an adult tibia was obtained from a previous study by Yueh (2020) to serve as the basis for the FEM. Initial importation of the tibia to SolidWorks was unsuccessful due to the complex geometry of the tibia – nearly 3 million faces were present in the tibia's original state. Thus, the tibia model required significant modification to simplify its geometry. This process was facilitated by MeshLab.

MeshLab is an open-source software for processing and editing 3D triangular meshes. Its utility for this study was to simplify the unstructured mesh of the original *.stl* file of the tibia, allowing for exportation to SolidWorks.

Upon importation to MeshLab, a quality check was run and determined there were several zero-volume elements. These elements were removed and filled via the "close holes" command. To minimize the number of faces, the "Isotropic Explicit Remeshing" command was run, and the target length of the vertices set to 3.5 mm. By increasing the length of the vertices, the number of faces decreased. Finally, the command "HC Laplacian Smooth" was run to smooth the vertices and faces. MeshLab reduced the number of faces from nearly 3 million to about 4000.

MeshLab was also used to create the trabecular bone as SolidWorks was unable to offset or shell the tibia due to the complex geometry and number of faces. Reported values of tibial cortical wall thickness range from 2-5mm [70]. For this study, the cortical bone was assumed to have a uniform thickness of 3mm to ease the modeling of the trabecular bone in MeshLab.

To create the trabecular bone, the “Uniform Mesh Resampling” command was used on the full tibia (seen in Figure 4.3 below) to create a new tibia with a 3mm offset inward – this 3mm inward offset corresponds to the assumption of a uniform 3mm cortical wall thickness. Then, the “Isotropic Explicit Remeshing” algorithm was used to set the target length of the vertices to 3mm, and finally, the command “HC Laplacian Smooth” was ran to remove any irregularities in the geometry.

Both the full tibia and trabecular bone tibia were exported as *.stl* files for further modification in SolidWorks.

Figure 4.3: The tibia before (left) and the cortical (center) and trabecular (right) tibias after mesh simplification in MeshLab.

## 4.3 Creation of Cortical Bone

The simplified *.stl* files were exported from MeshLab into SolidWorks. Once in SolidWorks, the cortical bone was created by subtracting the trabecular tibia from the full tibia.

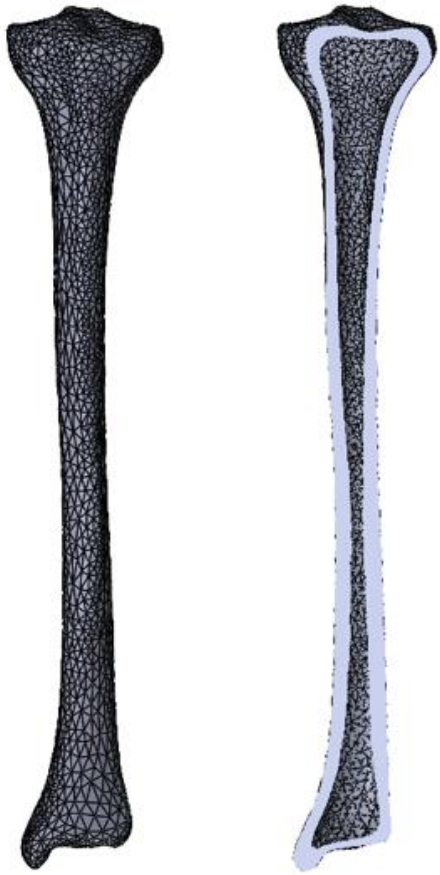

Figure 4.4: The cortical bone part file.

An assembly containing the part files for cortical and trabecular bone was created to mate the parts together and to ease subsequent modifications. To reduce computational effort and allow for easy application of boundary conditions in the succeeding ABAQUS analysis, the tibia was cut at approximately 192mm from the proximal end, as guided by St. Venant's principal.

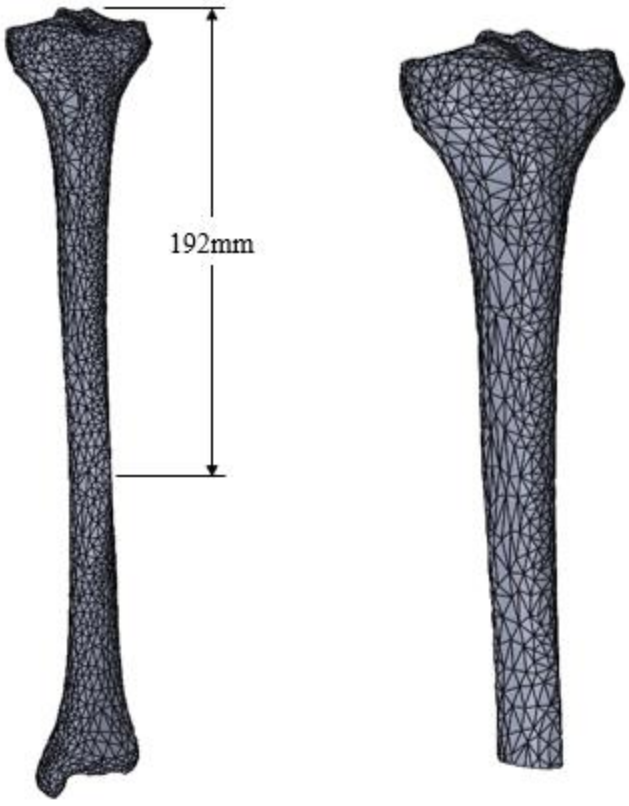


Figure 4.5: The tibia assembly prior to the mid-tibial cut (left) and the tibia after the mid-tibial cut (right).

## 4.4 Tibial Configuration

As stress shielding is a comparison between non-implanted and implanted bone, two different tibia models were constructed. These models will be differentiated as follows: the non-implanted tibia is designated as the intact tibia, and the implanted tibia is designated as the resectioned tibia.

### 4.4.1 Intact Tibia

The intact tibia serves to model the stress conditions in non-implanted tibial bone. After creation of the assembly with both trabecular and cortical bone part files (seen in Figure 4.5 above), no further modifications were required; the assembly was exported to ABAQUS as a *.STEP* file.

### 4.4.2 Resectioned Tibia

Creating the resectioned tibia required several additional steps. First, the tibia was resectioned at a length of approximately 10.5mm, which is in accordance with the geometry of the implant, recommendations from Johnson & Johnson's published surgical guide for the Attune Cementless Implant, and a range of resection depths reported by Berend (2010) [71], [72]. The tibial posterior slope (slope of the resectioned cut) was set to 3°, as recommended by the Attune Surgical Guide. The tibial posterior slope ensures that the anterior portion of the resectioned plane is higher than the posterior section, which anatomically helps to balance the ligaments.

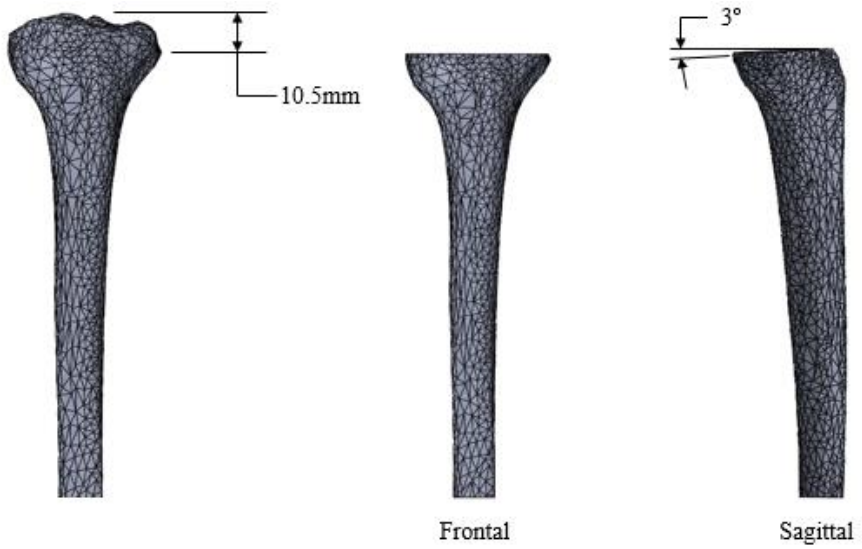


Figure 4.6: The tibia prior to the resectioning cut (left) and the tibia after the resectioning cut as viewed in the frontal (center) and sagittal planes (right).

Next, the implant part file was added to the assembly. The “cavity” command was used to subtract the geometry of the implant which resides in the bone, as seen in Figure 4.7 below.

Figure 4.7: The resectioned tibia with bone appropriately removed to seat the implant.

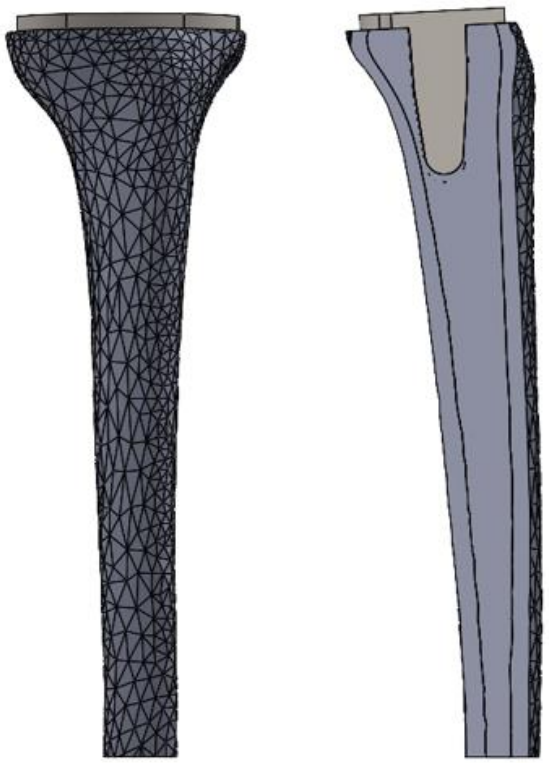

Figure 4.8: The right tibial assembly, front (right) and section view (left)

The final SolidWorks assembly of the resectioned tibia is shown in Figure 4.8 above. In the medical field, implant positioning is widely discussed and there are several different schools of thought. Factors such as ligament balancing, kinematic alignment, ligament retention, implant model, and fixation method are all variables for a surgeon to consider when positioning an implant. As stated previously, this study resections the tibia to a depth of 12.5 mm at 3° about the coronal plane. Additionally, this model assumes that there is no rotation about the sagittal plane – there no varus or valgus knee alignment. It is important to note that the assumptions made regarding the implant positioning align with the available literature; however, these values differ for individual cases.

Furthermore, the cross-sectional view of the tibia as seen from the sagittal plane was visually compared to post-operative x-ray images of Attune implants to obtain a general location for the implant stem. From the x-ray images analyzed, alignment of the implant stems' range from centered to shifting in the posterior direction. As the implant modeled in this study leans in the posterior direction, this comparison gives confidence that proper alignment has been achieved. As seen in Figure 4.9 below, the x-rays and model show visual agreement of location of the stem when viewed from the sagittal plane.

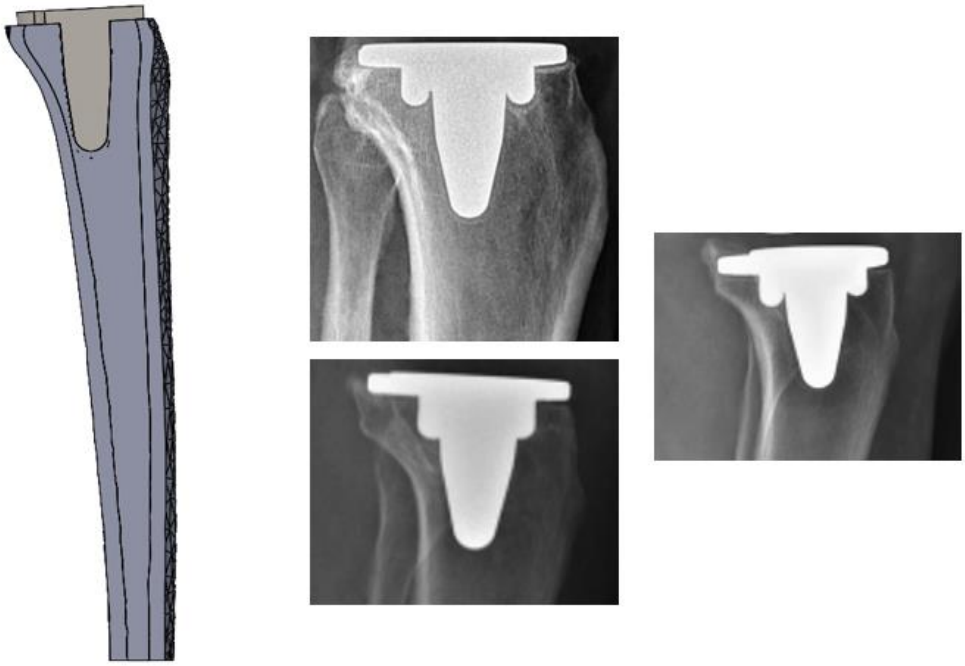

Figure 4.9: Visual comparison of implant alignment in the sagittal plane [73], [74].

## 4.5 ABAQUS

The implant, and intact and resectioned tibias were exported to ABAQUS as *.STEP* files. Once imported, all parts were scaled by a factor of 0.001 to convert

millimeters to meters to work in standard SI units. Construction of the FEM included assembling the parts, assigning material properties, creating interactions, applying loads and boundary conditions, and developing the mesh.

### 4.5.1 Material Properties

Critical to the creation of an adequate FEM is the assigning of material properties. Stress shielding is a measure of the conditions in bone; thus, it is critical that the bone be modeled as accurately as possible to replicate bone's in-vivo load mechanism. However, bone is a notoriously difficult material to model due to its variability across specimens, and due to difficulties in capturing its viscoelastic, orthotropic behavior and its complex non-homogenous structure.

The material properties of bone were greatly simplified in this study. Both trabecular and cancellous were modeled as linear-elastic, homogeneous, and isotropic to simplify the problem.

The linear-elastic assumption has been utilized in many different bone FEMs [43], [44], [46]. Although cortical and trabecular bone exhibit viscoelastic properties, assuming linear-elastic behavior is a reasonable approach, as evidenced by Rho's (1996) ultrasound study on measuring the elastic properties of human tibial bone [75].

The non-homogeneous behavior of bone is often modeled by obtaining a CT scan of the tibia which can be used to create a map of the bone density by relating the Hounsfield value to density. Youngs' modulus is known to be a function of bone density, which is used to create a distribution of Youngs' modulus in bone [45]. This method of creating a non-homogeneous model of the tibia is far more realistic but also far more time

consuming than a homogeneous model. Therefore, to simplify the bone model, both trabecular and cortical bone were considered to be homogeneous.

Modeling cortical and trabecular bone as being isotropic is another assumption made to simplify the problem. A study by Schuster and Krone (2006) to determine suitable material anisotropy for FEM of the human femur concluded that an isotropic model – rather than a more complex anisotropic model - was sufficient to predict the bending response of bone [76]. Additionally, a linear-elastic model of bone allows it to be defined by only two independent elastic parameters.

The rationale for modeling bone as linear-elastic, homogeneous, and isotropic is to simplify the bone model. Despite these simplifications straying from the real behavior of bone, these assumptions have been widely used in bone FEMs, and additionally, are validated by studies such as Rho's (1996) and Schuster's (2006).

Material property assignment for the implant was much simpler. The implant is modeled out of titanium, which is linear elastic, isotropic, and homogenous. The assumed material properties for the implant, and trabecular and cortical bone are shown in Table 4.1.

Table 4.1: Material Properties of Components in FEM [44], [47].

| Component | Material | Young's Modulus | Poisson's Ratio |
|---|---|---|---|
| Implant | Titanium | 110 GPa | 0.3 |
| Trabecular Bone | - | 1.75 GPa | 0.3 |
| Cortical Bone | - | 14.2 GPa | 0.3 |

### 4.5.2 Interactions

Interface conditions were used to create the interactions between the implant, and trabecular and cortical bone part files. To prevent any relative motion between the trabecular and cortical bone, a tie constraint was assigned to the contacting surfaces between the trabecular and cortical bone parts. Critically, the properties of the porous coated surfaces were captured by defining an interaction property creating a surface-to-surface interaction between the implant and contacting bone surfaces.

Physically modeling the porous coated surfaces in ABAQUS would require the discretization of the pores' microstructure. This would require an enormous number of nodes and elements, which would be computationally impossible given the computing power of ABAQUS' academic version, which is limited to 250,000 elements. Therefore, the properties of porous coated surfaces were distilled down to their coefficient of friction, and modeled using ABAQUS' Coulomb friction definition.

The coefficients of friction for some of the commercial coatings were provided in a study by Berahmani et al. (2015) and the Stryker sales guide for the Tritanium, shown in Table 4.2 below. The reported coefficients of friction all fall within a range of 0.5 to 1.4, giving confidence that these are the bounds of the coefficients of friction utilized by industry.

Table 4.2: Coefficients of Friction for Porous Coatings.

| **Coating Name** | **Coefficient of Friction** |
|---|---|
| Grit Blasted | 0.5 [56] |
| Tritanium | 0.92 [77] |
| Porocoat | 0.95 [56] |
| DePuy Synthes Experimental | 1.4 [56] |

It is important to consider the frictional interaction between the uncoated implant surfaces and bone. Damm's work on determining an empirical relationship between coefficient of friction and press-fit implants produced plots as seen in Figure 4.10 [32]. This plot shows that the coefficient of friction for polished titanium on bone is dependent on the normal stress; its practicality to this study is that it allows for calculation of the coefficient of friction. In this study's FEM, the applied force has a total magnitude of 2400 N (its development will be discussed in the next section), and acts on the proximal face of the tibial baseplate, which has an area of approximately 1780 $mm^2$. This results in a normal stress of nearly 1.35 MPa, which corresponds to a friction coefficient of 0.15. Thus, uncoated regions of the implant were assigned a coefficient of friction equal to 0.15.

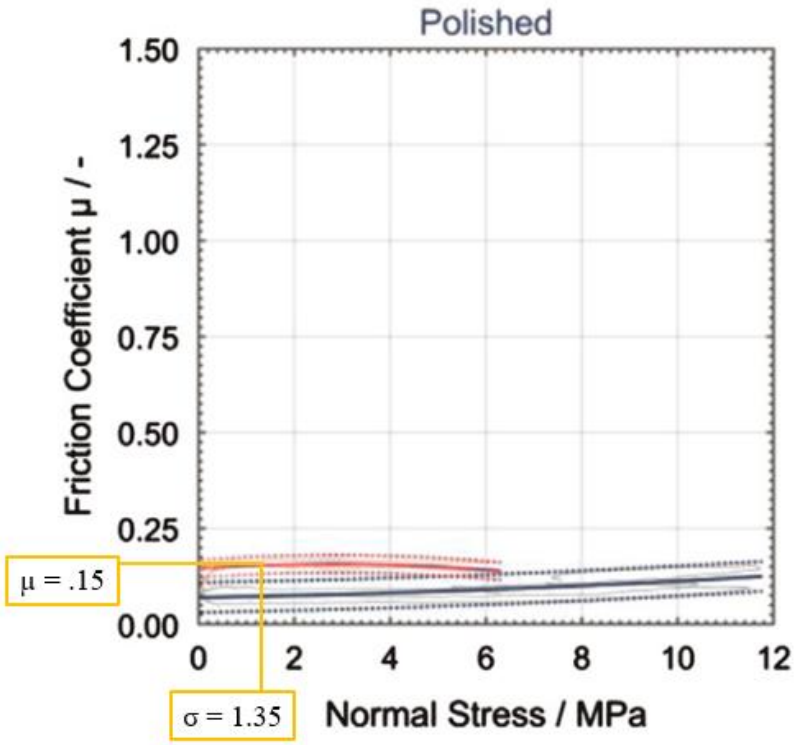


Figure 4.10: Results of Damm et al.'s study; it was used to cimpute the coefficeint of friction for uncoated surfaces of the implant [32].

The coefficients of friction were input to ABAQUS as a contact interaction property behaving in the tangential direction. To apply the porous coating to the implant, a surface-to-surface contact interaction was created, allowing the coefficient of friction to govern the motion between the implant and bone surfaces.

Although primary fixation is also a function of the interference fit, the interference fit was not included in this study. The linear-elastic material properties assigned to bone would create an unrealistic model of the system because the contact forces would linearly increase as interference fit increases [78]. Incorporation of an interference fit into the model would result in unreasonably high stresses in the bone [32],

[78]. Thus, to preserve model accuracy given the assumptions made for the material properties of bone, the fit between the bone and implant was assumed to be perfect.

### 4.5.3 Load and Boundary Conditions

The loading of the knee joint is complex due its anatomy, with loads being transferred through a number of muscles, ligaments, and joint surfaces. However, the largest of these tibiofemoral loads occur at the medial and lateral condyles, and because of their magnitude compared to other loads, these were the only forces considered. To simplify the application of these forces on the implant, it was assumed that the leg was fully extended so that the loads were purely axially compressive. Additionally, the maximum force at the tibiofemoral joint averages about 3 times body weight [10]. Therefore, a 2400N force was set as the maximum loading condition, which corresponds to the average North American's weight of about 82kg (180lb) [79].

As previously stated, the total tibiofemoral load is non-uniformly split between the medial and lateral condyles. Additionally, the load at each condyle is non-uniformly distributed over a contact area. A study by Zhao et al. (2007) concluded that there was a consistent 55% medial and 45% lateral tibiofemoral load distribution; these breakdowns were used in this study to define 1320 N and 1080 N as the medial and lateral loads, respectively [61].

The non-uniform pressure distribution present at each condyle was simplified to be uniform. The final step in defining the load was sizing and locating the contact area. This was a crucial component of creating the FEM, as the location of the load had substantial effects on the force and subsequently the stress distribution, as it greatly affected the neutral axis.

The results of a study by Fukubayashi and Kurosawa (1980) were used to size and locate the contact area. Their results included photographs and tables of the contact area for knees with and without the menisci under varying loads up to 1000 N [62]. The need for TKA often arises due to osteoarthritis; thus, the data for contact area without a meniscus was used as it represents worst-case osteoarthritis.

First, the size of the contact area was determined using tabulated data obtained from Fukubayashi and Kurosawa's study. Because Fukubayashi and Kurosawa did not experiment with loads greater than 1000 N, their raw data had to be extrapolated to approximate the contact area under a 2400 N load. When subjected to the 2400 N load, the contact area was approximately 4.1 $mm^2$ and 3.1 $mm^2$ at the medial and lateral condyles, respectively, as shown by Figure 4.11.

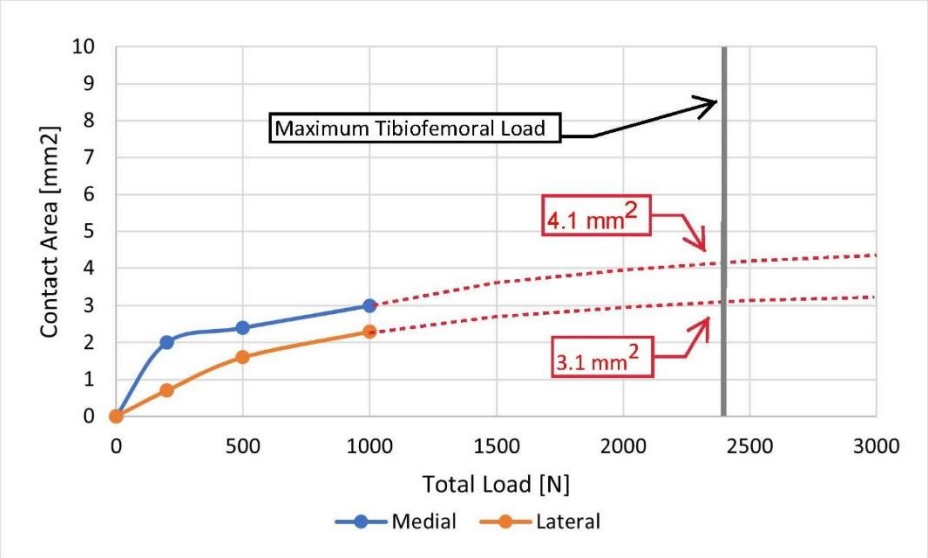


Figure 4.11: Extrapolation of the data provided by Fukubayashi and Kurosawa to determine the size of the contact area [62].

The location of the contact area was determined by overlaying photos of the contact area from Fukubayashi and Kurosawa's study on corresponding photos of the intact and resectioned tibia.

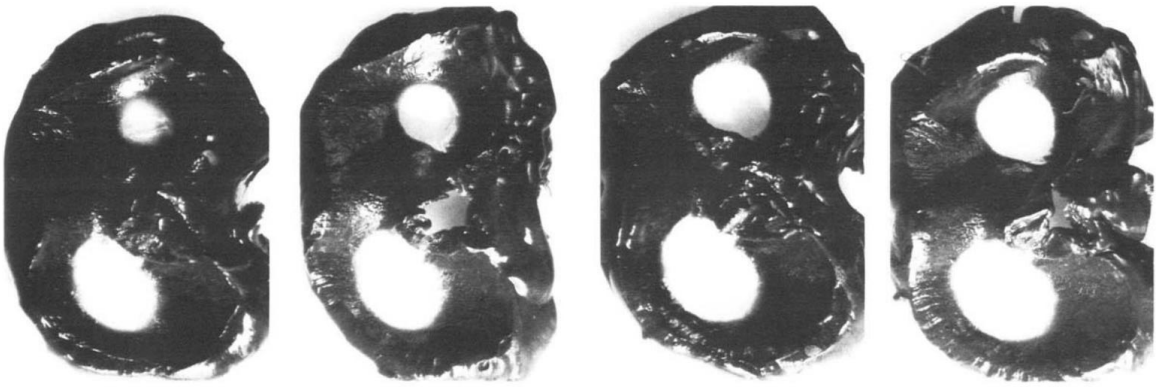

Figure 4.12: Photographs of the boundaries of the contact area without the menisci as reported by Fukubayashi and Kurosawa [62].

The contact areas shown in Figure 4.12 above were used to identify the centroid of the contact areas. The centroid of the contact area was denoted as a star and transcribed to the intact and resectioned tibias in Figure 4.13 below to identify the location of the load. The contact areas were assumed to be circular based on the photographs in Figure 4.12.

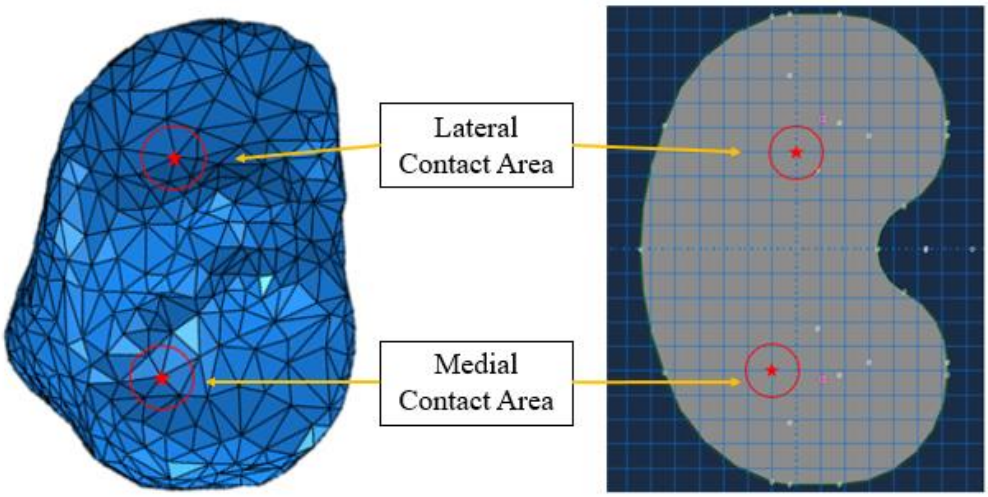


Figure 4.13: The location of the contact area for the intact (left) and resectioned (right) tibias.

Finally, the distal cut surface of the tibia was assigned a fixed boundary condition to prevent any movement or rotation.

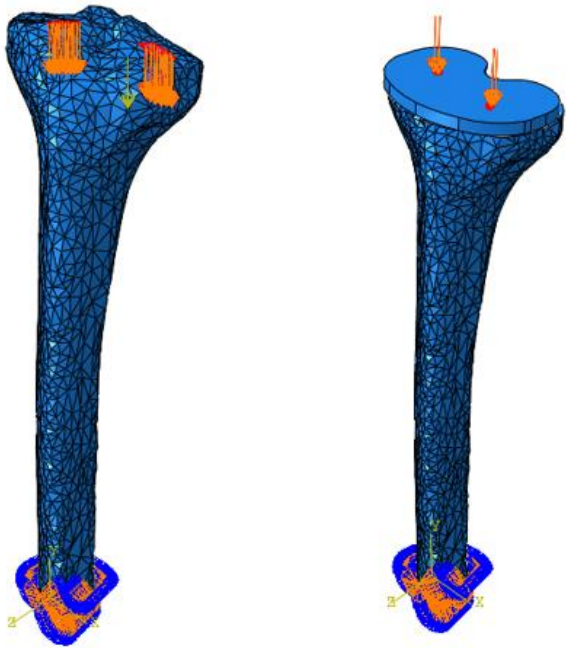

Figure 4.14: Intact (left) and resectioned (right) tibias with the associated loading and boundary conditions.

### 4.5.4 Mesh Development

Both the intact and resectioned tibia assemblies were meshed using ABAQUS' built-in free meshing technique. To mesh the parts, 10-node tetrahedral C3D10 elements were selected due to their proficiency with complex geometry. Additionally, C3D10 elements have been used in several other published implant FEM studies providing further evidence that they are a suitable choice.

As there are multiple parts within each assembly, each part required its own convergence study to determine an appropriate mesh size. This was accomplished by varying the seed size for one part and keeping all other parts at a consistent seed size. The maximum, minimum, and stress at a specific point of interest were recorded for the part undergoing seed size variation. Convergence was defined when all three of these measures fell within 5% of the previous results.

The intact and resectioned tibia assemblies each required their own convergence studies due to the large differences in geometry. The dominant source of the geometric differences between the two assemblies is the addition of the implant to the resectioned tibia assembly.

#### 4.5.4.1 Intact Tibia Convergence

The results of the convergence study for the intact tibia are tabulated in Table 4.3 and displayed in Figure 4.15. Note that the stress results have been normalized to better depict the simultaneous convergence of the minimum, maximum, and point of interest stress. The final meshed intact tibia assembly is shown in Figure 4.16 below; note that the

vertical red dashed line indicates the degrees of freedom corresponding to convergence. See Appendix A for additional info on the intact tibia convergence.

Table 4.3: Overview of the Mesh Characteristics for Parts in the Intact Tibia Assembly.

| **Part** | **Number of Elements** | **Degrees of Freedom** | **Seed size [mm]** |
|---|---|---|---|
| Trabecular Bone | 49980 | 220956 | 2.05 |
| Cortical Bone | 55143 | 265842 | 2.175 |

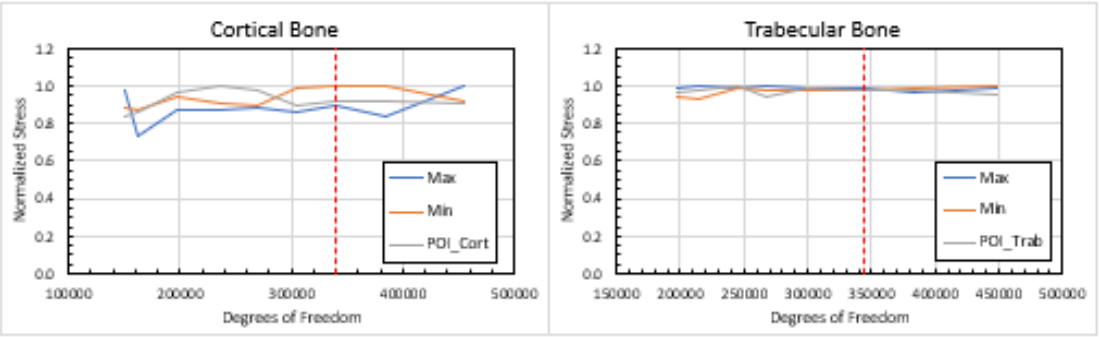


Figure 4.15: Convergence results for the parts in the intact tibia assembly.

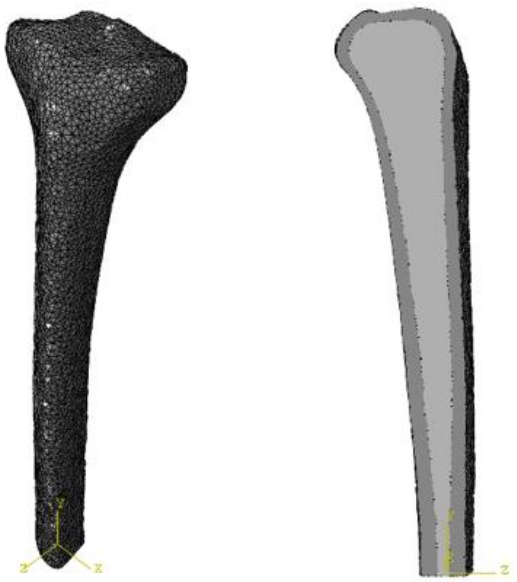

Figure 4.16: The fully-meshed intact tibia assembly.

#### 4.5.4.2 Resectioned Tibia Convergence

The results of the convergence study for the resectioned tibia are tabulated in Table 4.4 and displayed in Figure 4.17. Note that the stress results have been normalized to better depict the simultaneous convergence of the minimum, maximum, and points of interest stresses. The final meshed intact tibia assembly is shown in Figure 4.18 below. See Appendix B for additional info on the resectioned tibia convergence.

Table 4.4: Seed Sizes for Parts in the Resectioned Tibia Assembly.

| **Part** | **Number of Elements** | **Degrees of Freedom** | **Seed size [mm]** |
|---|---|---|---|
| Trabecular Bone | 35099 | 160725 | 2.175 |
| Cortical Bone | 23885 | 122016 | 2.175 |
| Implant | 11685 | 57102 | 2.25 |

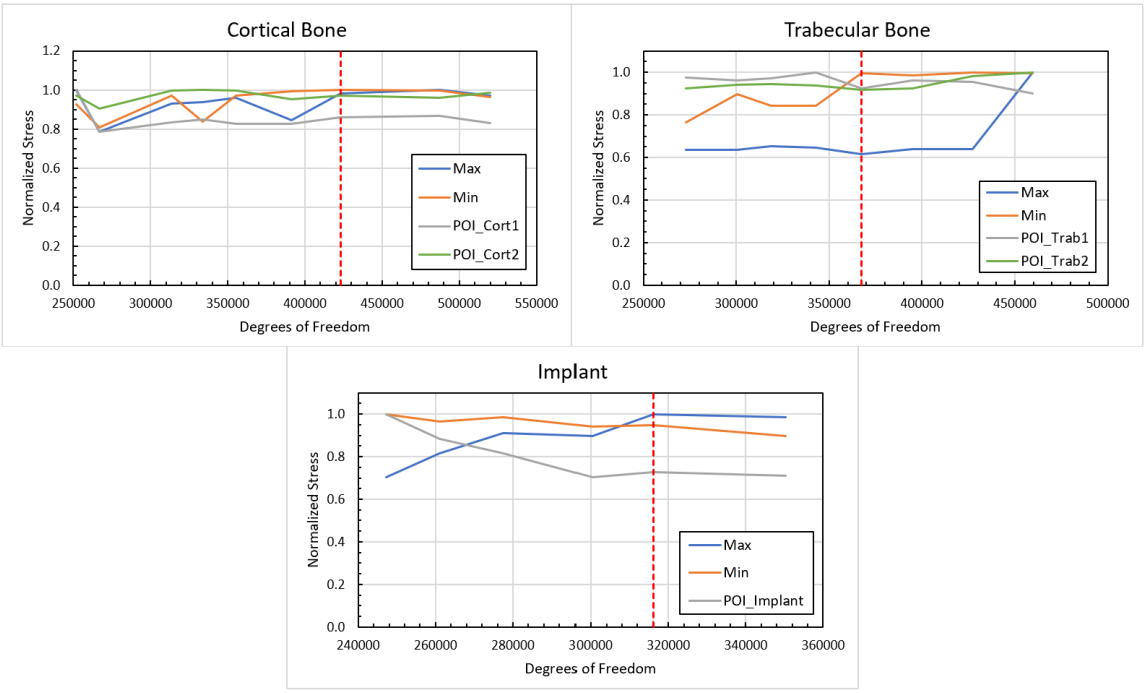


Figure 4.17: Convergence results for the parts in the intact tibia assembly.

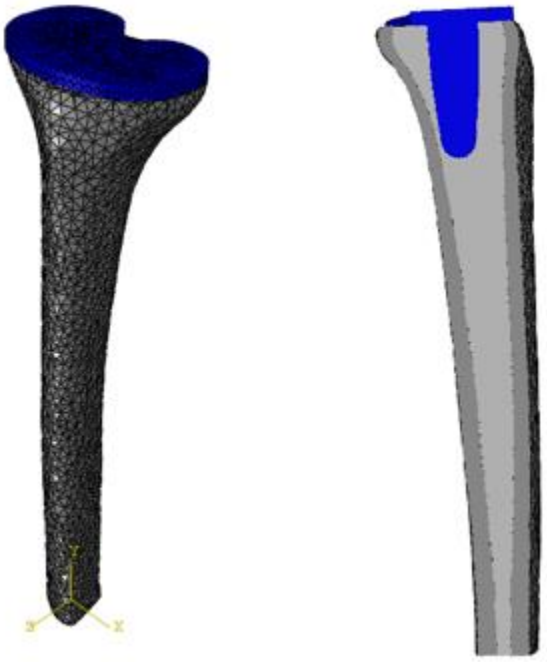

Figure 4.18: The fully-meshed resectioned tibia assembly.

### 4.5.5 Post-Processing

This model studied the implant prior to achieving osseointegration; therefore, stress shielding was only computed in trabecular bone because of its high turnover rate. Stress shielding was computed via the following equation:

$$Stress\ Shielding = \frac{Stress\ in\ Implanted\ Tibia}{Stress\ in\ Non-Implanted\ Tibia}$$

where stress shielding is reported as a ratio. A value of less than 1 is an indicator of stress shielding because the post-TKA bone experiences a decrease in stress compared to the intact tibia. Since the applied loads are purely compressive, the minimum principal stress was used as the stress measure in this study because it is the most compressive of the principal stresses.

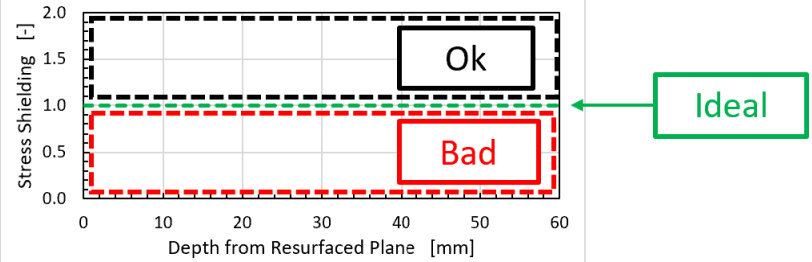


Figure 4.19: Acceptance criteria for the stress shielding response.

The intact tibial stresses were determined by creating planes of elemental sets in 10mm intervals from the resectioned plane to a depth of 70mm. Each set was further divided into anatomical regions; in total, 8 cut planes each split into 4 anatomical regions resulted in a total of 32 elemental sets. Finally, the stress values in the implanted tibia were calculated by averaging the centroidal minimum principal stress for each of the 32 elemental sets. The stress values in the implanted tibia were calculated in an identical manner.

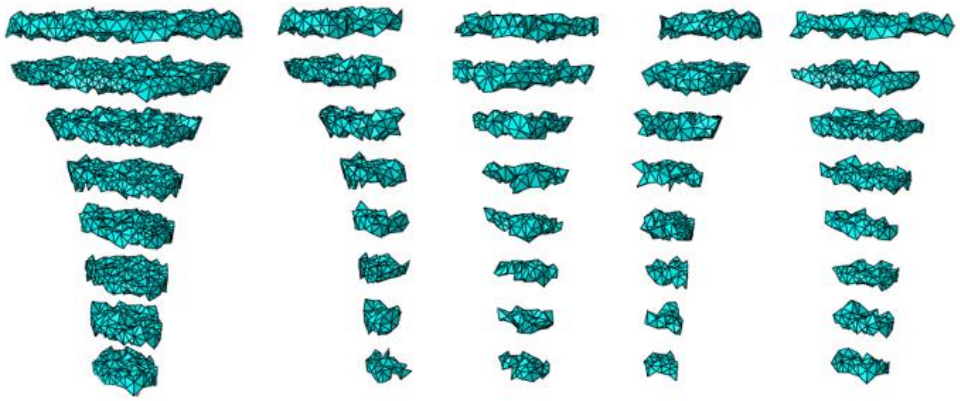

Figure 4.20: Elemental sets used to define the intact tibia stress. From left to right: elemental sets prior to being divided into anatomical quadrants; medial elemental set; posterior elemental set; lateral elemental set; anterior elemental set.

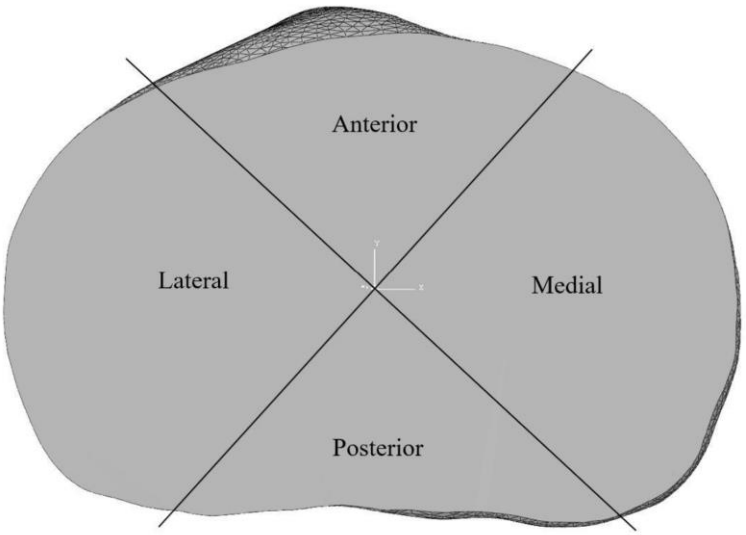


Figure 4.21: The anatomical regions of the tibia.

In addition to stress shielding, stress concentrations were also found at specific regions in bone. These regions were found as dictated by the geometry of the implant; the tip of the stem and all pegs were selected for analysis. Elemental sets were created at these regions and the minimum principal stress was computed at the centroid of each of the elements in the set and averaged.

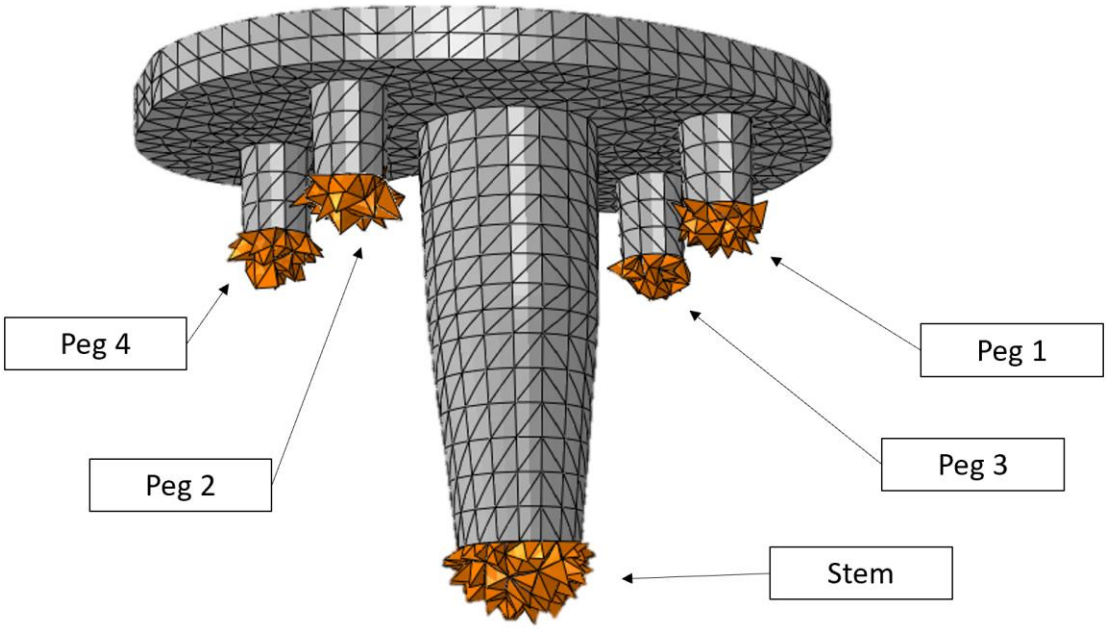


Figure 4.22: Elemental sets defined in bone (shown in orange) were used to calculate stress concentrations.

## 4.6 Configurations

A total of twenty different configurations varying the location and type of coating were constructed to analyze how the surface morphologies of cementless implants affect stress shielding. There were 4 different locations which the coating was applied; these locations were synthesized by examination of commercially available cementless implants such as the Attune, Tritanium, Persona, and others. These coatings include fully coated, partial stem, just stem, and just pegs configurations, as shown in Figure 4.23 below. Note that the red-shaded areas indicate regions of coating application.

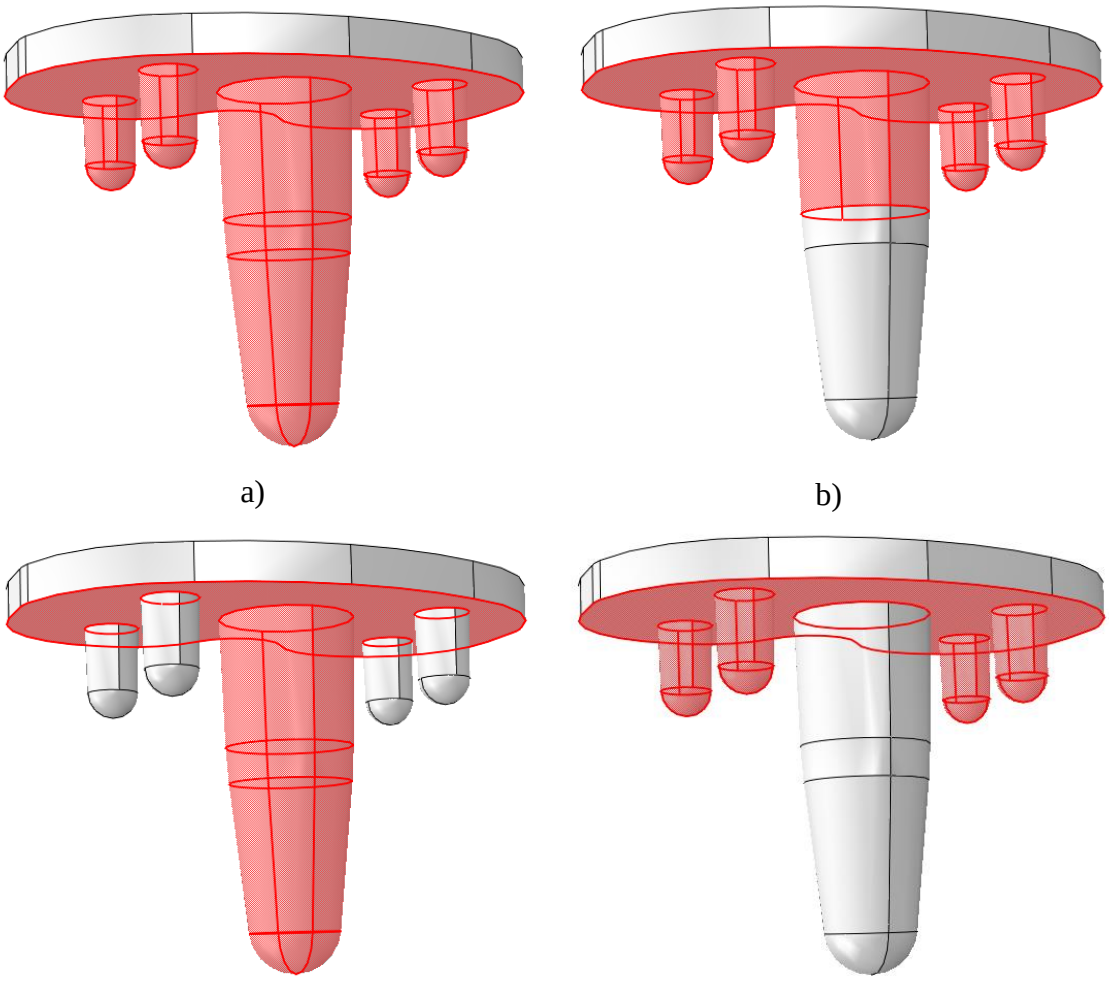


Figure 4.23: Configurations for coating location. a) fully coated, b) partial stem, c) just stem, d) just pegs.

The coated regions were assigned a coefficient of friction corresponding to a specific type of coating. Specific values of the coefficient of friction were found via a previous study by Berahmani et al. (2015). The regions without coating were assigned a coefficient of friction for uncoated titanium, or polished titanium against bone, of 0.15, as reported by Damm (2015) and rationalized previously [32]. To complete the span of the coefficients of friction, a high control coating was defined to have a coefficient of friction

of 2. A table of the values of the coefficients of friction for the types of coatings is shown in Table 4.5 below.

Table 4.5: Coefficients of Friction for Different Coating Types.

| **Description** | **Coefficient of Friction** |
|---|---|
| Uncoated | 0.15 [32] |
| Grit Blasted | 0.5 [56] |
| Porocoat | 0.95 [56] |
| DePuy Synthes Experimental | 1.4 [56] |
| High Control Coating | 2 |

All 20 configurations are described in Table 4.6 below by the coating location, coating type, and name of the configuration.

Table 4.6: List of all 20 Configurations Tested.

| Name | Coating Location | Coating Type |
|---|---|---|
| FullyUncoated | Fully Coated | Uncoated |
| FullyGritBlasted | Fully Coated | Grit Blasted |
| FullyPorocoat | Fully Coated | Porocoat |
| FullyExperimental | Fully Coated | DePuy Synthes Experimental |
| FullyHighControl | Fully Coated | High Control Coating |
| PartialUncoated | Partial Stem | Uncoated |
| PartialGritBlasted | Partial Stem | Grit Blasted |
| PartialPorocoat | Partial Stem | Porocoat |
| PartialExperimental | Partial Stem | DePuy Synthes Experimental |
| PartialHighControl | Partial Stem | High Control Coating |
| JustStemUncoated | Just Stem | Uncoated |
| JustStemGritBlasted | Just Stem | Grit Blasted |
| JustStemPorocoat | Just Stem | Porocoat |
| JustStemExperimental | Just Stem | DePuy Synthes Experimental |
| JustStemHighControl | Just Stem | High Control Coating |
| JustPegsUncoated | Just Pegs | Uncoated |
| JustPegsGritBlasted | Just Pegs | Grit Blasted |
| JustPegsPorocoat | Just Pegs | Porocoat |
| JustPegsExperimental | Just Pegs | DePuy Synthes Experimental |
| JustPegsHighControl | Just Pegs | High Control Coating |

# Chapter 5: Results

This chapter will detail the process of validating the FEM and present the results obtained. Results were broken into two parts; a 'global' analysis on stress shielding, and a 'local' analysis on the stress concentrations.

## 5.1 Validation

To validate the FEM, the intact tibial stresses were computed to a depth of 100mm and compared to values obtained in prior research. It was expected that the stress values would be different due to variations in model construction – factors such as tibial geometry, material properties, and loading conditions accounting for the variation among reported values.

Validation of this FEM was conducted by comparing the magnitude and behavior of the minimum principal stress along the length of the tibia. To account for the expected variation amongst the reported stress values, generous acceptance criteria were defined for the magnitude and the behavior. The acceptance criteria for magnitude was to be within an order of 10, and behavior to be that there were no outlying deviations. The intact tibial stress obtained for this FEM are shown in Figure 5.1 below.

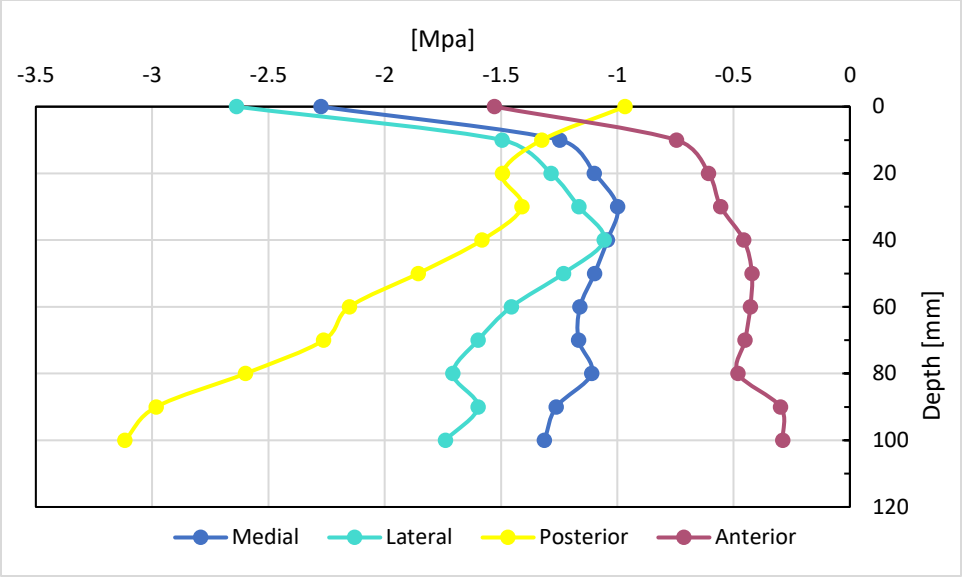


Figure 5.1: Intact tibial stress obtained for this FEM.

These stress values were compared to Completo et al.'s (2009) study due to similar bone models and outputs. Completo obtained a minimum principal stress distribution shown in Figure 5.2 below. A comparison between these plots' magnitude and behavior was deemed to satisfy the acceptance criteria for evaluation.

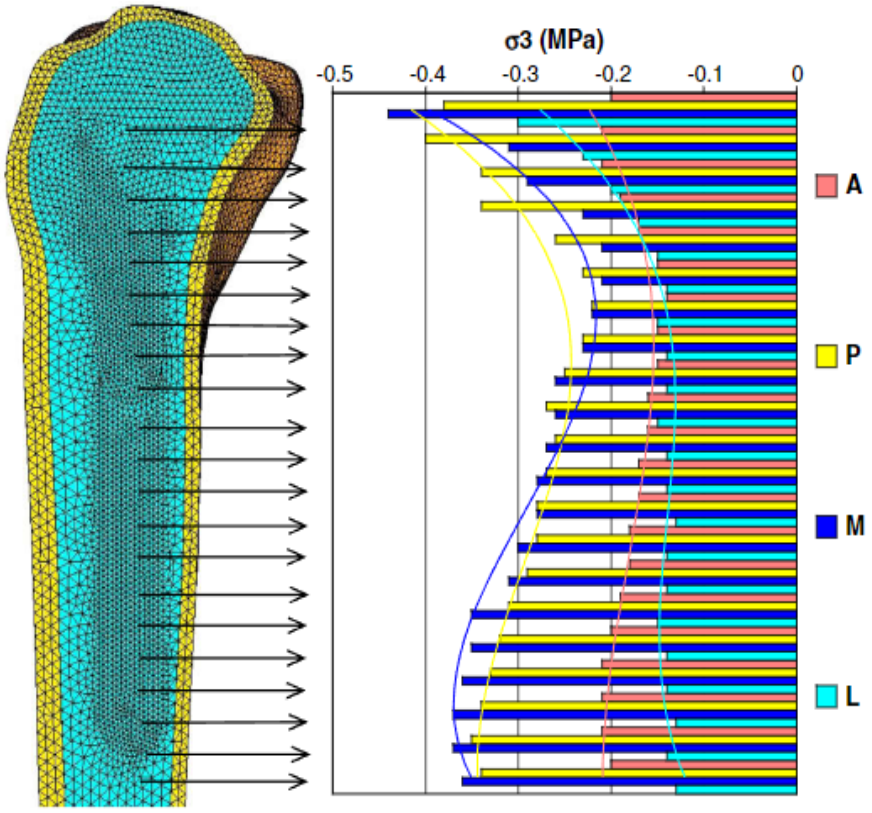


Figure 5.2: Intact stress distribution obtained by Completo et al. (2009). Note that this plot evaluates stress up to 110mm [44].

## 5.2 Results

The results are broken up into two separate analyses. First, an analysis of the entire bone-implant system was conducted to obtain the 'global' results. These results were obtained by determining stress shielding values as a function of distance from the resectioned plane in the same method used in the validation. A second analysis to obtain 'local' results analyzed the stress concentrations in specific regions of bone near distinguishing features of the implant (tip of stem and pegs). To analyze the effects of coating location and coefficient of friction, one variable was varied while the other remained constant.

### 5.2.1 Global Results: Optimal Coefficient of Friction

To determine the optimal coefficient of friction, the coating configurations were held constant as the friction varied. Figures 5.3 through 5.6 show the stress shielding in the medial compartment for different coating configurations.

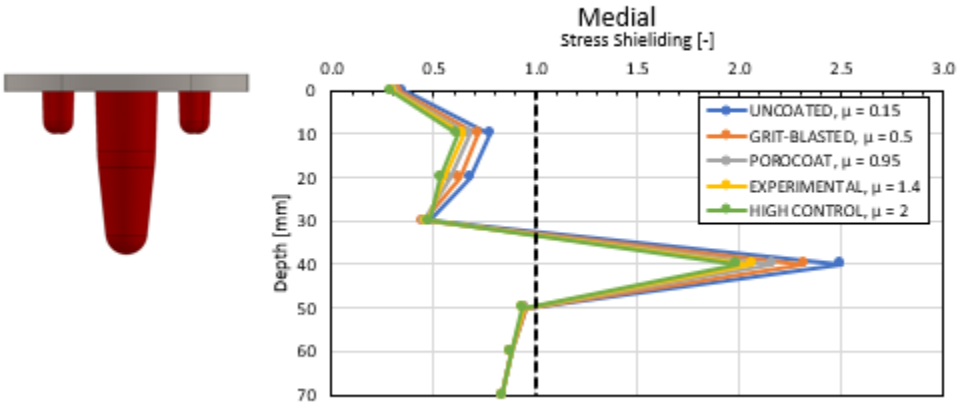


Figure 5.3: Stress shielding in the medial compartment for a fully coated implant.

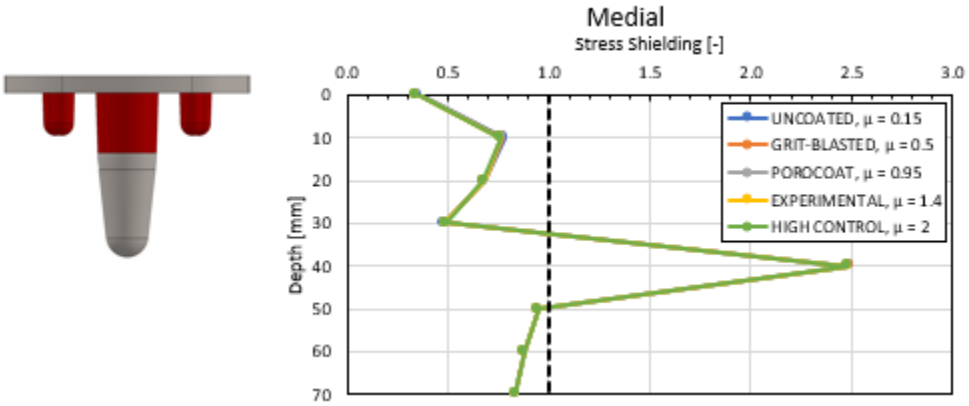


Figure 5.4: Stress shielding in the medial compartment for a partially coated implant.

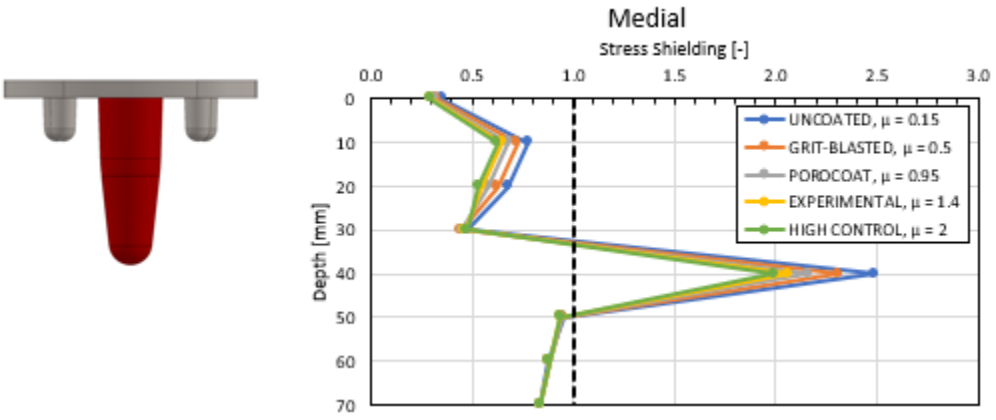


Figure 5.5: Stress shielding in the medial compartment for a just stem coated implant.

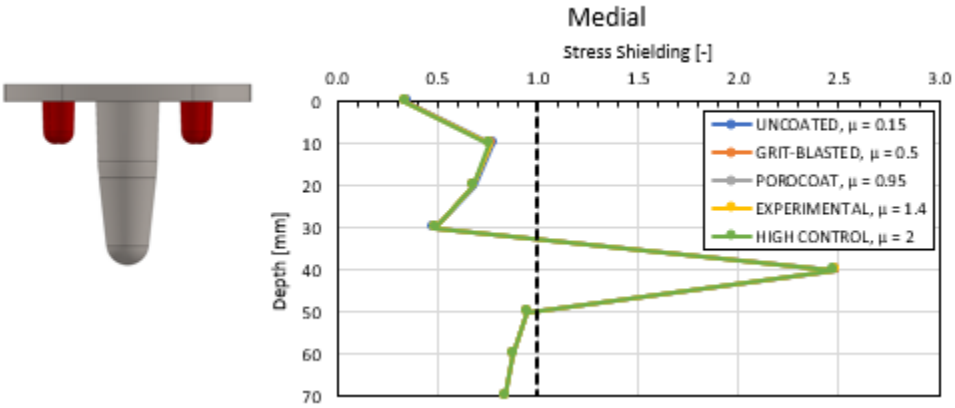


Figure 5.6: Stress shielding in the medial compartment for a just pegs coated implant.

Figures 5.3 through 5.6 indicate a high level of similarity between the fully coated and just stem configurations and the partially coated and just pegs configurations. Importantly, these results are not identical – there is slight variation amongst them in the regions in contact or proximity to the implant (depth of 0-40mm), see Figure 5.7 below.

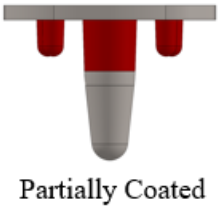


GRIT-BLASTED, μ = 0.5

| Depth [mm] | Medial Stress Shielding [-] |
|---|---|
| 0 | 0.346 |
| 10 | 0.770 |
| 20 | 0.681 |
| 30 | 0.487 |
| 40 | 2.487 |
| 50 | 0.949 |
| 60 | 0.880 |
| 70 | 0.837 |

a)


GRIT-BLASTED, μ = 0.5

| Depth [mm] | Medial Stress Shielding [-] |
|---|---|
| 0 | 0.346 |
| 10 | 0.771 |
| 20 | 0.682 |
| 30 | 0.488 |
| 40 | 2.485 |
| 50 | 0.949 |
| 60 | 0.880 |
| 70 | 0.837 |

b)

Figure 5.7: Comparison between the stress shielding values for grit-blasted a) partially coated and b) just pegs configurations.

Stress shielding is most critical when its value is less than 1 because it signals that the bone is seeing a reduction in applied forces, which can lead to bone resorption. These results demonstrate that stress shielding is most severe at depths of 0mm to 30mm from the resectioned plane.

For all configurations, stress shielding values improved with the application of decreasing values of the coefficient of friction. However, only substantial differences in stress shielding were observed in the fully coated and just stem configurations. While the partial and just pegs configurations did exhibit more favorable stress shielding values for decreasing friction coefficients, the changes in stress shielding were not appreciably different; Figure 5.8 below shows the slight difference in the stress shielding response of a just pegs coated implant.

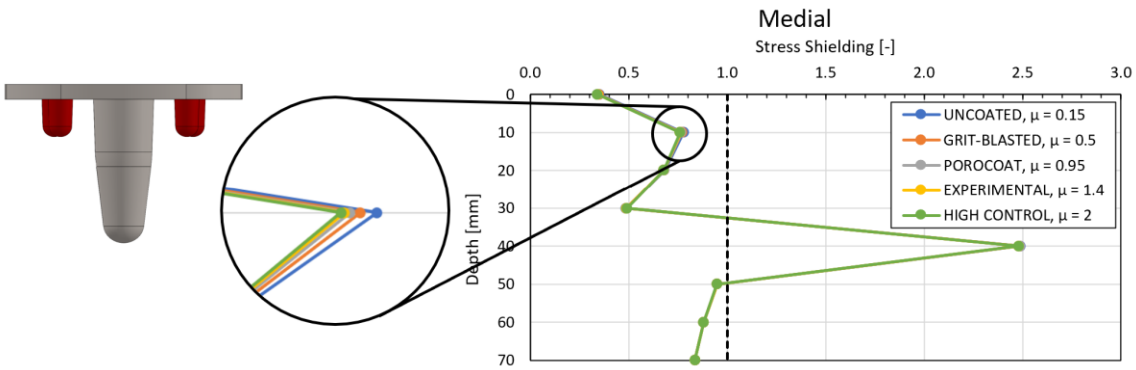


Figure 5.8: The stress shielding response of the just pegs configuration shows small differences between different friction coefficients.

The stress shielding values in the lateral, posterior, and anterior compartments displayed the same trends displayed in the medial compartment. These plots can be found in Appendix C.

### 5.2.2 Global Results: Optimal Coating Location

To determine the optimal coating location, the coefficients of friction were held constant as the coating location varied. Figures 5.9 through 5.12 show the stress shielding in the medial compartment for different coating configurations.

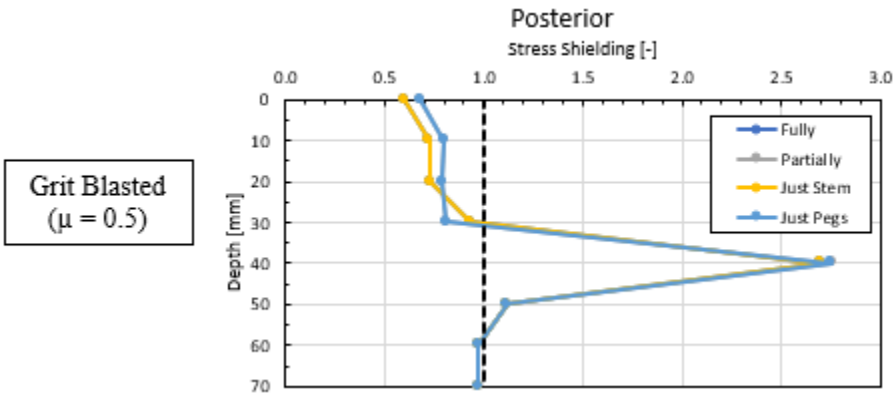


Figure 5.9: Stress shielding in the posterior compartment for a grit blasted implant.

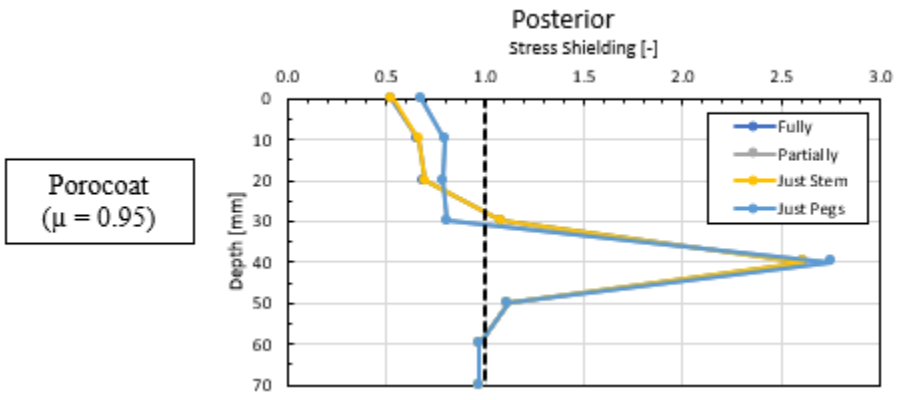


Figure 5.10: Stress shielding in the posterior compartment for an implant coated with Porocoat.

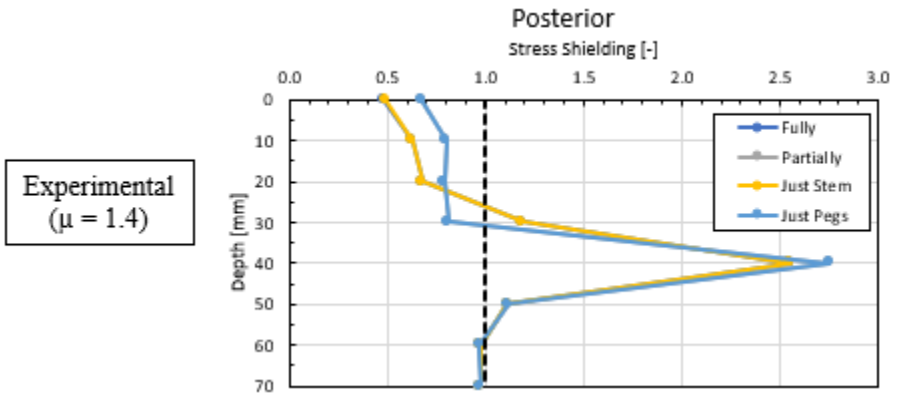


Figure 5.11: Stress shielding in the posterior compartment for an implant coated with the experimental coating.

High Control
(μ = 2)

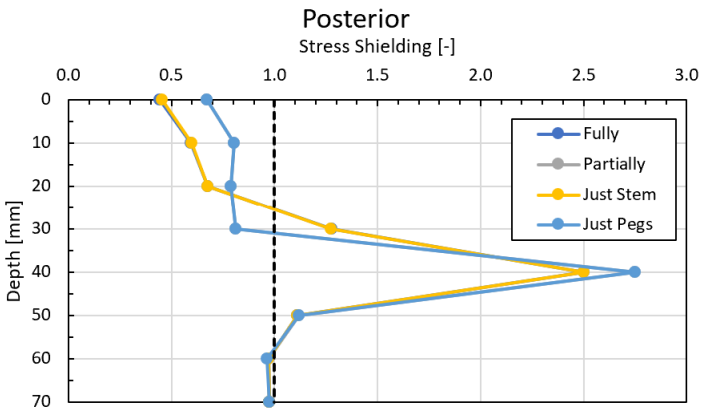


Figure 5.12: Stress shielding in the posterior compartment for an implant coated with the high control coating.

As expected with the previous results, there is a high level of similarity between the fully coated and just stem configurations, and the partially coated and just pegs configurations. The partially coated and just pegs configurations average about 15% higher stress shielding values than the fully coated and just stem configurations at depths of 0mm to 30mm, where the stress shielding phenomena is most critical. Note that the stress shielding responses of the fully coated and just stem configurations fall closer to zero as the coefficient of friction increases (grit-blasted stress shielding at a depth of 0mm is approximately 0.6; high control coated stress shielding is just less than 0.5 at a depth of 0mm, depicted in Figures 5.9 and 5.12, respectively). Thus, it is concluded that that the partially coated and just pegs configurations exhibit superior stress shielding performance, regardless of friction coefficient. Additionally, the results for optimal coating configuration displayed the same trends in all anatomical regions. Plots for the optimal coating configuration in the medial, lateral, and anterior compartments can be found in Appendix D.

### 5.2.3 Local Results: Optimal Coefficient of Friction

A comparison of the stress concentrations at the tips of the pegs and stem was conducted to determine the coefficient of friction which minimized the magnitude of the stress concentrations. Each coating location configuration was held constant as the coefficient of friction varied. Figures 5.13 through 5.16 contain the results of the stress concentrations when subjected to varying friction coefficients.

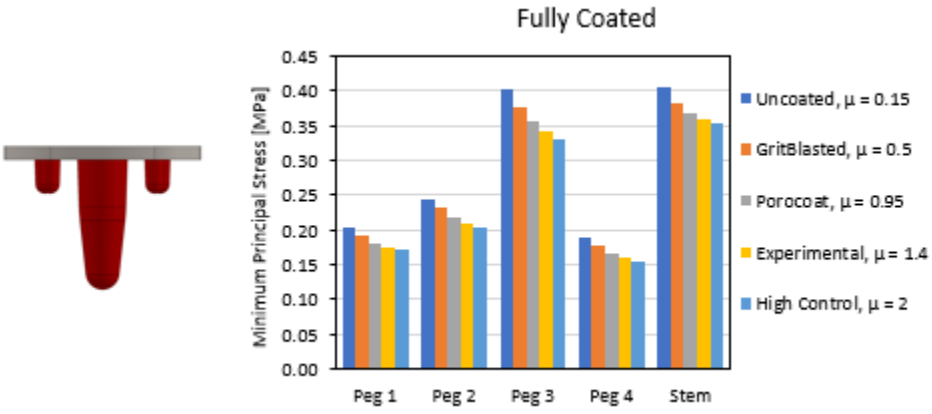


Figure 5.13: Stress concentrations for the fully coated configuration.

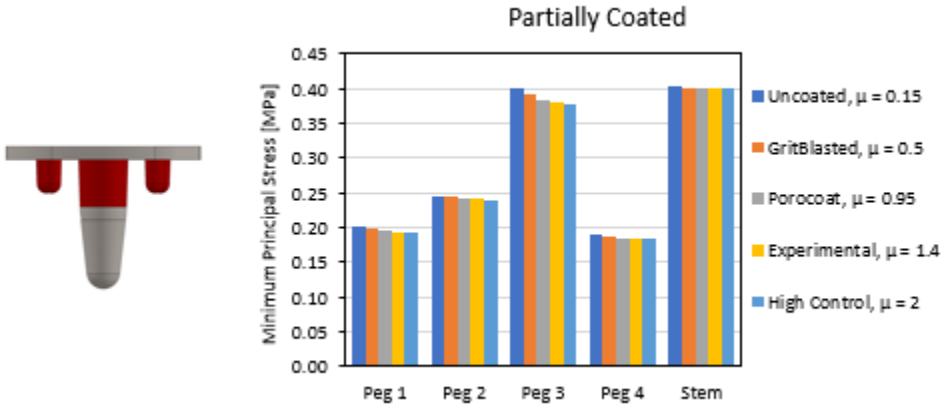


Figure 5.14: Stress concentrations for the partially coated configuration.

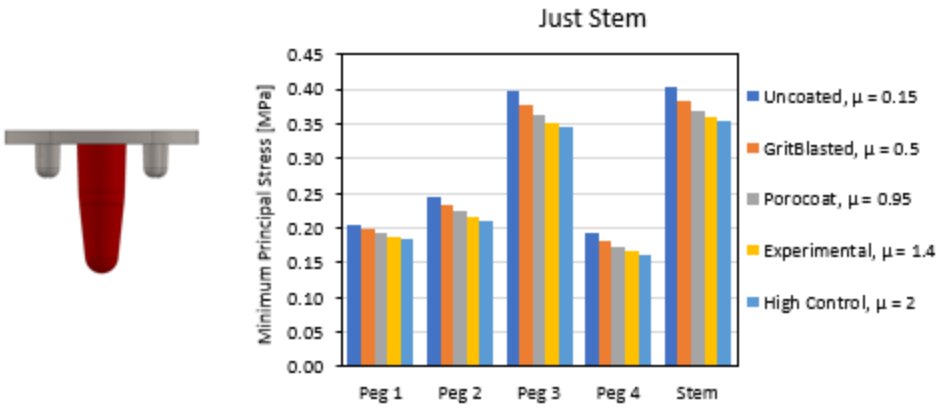


Figure 5.15: Stress concentrations for the just stem configuration.

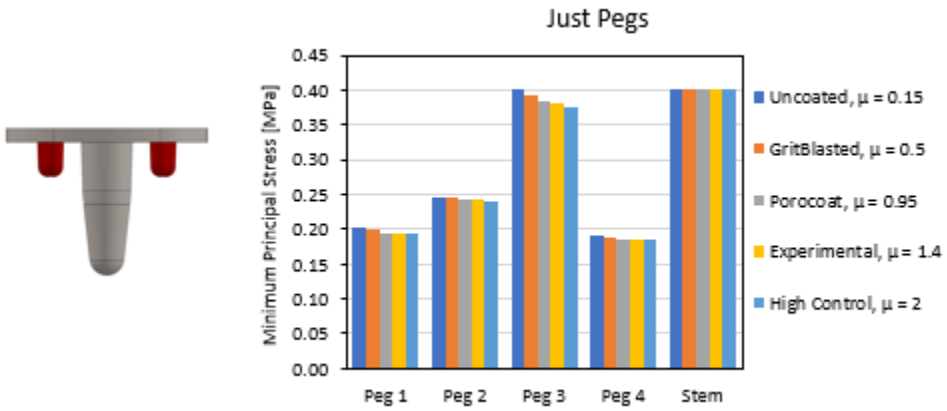


Figure 5.16: Stress concentrations for the just pegs configuration.

Across all configurations, a smaller coefficient of friction resulted in a larger magnitude of the stress concentrations. As expected from the global results, there is a high level of similarity between the fully coated and just stem configurations and the partially coated and just pegs configurations.

### 5.2.4 Local Results: Optimal Coating Location

To determine the optimal coating location which best minimized the magnitude of the stress concentrations, the coating locations were varied as the friction coefficient

remained constant. Figures 5.17 thorough 5.20 depict the stress concentration results as the coating location is varied.

Grit Blasted
(μ = 0.5)

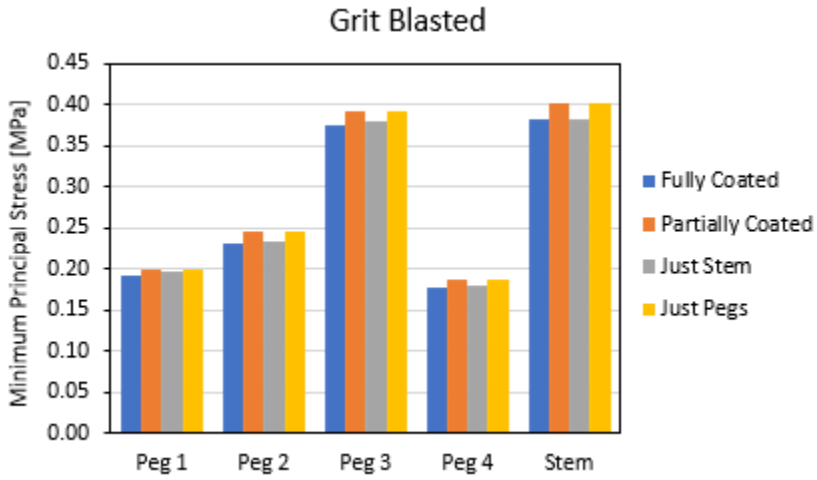


Figure 5.17: Stress concentrations for a grit blasted implant.

Porocoat
(μ = 0.95)

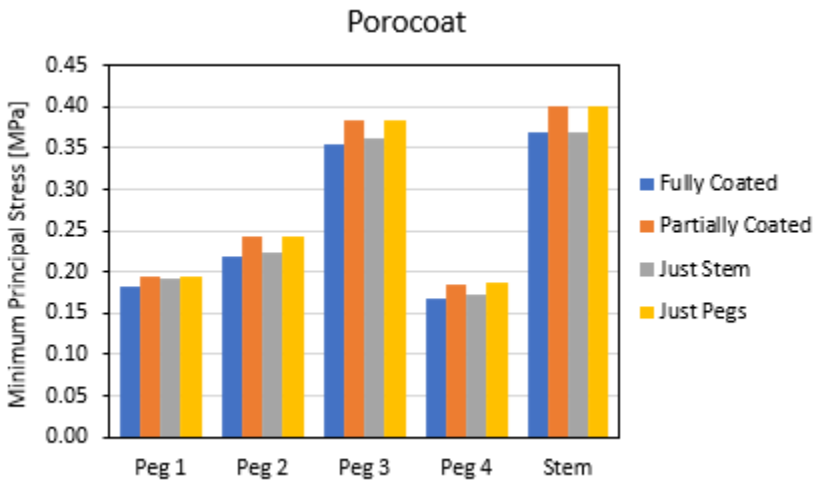


Figure 5.18: Stress concentrations for an implant coated with Porocoat.

Experimental
(μ = 1.4)

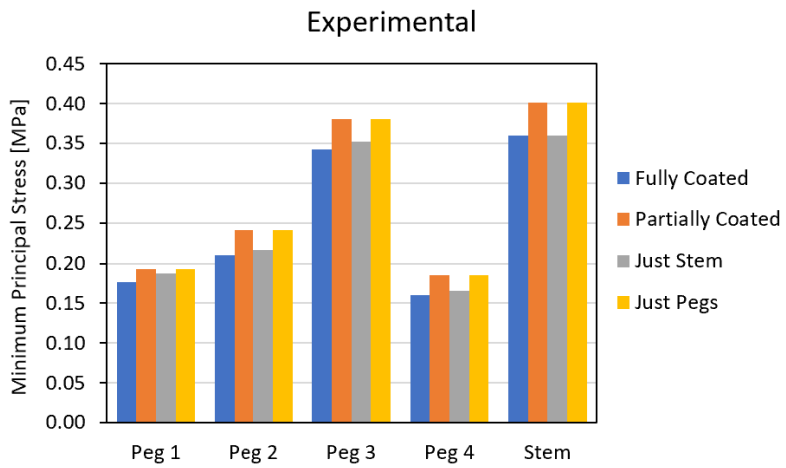


Figure 5.19: Stress concentrations for an implant coated with the experimental coating.

High Control
(μ = 2)

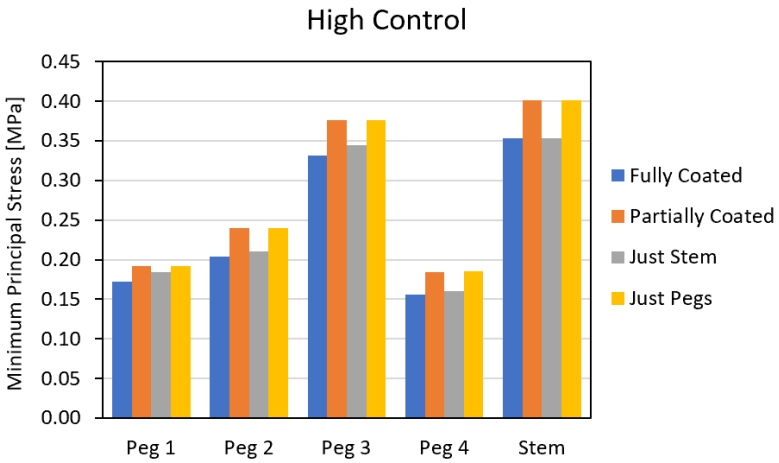


Figure 5.20: Stress concentrations for an implant coated with the high control coating.

Again, the results for the partially coated and the just pegs configurations are very similar; likewise, the results for the fully coated and just stem configurations are quite alike. Across all coefficients of friction, the partially coated and just pegs configurations exhibited smaller stress concentration magnitudes than the fully and just stem configurations.

## 5.3 Summary of Results

The global results and the local results are consistent in that the results for the pair of fully coated and just stem configurations and the pair of partially coated and just pegs configurations are nearly indistinguishable. In terms of the optimal coefficient of friction, the global results maintain that a smaller value will best mitigate stress shielding; the local results reveal that a higher coefficient of friction leads to a decrease in the magnitude of stress concentrations. As for the optimal coating location, the global results find that the partially and just pegs configurations best mitigate stress shielding; the local results found that the fully and just stem configurations correlated to a decrease in the magnitudes of the stress concentrations. On the surface, the global and local results are contradictory – this behavior will be further analyzed in the next chapter.

# Chapter 6: Discussion

This chapter will discuss and interpret the results presented. Analysis of the behavior of the configurations and comparisons between the global and local results will be conducted.

## 6.1 Interpretation and Comparison of Stress Shielding Results

The geometry of the implant greatly influences the stress shielding behavior in bone as it is the mechanism of load transfer from implant to bone. Critical geometric features of the implant utilized in this study are the pegs and stem.

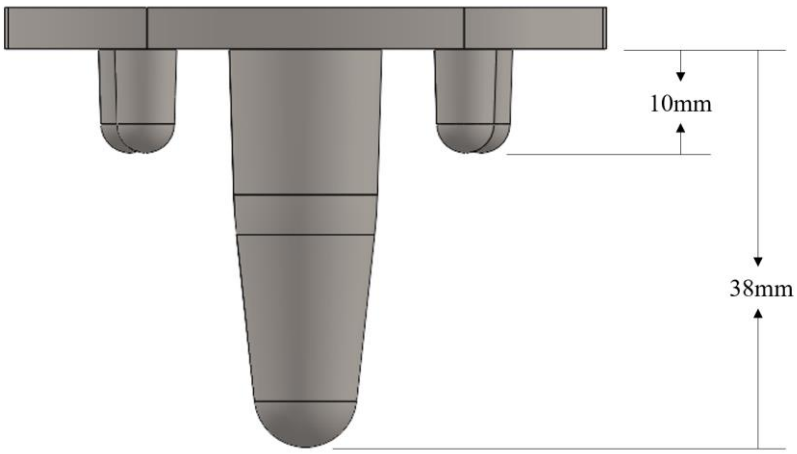


Figure 6.1: Locations of important features of the implant.

The stress shielding response across all anatomical compartments and all coating configurations is the same in regard to their behavior. For reference, Figure 6.2 below shows the stress shielding in the lateral compartment of a just pegs coated implant.

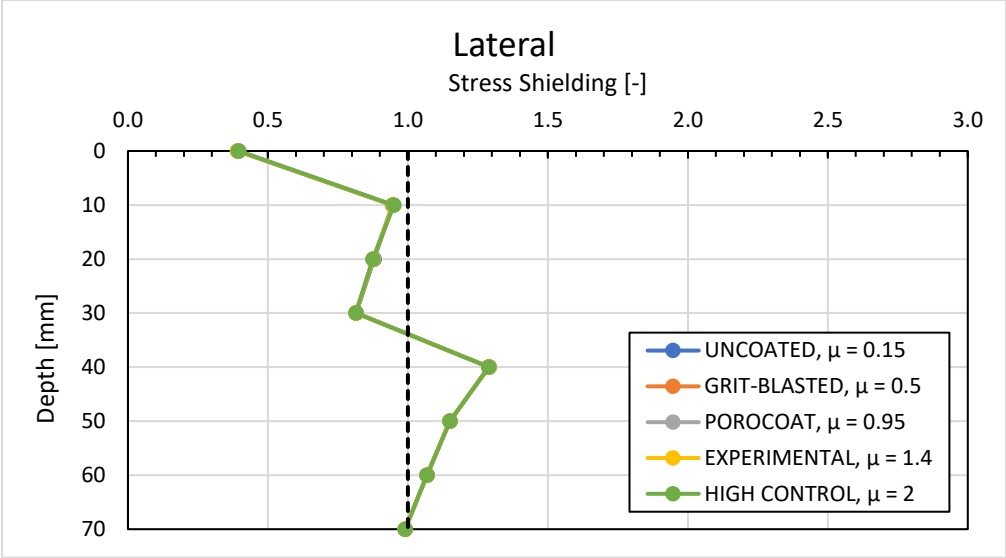


Figure 6.2: Stress shielding in the lateral compartment of a just pegs coated implant.

At the resectioned plane, stress shielding values are the most critical as the ratio is closest to zero. At a depth of 10mm, the stress shielding spikes, and then falls until it spikes again at a depth of 40mm. These spikes can be attributed to the geometry of the implant. The pegs extend to a depth of 10mm, and the stem extends to a depth of 38mm. Due to the abrupt changes in geometries, these locations produce stress concentrations. Recall that stress shielding has been defined as the ratio of stress in implanted bone to the stress in non-implanted bone; thus, the spikes in the stress shielding response can be attributed to the stress concentrations arising from the geometry of the implant.

There are many other studies which report stress shielding in tibial bone, allowing for easy comparison with the results obtained in this study. These studies similarly report the most critical stress shielding values at the resectioned plane, and spikes at the stem tip (no other referenced study used an implant with pegs). Completo et al. (2009) found that bone in proximity to the stem tip region experienced increases in stress (as compared to

non-implanted bone) no matter the length or material of the stem; additionally, Completo's study also reported the most damaging stress shielding occurred at the resectioned plane [44]. Yueh's (2020) results displayed the same behavior; critical stress shielding at the resectioned plane and spikes located at the tip of the stem [46].

## 6.2 Similarity Between Configurations

A consistent result across all analyses was the similar behavior between the fully coated and just stem configurations and the partially coated and just pegs configurations. A source of discrepancy between these configurations is the coating of the stem. The stem is entirely coated in the fully and just stem configurations, whereas in the partially and just pegs configurations, the stem is only partially coated and uncoated, respectively.

It is easier to explain why the results do not differ rather than to explain why they are similar. The stem is the feature of the implant with the largest footprint – compared to the individual pegs, its surface area is 1528mm$^2$ to 180mm$^2$. The stem is 38mm in length and displaces nearly 4800mm$^3$ of bone. Thus, due to its large surface area and prominence, the stem is the feature that dominates stress dispersion. As friction obeys $F_f = \mu N$, the specific location of the stem to experience the largest impact of friction force is where the normal forces are the largest, which is at the stem tip where the stress concentration is present. Thus, changes in stress shielding behavior are dominated by the surface morphology applied to the implant's stem tip.

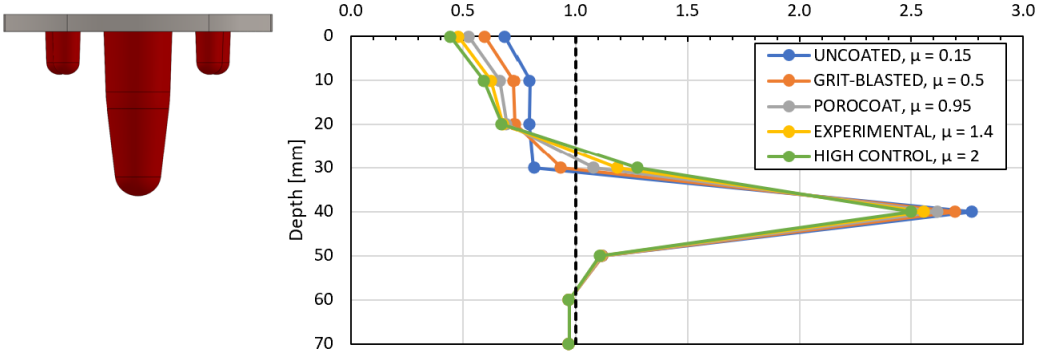


a) Fully Coated

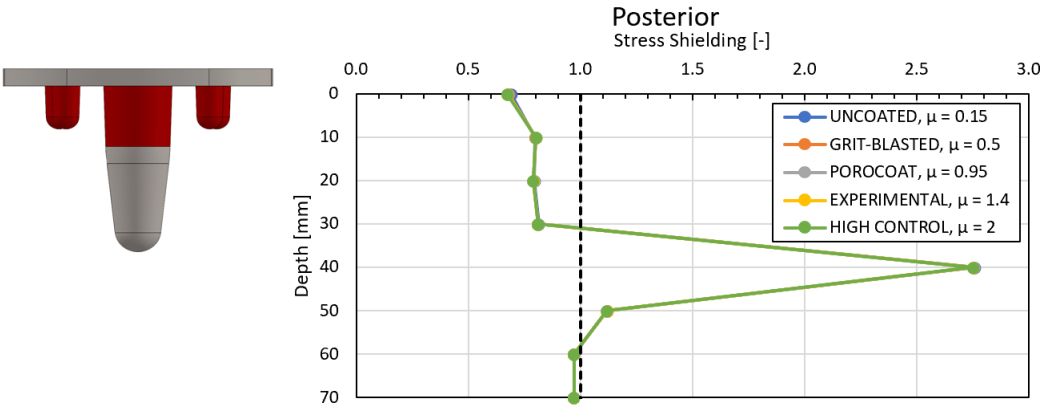


b) Partially Coated

Figure 6.3: Variation of the surface morphology applied to the stem tip. A) showed noticeable differences in the stress shielding output when compared to an implant without the stem tip coated b).

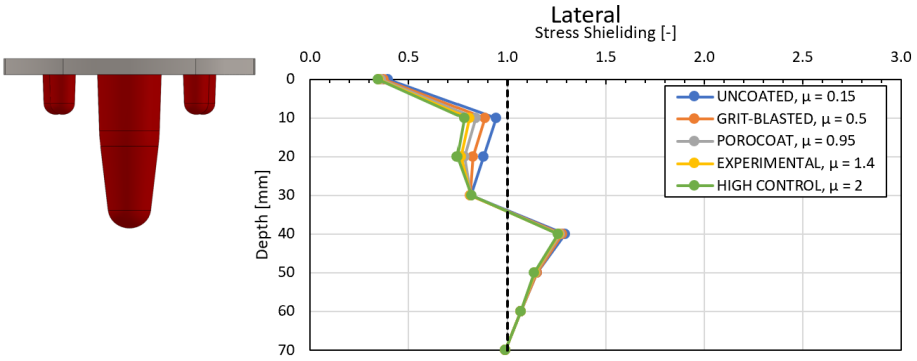


a) Fully Coated

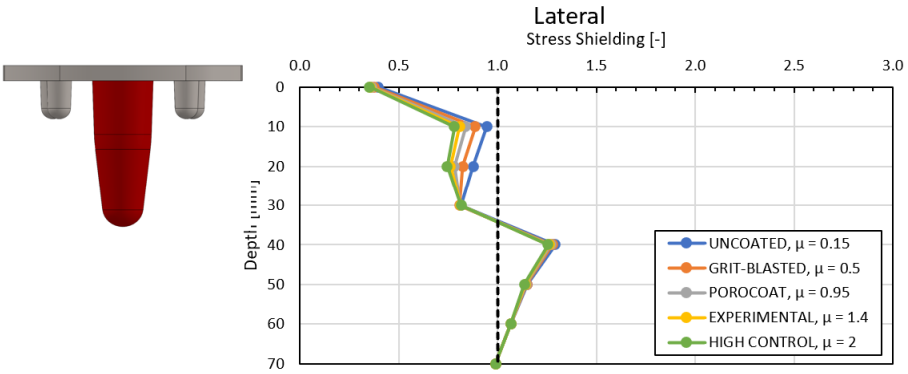


b) Just Stem

Figure 6.4: Coating of the pegs had an insignificant impact on the stress shielding response.

Figure 6.4 above shows that coating the tips of the pegs had negligible effects, as the fully coated and just stem configurations do not differ, further emphasizing that the stress distribution is dependent only on the surface morphologies applied to the tip of the stem.

## 6.3 Interpretation of Global and Local Results

Considering stress shielding's dependence on the coating of the stem tip, the fully and just stem configurations and partially and just pegs configurations display near indistinguishable results; this trend was consistent across all analyses.

At first glance, it appears that the global and local results are contradictory. First, the optimal coefficient of friction, as determined via the global results, concludes that a smaller coefficient of friction will best mitigate stress shielding; the local results find that a higher coefficient of friction leads to a decrease in the magnitude of stress concentrations.

Despite opposing conclusions about the optimal coefficient of friction, these results point to the same thing – that a smaller coefficient of friction leads to an increase in stress levels in the tibia. Regarding the global results, recall that stress shielding has been defined as the ratio of stress in implanted bone to the stress in non-implanted bone. Thus, the greater the stress shielding ratio, the greater the stresses in implanted bone. The global results find that the highest stress shielding values correlated to decreasing values of the friction coefficient. The local results find that the highest magnitude of stress concentrations are present with the lowest coefficients of friction. Thus, the global and local results agree that the smaller the coefficient of friction, the greater the compressive stress in bone.

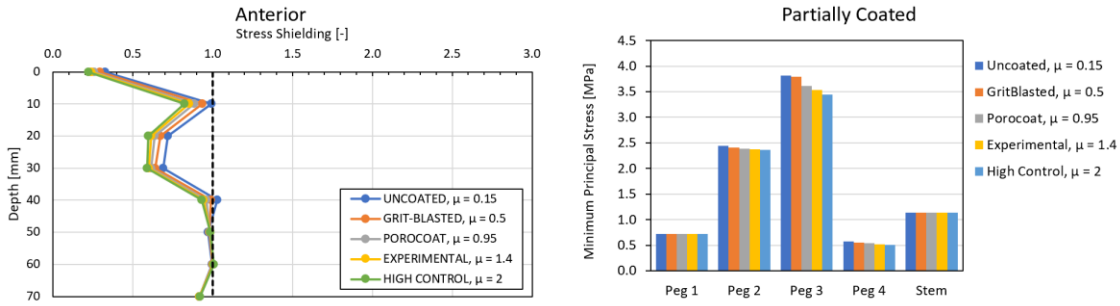


Figure 6.5: Comparison between global and local results for optimal coefficient of friction.

This is an interesting result, in part because of the method used to incorporate the coefficient of friction into the FEM. The frictional interface between implant and bone was governed by Coulomb's friction law, which states that $F_f = \mu N$, where $F_f$ is the friction force, $\mu$ is the coefficient of friction, and $N$ is the normal force. The applied force does not change across the various configurations tested; therefore, the friction force does not change across the various configurations. Considering the observed trend of decreasing friction coefficient - for Coulomb's friction law to hold, as the coefficient of friction decreases, the normal force must increase.

Apparently, lower coefficients of friction were responsible for creating higher strains on the implant surface. Higher strain values would indicate a larger outward deformation of the implant, which would be responsible for the necessary increases in the normal force.

Berahmani et al. (2015) reported higher initial compressive stresses in a femoral TKA implant coated with Porocoat ($\mu = 0.95$) than implants coated with a novel coating ($\mu = 1.4$) [65]. This finding is consistent with the findings of this study; an important side note is that that study was conducted with cadaveric femurs, providing extra credibility.

The results for the optimal coating location between the global and local results also conflicts. The global results found that the partially and just pegs configurations best mitigate the effects of stress shielding; the local results found that the fully and just stem configurations correlated to a decrease in the magnitudes of the stress concentrations. However, like the conflicting results for the coefficient of friction, the results for the optimal coating location are in agreement – that the partially coated and just pegs configurations lead to greater stress levels in the tibia.

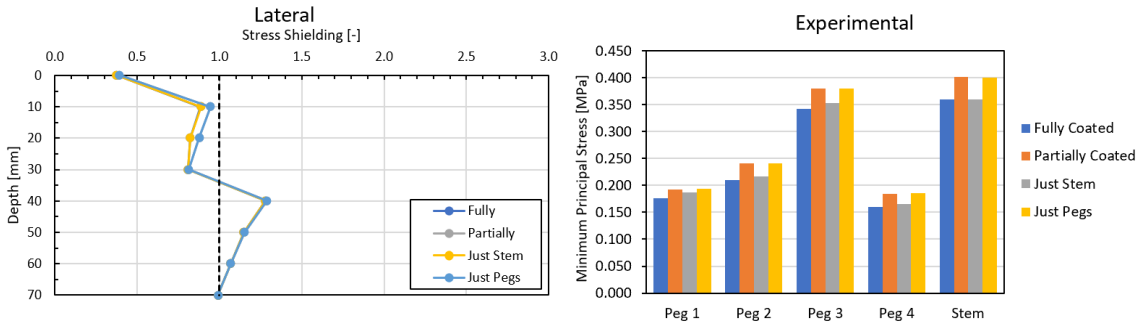


Figure 6.6: Comparison between global and local results for optimal coefficient of friction.

Interestingly, these results can be tied back into the results for similarity between the configurations and the optimal coefficient of friction. The partially coated and just pegs configurations were uncoated at the stem tip. The coefficient of friction between an uncoated titanium implant and bone is 0.15; this coefficient of friction was used to capture the uncoated bone-implant interfaces in the FEM [32]. Thus, the surface morphology at the stem tip was modeled with a friction coefficient of 0.15 for all partially coated and just pegs configurations.

Because the stem tip of the partially and just pegs configurations have the same surface morphologies, there were no significant differences in the stress shielding responses. This result is in alignment with the conclusion gathered from similarity of configurations, which found that discrepancies in the stress shielding response are dependent only on the surface morphology applied at the stem tip. The coefficient of friction applied to the stem tips for these configurations was 0.15; this is the smallest coefficient of friction included in the FEM, and it produced heightened stress values in the bone. The result is in alignment with the conclusion obtained from the analysis of the

optimal coefficient of friction, which found that lower coefficients of friction caused greater levels of stress in bone.

# Chapter 7: Conclusion

The goal of this study was to determine the optimal stress shielding response of a tibia implanted with a cementless prothesis prior to achieving secondary fixation by varying the surface morphologies applied to the implant. The surface morphologies were varied by the coefficient of friction of the coating and the location where the coating was applied. To the author's knowledge, this study is the first to analyze the effects of surface morphologies in the tibia, and by proxy, the first to analyze how surface morphologies affect stress shielding in the tibia.

## 7.1 Summary of Findings

In this study, stress shielding and stress concentrations were analyzed in a tibia implanted with a cementless tibial knee prosthesis prior to obtaining secondary fixation. It was found that stress shielding and stress concentrations are dependent on the surface morphology of the stem tip. The geometric prominence of stem tip permits the surface morphologies applied to it to dominate the stress distribution in bone. For the surface morphologies applied to the stem tip, the results find that decreasing values of the coefficient of friction caused higher compaction of the bone, which resulted in increased stress levels. The increased stress levels lead to more favorable stress shielding responses but higher magnitudes of stress concentrations.

The implications of this study should also be considered. It has been experimentally established that a higher coefficient of friction leads to better stability in primary fixation [65], [66]. The results obtained in this study suggest that a smaller coefficient of friction will mitigate the impact of the stress shielding phenomena if

applied to the stem tip. Although evaluating optimal stability is not within the scope of this study, it appears that a conclusion can be drawn regarding the stress shielding results obtained in this study and the stability results from previous literature. An implant coated with a low coefficient of friction at the stem tip and a high coefficient of friction at all other regions would be the optimal surface morphology for both primary fixation and stress shielding. Interestingly, this conclusion is in alignment with the coating applied to DePuy Synthes' Attune Knee implant, whose geometry served as the basis for the implant utilized in this study.

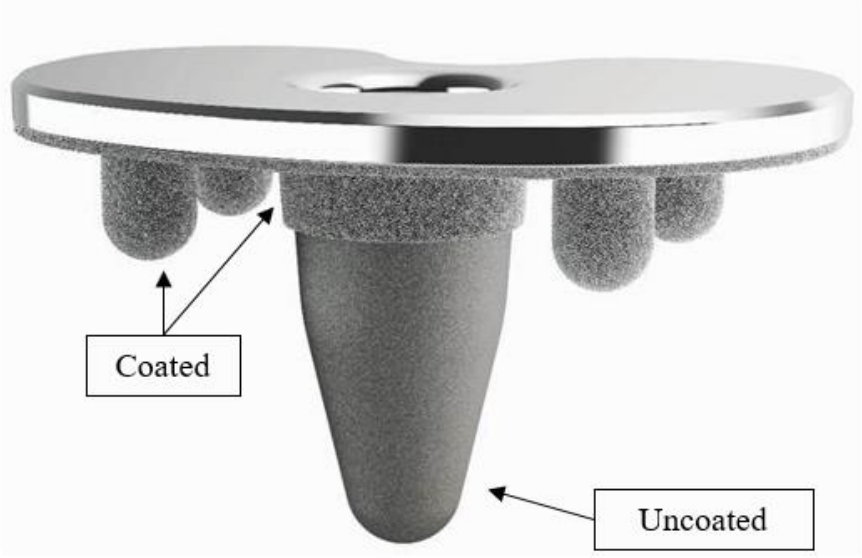


Figure 7.1: Coating locations of DePuy's Attune knee implant align with recommendations based on optimal primary fixation and stress shielding [80].

## 7.2 Limitations

Several limitations of this study exist, including the material properties of bone, the exclusion of the interference fit, the simple friction model, and assumptions regarding the implant.

This study assumed both trabecular and cortical bone to be linear elastic, isotropic, and homogeneous, a substantial deviation from the actual material properties of bone. As the measurables of stress shielding and stress concentrations are measured in bone, it is important that bone is represented as realistically as possible. Although the material properties assigned to bone are acceptable for this model, further modification to the material properties would enhance this FEM.

An interference fit between implant and bone is a critical factor in ensuring primary fixation. However, it was excluded from this FEM because it would introduce inconsistencies in the material properties assigned to the bone and produce artificially large stresses. Additionally, the exclusion of an interference fit allowed for direct comparison of the surface morphologies and their locations to the stress measurables.

Coulomb's law was used to incorporate the coefficient of friction to the FEM. This relationship distills the complex frictional relationship between the bone and implant down to a friction coefficient. A non-linear friction model may more realistically capture the interaction between bone and implant.

Finally, this study utilized a single implant design made of titanium. As the results showed, the inclusion of pegs greatly influenced the stress shielding response. The geometry of other cementless implants greatly differs, and the stress shielding response would vary accordingly. However, the differences in the stress shielding response may ultimately lead to the same conclusions reached in this study.

# REFERENCES


[1] "The Seventh Annual Report of the AJRR on Hip and Knee Arthroplasty PEEK INSIDE FOR A PREVIEW OF THE 2020 AJRR ANNUAL REPORT," 2020.

[2] C. A. Kahlenberg, B. U. Nwachukwu, A. S. McLawhorn, M. B. Cross, C. N. Cornell, and D. E. Padgett, "Patient Satisfaction After Total Knee Replacement: A Systematic Review," *HSS Journal*, vol. 14, no. 2. Springer New York LLC, pp. 192–201, Jul. 01, 2018. doi: 10.1007/s11420-018-9614-8.

[3] J. A. Singh, S. Yu, L. Chen, and J. D. Cleveland, "Rates of total joint replacement in the United States: Future projections to 2020-2040 using the national inpatient sample," *Journal of Rheumatology*, vol. 46, no. 9, pp. 1134–1140, Sep. 2019, doi: 10.3899/jrheum.170990.

[4] C. Pabinger, H. Lothaller, and A. Geissler, "Utilization rates of knee-arthroplasty in OECD countries," *Osteoarthritis Cartilage*, vol. 23, no. 10, pp. 1664–1673, Oct. 2015, doi: 10.1016/j.joca.2015.05.008.

[5] S. G. Memtsoudis, A. G. della Valle, M. C. Besculides, L. Gaber, and R. Laskin, "Trends in Demographics, Comorbidity Profiles, In-Hospital Complications and Mortality Associated With Primary Knee Arthroplasty," *Journal of Arthroplasty*, vol. 24, no. 4, pp. 518–527, Jun. 2009, doi: 10.1016/j.arth.2008.01.307.

[6] "American Joint Replacement Registry (AJRR): 2019 Annual Report," Rosement, IL, 2019.

[7] P. Fenton, S. Al-Nammari, C. Blundell, and M. Davies, “The patterns of injury and management of cuboid fractures A RETROSPECTIVE CASE SERIES,” *Bone and Joint Journal*, vol. 98B, no. 7, pp. 1003–1008, 2016, doi: 10.1302/0301-620X.98B7.

[8] E. M. Schwarz, J. Looney, and R. J. O’keefe, “Anti-TNF-α α therapy as a clinical intervention for periprosthetic osteolysis.” [Online]. Available: http://arthritis-research.com/content/2/3/165

[9] M. Bahraminasab, B. B. Sahari, K. L. Edwards, F. Farahmand, and M. Arumugam, “Aseptic loosening of femoral components - Materials engineering and design considerations,” *Mater Des*, vol. 44, pp. 155–163, 2013, doi: 10.1016/j.matdes.2012.07.066.

[10] I. B. Morrison, “THE MECHANICS OF THE KNEE JOINT IN RELATION TO NORMAL WALKING*,” Pergam~n PRSS, 1970.

[11] T. de O. Sato, G. Å. Hansson, and H. J. C. G. Coury, “Goniometer crosstalk compensation for knee joint applications,” *Sensors (Switzerland)*, vol. 10, no. 11, pp. 9994–10005, Nov. 2010, doi: 10.3390/s101109994.

[12] A. J. S. Fox, A. Bedi, and S. A. Rodeo, “The Basic Science of Human Knee Menisci: Structure, Composition, and Function,” *Sports Health*, vol. 4, no. 4, pp. 340–351, Jul. 2012, doi: 10.1177/1941738111429419.

[13] “Anatomy of the Knee,” *Comprehensive Orthopaedics*, Jul. 27, 2016. https://comportho.com/anatomy/anatomy-of-the-knee/ (accessed Jul. 26, 2022).

[14] E. A. Zimmermann and R. O. Ritchie, “Bone as a Structural Material,” *Advanced Healthcare Materials*, vol. 4, no. 9. Wiley-VCH Verlag, pp. 1287–1304, Jun. 01, 2015. doi: 10.1002/adhm.201500070.

[15] E. F. Morgan, G. U. Unnikrisnan, and A. I. Hussein, “Bone Mechanical Properties in Healthy and Diseased States,” *Annual Review of Biomedical Engineering*, vol. 20. Annual Reviews Inc., pp. 119–143, Jun. 04, 2018. doi: 10.1146/annurev-bioeng-062117-121139.

[16] N. M. B. K. Willems, G. E. J. Langenbach, V. Everts, and A. Zentner, “The microstructural and biomechanical development of the condylar bone: A review,” *European Journal of Orthodontics*, vol. 36, no. 4. Oxford University Press, pp. 479–485, 2014. doi: 10.1093/ejo/cjt093.

[17] A. Matthew Varacallo, T. David Luo, and N. A. Johanson Affiliations, “Total Knee Arthroplasty Techniques Continuing Education Activity.” [Online]. Available: https://www.ncbi.nlm.nih.gov/books/NBK499896/?report=printable

[18] “Knee Replacement Market analysis by Top Player,Report, Trends, Sales, Share, Revenue Status & Forecast Period 2017-2023,” *Medgadget*, Jun. 19, 2018. https://www.medgadget.com/2018/06/knee-replacement-market-analysis-by-top-playerreport-trends-sales-share-revenue-status-forecast-period-2017-2023.html (accessed Jul. 27, 2022).

[19] A. S. Ranawat and C. S. Ranawat, “The history of total knee arthroplasty.”

[20] “DePuy Synthes Expands ATTUNE Knee Platform with Cementless Option,” 2019. https://www.jnj.com/depuy-synthes-expands-attune-knee-platform-with-cementless-option (accessed Apr. 26, 2022).

[21] A. Postler, C. Lützner, F. Beyer, E. Tille, and J. Lützner, “Analysis of Total Knee Arthroplasty revision causes,” *BMC Musculoskelet Disord*, vol. 19, no. 1, Feb. 2018, doi: 10.1186/s12891-018-1977-y.

[22] W. B. Schrurs and G. Hannink, “Total joint arthroplasty in younger patients: heading for trouble?,” *The Lancet*, vol. 389, no. 10077, pp. 1410–1423, Apr. 2017, doi: 10.1016/S0140-6736(16)32398-4.

[23] J. H. Baek, S. C. Lee, H. Jin, J. W. Kim, H. S. Ahn, and C. H. Nam, “Poor outcomes of revision total knee arthroplasty in patients with septic loosening compared to patients with aseptic loosening,” *J Orthop Surg Res*, vol. 16, no. 1, Dec. 2021, doi: 10.1186/s13018-021-02766-y.

[24] L. E. Bayliss *et al.*, “The effect of patient age at intervention on risk of implant revision after total replacement of the hip or knee: a population-based cohort study,” *The Lancet*, vol. 389, no. 10077, pp. 1424–1430, Apr. 2017, doi: 10.1016/S0140-6736(17)30059-4.

[25] J. Julin, E. Jämsen, T. Puolakka, Y. T. Konttinen, and T. Moilanen, “Younger age increases the risk of early prosthesis failure following primary total knee replacement for osteoarthritis: A follow-up study of 32,019 total knee replacements in the Finnish Arthroplasty Register,” *Acta Orthop*, vol. 81, no. 4, pp. 413–419, Aug. 2010, doi: 10.3109/17453674.2010.501747.

[26] “Artificial Joint Replacement of the Knee.” https://eorthopod.com/artificial-joint-replacement-of-the-knee/ (accessed Nov. 04, 2022).

[27] K. B. Fricka, C. J. McAsey, and S. Sritulanondha, “To Cement or Not? Five-Year Results of a Prospective, Randomized Study Comparing Cemented vs Cementless Total Knee Arthroplasty,” *Journal of Arthroplasty*, vol. 34, no. 7, pp. S183–S187, Jul. 2019, doi: 10.1016/j.arth.2019.02.024.

[28] M. P. Ginebra, “Cements as bone repair materials,” *Bone Repair Biomaterials*, pp. 271–308, 2009, doi: 10.1533/9781845696610.2.271.

[29] E. Sánchez *et al.*, “The effect of different interference fits on the primary fixation of a cementless femoral component during experimental testing,” *J Mech Behav Biomed Mater*, vol. 113, Jan. 2021, doi: 10.1016/j.jmbbm.2020.104189.

[30] B. Eidel, A. Gote, C. P. Fritzen, A. Ohrndorf, and H. J. Christ, “Tibial implant fixation in TKA worth a revision?—how to avoid stress-shielding even for stiff metallic implants,” *https://doi.org/10.1080/10255842.2020.1830274*, vol. 24, no. 3, pp. 320–332, 2020, doi: 10.1080/10255842.2020.1830274.

[31] R. L. Purcell, E. C. Baral, S. E. Slaven, T. M. Wright, and G. H. Westrich, “Bone Ongrowth of Contemporary Cementless Tibial Components: A Retrieval Analysis,” *Arthroplast Today*, vol. 13, pp. 149–153, Feb. 2022, doi: 10.1016/j.artd.2021.12.007.

[32] N. B. Damm, M. M. Morlock, and N. E. Bishop, “Friction coefficient and effective interference at the implant-bone interface,” *J Biomech*, vol. 48, no. 12, pp. 3517–3521, Sep. 2015, doi: 10.1016/j.jbiomech.2015.07.012.

[33] Z. C. Lum, A. K. Shieh, and L. D. Dorr, “Why total knees fail-A modern perspective review,” *World Journal of Orthopedics*, vol. 9, no. 4. Baishideng Publishing Group Co, pp. 60–64, Apr. 18, 2018. doi: 10.5312/wjo.v9.i4.60.

[34] Y. Abu-Amer, I. Darwech, and J. C. Clohisy, “Aseptic loosening of total joint replacements: Mechanisms underlying osteolysis and potential therapies,” *Arthritis Research and Therapy*, vol. 9, no. SUPPL.1. Jun. 29, 2007. doi: 10.1186/ar2170.

[35] X. Zhao *et al.*, “An experimental study on stress-shielding effects of locked compression plates in fixing intact dog femur,” *J Orthop Surg Res*, vol. 16, no. 1, Dec. 2021, doi: 10.1186/s13018-021-02238-3.

[36] Q. H. Zhang, A. Cossey, and J. Tong, “Stress shielding in periprosthetic bone following a total knee replacement: Effects of implant material, design and alignment,” *Med Eng Phys*, vol. 38, no. 12, pp. 1481–1488, Dec. 2016, doi: 10.1016/j.medengphy.2016.09.018.

[37] S. M. Ott, “Cortical or Trabecular Bone: What’s the Difference?,” *American Journal of Nephrology*, vol. 47, no. 6. S. Karger AG, pp. 373–375, Jul. 01, 2018. doi: 10.1159/000489672.

[38] “Stryker Knee Implants,” 2022. https://www.stryker.com/us/en/portfolios/orthopaedics/joint-replacement/knee.html (accessed Apr. 26, 2022).

[39] “Triathlon ® Tritanium ®.” Accessed: Apr. 26, 2022. [Online]. Available: https://www.strykermeded.com/media/2971/tritan_sp_5-ssp-ca2099-triathlon-tritanium-surgical-technique.pdf

[40] S. Bhimji and R. M. Meneghini, “Micromotion of cementless tibial baseplates: Keels with adjuvant pegs offer more stability than pegs alone,” *Journal of Arthroplasty*, vol. 29, no. 7, pp. 1503–1506, 2014, doi: 10.1016/j.arth.2014.02.016.

[41] “Zimmer Biomet Commences Commercial Release of Persona® Revision Knee System”, Accessed: Apr. 26, 2022. [Online]. Available: https://investor.zimmerbiomet.com/news-and-events/news/2019/09-09-2019-120028192

[42] “Zimmer® Trabecular Metal™ Monoblock Tibial Components”, Accessed: Apr. 26, 2022. [Online]. Available: https://www.zimmerbiomet.lat/content/dam/zimmer-web/documents/en-US/pdf/medical-professionals/knee/zimmer-trabecular-metal-monoblock-tibial-components-brochure-2.pdf

[43] A. G. Au, A. B. Liggins, V. J. Raso, and A. Amirfazli, “A parametric analysis of fixation post shape in tibial knee prostheses,” *Med Eng Phys*, vol. 27, no. 2, pp. 123–134, Mar. 2005, doi: 10.1016/j.medengphy.2004.09.010.

[44] A. Completo, P. Talaia, F. Fonseca, and J. A. Simões, “Relationship of design features of stemmed tibial knee prosthesis with stress shielding and end-of-stem pain,” *Mater Des*, vol. 30, no. 4, pp. 1391–1397, Apr. 2009, doi: 10.1016/j.matdes.2008.06.071.

[45] Z. Jia, H. Gong, S. Hu, J. Fang, and R. Fan, “Influence of design features of tibial stems in total knee arthroplasty on tibial bone remodeling behaviors,” *Med Eng Phys*, vol. 48, pp. 103–113, Oct. 2017, doi: 10.1016/j.medengphy.2017.06.046.

[46] S. Yueh, “FINITE ELEMENT ANALYSIS OF TOTAL KNEE ARTHROPLASTY,” 2020.

[47] V. Baca, Z. Horak, P. Mikulenka, and V. Dzupa, “Comparison of an inhomogeneous orthotropic and isotropic material models used for FE analyses,” *Med Eng Phys*, vol. 30, no. 7, pp. 924–930, Sep. 2008, doi: 10.1016/j.medengphy.2007.12.009.

[48] J. D. Slooff, R. Huiskes, J. D. Janssen, and T. J. Slooff, “A detailed comparison of experimental and theoretical stress-analysis of a human femur Citation for published version (APA): Huiskes A DETAILED COMPARISON OF EXPERIMENTAL AND THEORETICAL STRESS-ANALYSES OF A HUMAN FEMUR.” [Online]. Available: www.tue.nl/taverne

[49] C. Anderson Engh, A. M. Young, C. A. Engh, and R. H. Hopper, “Clinical Consequences of Stress Shielding After Porous-Coated Total Hip Arthroplasty”, doi: 10.1097/01.blo.0000096825.67494.e3.

[50] F. Schmidutz, Y. Agarwal, P. E. Müller, B. Gueorguiev, R. G. Richards, and C. M. Sprecher, “Stress-shielding induced bone remodeling in cementless shoulder resurfacing arthroplasty: A finite element analysis and in vivo results,” *J Biomech*, vol. 47, no. 14, pp. 3509–3516, 2014, doi: 10.1016/j.jbiomech.2014.08.029.

[51] C. Quental, J. Folgado, P. R. Fernandes, and J. Monteiro, “Bone remodelling analysis of the humerus after a shoulder arthroplasty,” *Med Eng Phys*, vol. 34, no. 8, pp. 1132–1138, Oct. 2012, doi: 10.1016/j.medengphy.2011.12.001.

[52] S. H. Pettersen, T. S. Wik, and B. Skallerud, “Subject specific finite element analysis of stress shielding around a cementless femoral stem,” *Clinical Biomechanics*, vol. 24, no. 2, pp. 196–202, 2009, doi: 10.1016/j.clinbiomech.2008.11.003.

[53] S. Arabnejad, B. Johnston, M. Tanzer, and D. Pasini, “Fully porous 3D printed titanium femoral stem to reduce stress-shielding following total hip arthroplasty,” *Journal of Orthopaedic Research*, vol. 35, no. 8, pp. 1774–1783, Aug. 2017, doi: 10.1002/jor.23445.

[54] A. G. Au, V. James Raso, A. B. Liggins, and A. Amirfazli, “Contribution of loading conditions and material properties to stress shielding near the tibial component of total knee replacements,” *J Biomech*, vol. 40, no. 6, pp. 1410–1416, 2007, doi: 10.1016/j.jbiomech.2006.05.020.

[55] E. Sánchez *et al.*, “The effect of different interference fits on the primary fixation of a cementless femoral component during experimental testing,” *J Mech Behav Biomed Mater*, vol. 113, Jan. 2021, doi: 10.1016/j.jmbbm.2020.104189.

[56] S. Berahmani *et al.*, “An experimental study to investigate biomechanical aspects of the initial stability of press-fit implants,” *J Mech Behav Biomed Mater*, vol. 42, pp. 177–185, Feb. 2015, doi: 10.1016/j.jmbbm.2014.11.014.

[57] S. Berahmani *et al.*, “Evaluation of interference fit and bone damage of an uncemented femoral knee implant,” *Clinical Biomechanics*, vol. 51, pp. 1–9, Jan. 2018, doi: 10.1016/j.clinbiomech.2017.10.022.

[58] B. F. El-Zayat, T. J. Heyse, N. Fanciullacci, L. Labey, S. Fuchs-Winkelmann, and B. Innocenti, “Fixation techniques and stem dimensions in hinged total knee arthroplasty: a finite element study,” *Arch Orthop Trauma Surg*, vol. 136, no. 12, pp. 1741–1752, Dec. 2016, doi: 10.1007/s00402-016-2571-0.

[59] M. T. Hirschmann and W. Müller, “Complex function of the knee joint: the current understanding of the knee,” *Knee Surgery, Sports Traumatology, Arthroscopy*, vol. 23, no. 10. Springer Verlag, pp. 2780–2788, Oct. 26, 2015. doi: 10.1007/s00167-015-3619-3.

[60] J. Fang, H. Gong, L. Kong, and D. Zhu, “Simulation on the internal structure of three-dimensional proximal tibia under different mechanical environments,” 2013. [Online]. Available: http://www.biomedical-engineering-online.com/content/12/1/130

[61] D. Zhao, S. A. Banks, D. D. D’Lima, C. W. Colwell, and B. J. Fregly, “In vivo medial and lateral tibial loads during dynamic and high flexion activities,” *Journal of Orthopaedic Research*, vol. 25, no. 5, pp. 593–602, May 2007, doi: 10.1002/jor.20362.

[62] T. Fukubayashi and H. Kurosawa, “the contact area and pressure distribution pattern of the knee: A study of normal and osteoarthrotic knee joints,” *Acta Orthop*, vol. 51, no. 1–6, pp. 871–879, 1980, doi: 10.3109/17453678008990887.

[63] J.-W. Park and Y.-H. Kim, “Simultaneous cemented and cementless total knee replacement in the same patients A PROSPECTIVE COMPARISON OF LONG-TERM OUTCOMES USING AN IDENTICAL DESIGN OF NEXGEN

PROSTHESIS," *J Bone Joint Surg Br*, vol. 93, no. 11, pp. 93–1479, 2011, doi: 10.1302/0301-620X.93B11.

[64] D. Nam, C. M. Lawrie, R. Salih, C. R. Nahhas, R. L. Barrack, and R. M. Nunley, "Cemented Versus Cementless Total Knee Arthroplasty of the Same Modern Design: A Prospective, Randomized Trial," *Journal of Bone and Joint Surgery - American Volume*, vol. 101, no. 13, pp. 1185–1192, Jul. 2019, doi: 10.2106/JBJS.18.01162.

[65] S. Berahmani, D. Janssen, D. Wolfson, K. Rivard, M. de Waal Malefijt, and N. Verdonschot, "The effect of surface morphology on the primary fixation strength of uncemented femoral knee prosthesis: A cadaveric study," *Journal of Arthroplasty*, vol. 30, no. 2, pp. 300–307, Feb. 2015, doi: 10.1016/j.arth.2014.09.030.

[66] E. de Vries, E. Sánchez, D. Janssen, D. Matthews, and E. van der Heide, "Predicting friction at the bone – Implant interface in cementless total knee arthroplasty," *J Mech Behav Biomed Mater*, vol. 128, Apr. 2022, doi: 10.1016/j.jmbbm.2022.105103.

[67] C. E. Post, T. Bitter, A. Briscoe, N. Verdonschot, and D. Janssen, "A FE study on the effect of interference fit and coefficient of friction on the micromotions and interface gaps of a cementless PEEK femoral component," *J Biomech*, vol. 137, May 2022, doi: 10.1016/j.jbiomech.2022.111057.

[68] I. Bendich, C. M. Lawrie, V. Riegler, R. L. Barrack, and R. M. Nunley, "The Impact of Component Design and Fixation on Stress Shielding After Modern Total

Knee Arthroplasty," *Journal of Arthroplasty*, 2022, doi: 10.1016/j.arth.2022.01.074.

[69] "The Attune Cementless Knee System," 2019. https://www.jnjmedtech.com/sites/default/files/2020-08/107728-200106%20ATTUNE%20Cementless%20Sales%20Aid.pdf (accessed Oct. 27, 2022).

[70] J. Karjalainen, O. Riekkinen, J. Töyräs, H. Kröger, and J. Jurvelin, "Ultrasonic assessment of cortical bone thickness in vitro and in vivo," *IEEE Trans Ultrason Ferroelectr Freq Control*, vol. 55, no. 10, pp. 2191–2197, 2008, doi: 10.1109/TUFFC.918.

[71] "Surgical Technique Featuring The Attune Rotating Platform Cementless Knee," 2019. http://synthes.vo.llnwd.net/o16/LLNWMB8/INT%20Mobile/Synthes%20International/Product%20Support%20Material/legacy_DePuy_PDFs/104862.pdf (accessed Oct. 27, 2022).

[72] M. E. Berend, S. R. Small, M. A. Ritter, and C. A. Buckley, "The Effects of Bone Resection Depth and Malalignment on Strain in the Proximal Tibia After Total Knee Arthroplasty," *Journal of Arthroplasty*, vol. 25, no. 2, pp. 314–318, Feb. 2010, doi: 10.1016/j.arth.2009.01.021.

[73] J. Desmarais *et al.*, "A Short-Term Multicenter Analysis of Radiolucent Lines in a Single Uncemented Rotating Platform Implant for Total Knee Arthroplasty," *Arthroplast Today*, vol. 15, pp. 34–39, Jun. 2022, doi: 10.1016/j.artd.2022.02.011.

[74] D. E. Beverland and R. M. Nunley, “Cementless Total Knee Replacement: Guidance for Best Practices.”

[75] J.-Y. Rho, “An ultrasonic method for measuring the elastic properties of human tibia1 cortical and cancellous bone,” 1996.

[76] R. Krone and P. Schuster, “An Investigation on the Importance of Material Anisotropy in Finite-Element Modeling of the Human Femur,” 2006.

[77] “Tritanium”, Accessed: Apr. 27, 2022. [Online]. Available: https://www.stryker.com/builttofuse/

[78] S. Berahmani, D. Janssen, and N. Verdonschot, “Experimental and computational analysis of micromotions of an uncemented femoral knee implant using elastic and plastic bone material models,” *J Biomech*, vol. 61, pp. 137–143, Aug. 2017, doi: 10.1016/j.jbiomech.2017.07.023.

[79] S. C. Walpole, D. Prieto-Merino, P. Edwards, J. Cleland, G. Stevens, and I. Roberts, “The weight of nations: An estimation of adult human biomass,” *BMC Public Health*, vol. 12, no. 1, 2012, doi: 10.1186/1471-2458-12-439.

[80] D. Rumple, “‘I Designed My Knee Replacement’: Meet the Johnson & Johnson Employee Who Benefited From His Own Innovation,” Jun. 28, 2017. https://www.jnj.com/personal-stories/meet-the-johnson-and-johnson-employee-who-designed-his-own-knee-replacement (accessed Nov. 30, 2022).

## Appendix A: Intact Tibia Convergence

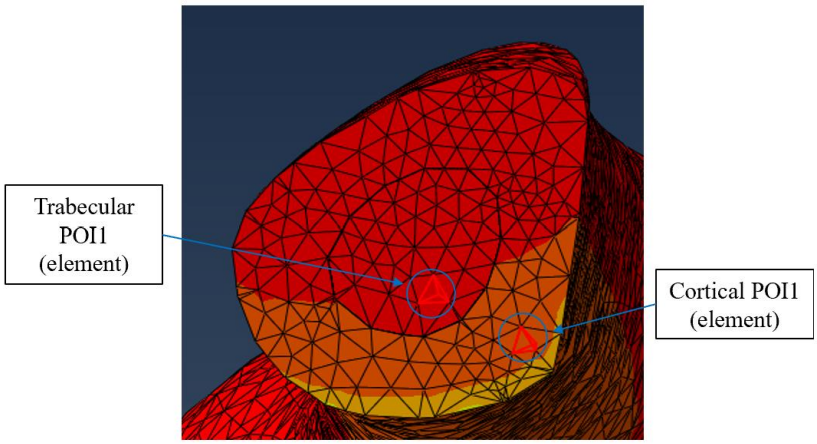
Trabecular
POI1
(element)
Cortical POI1
(element)

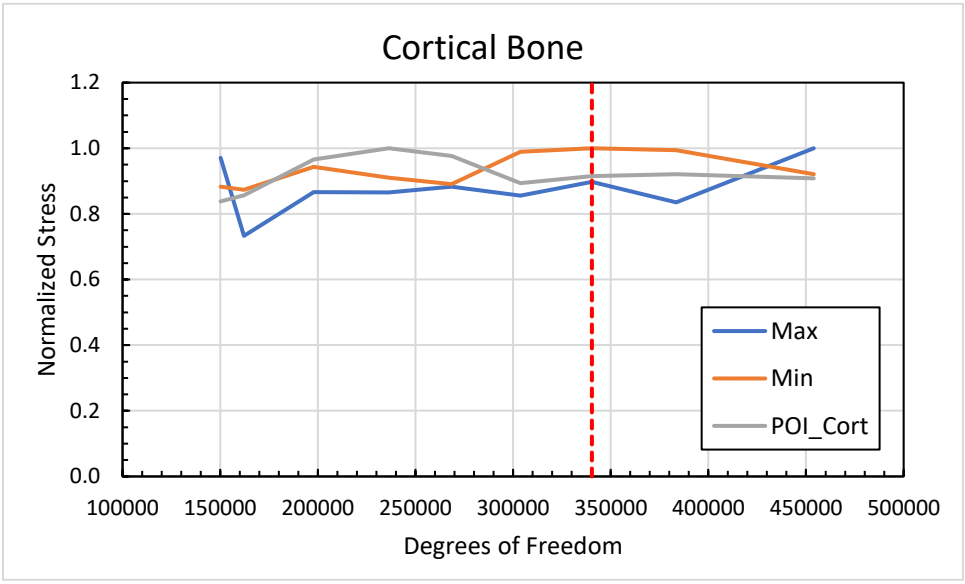
Cortical Bone
Normalized Stress
1.2
1.0
0.8
0.6
0.4
0.2
0.0
100000
150000
200000
250000
300000
350000
400000
450000
500000
Degrees of Freedom
Max
Min
POI_Cort

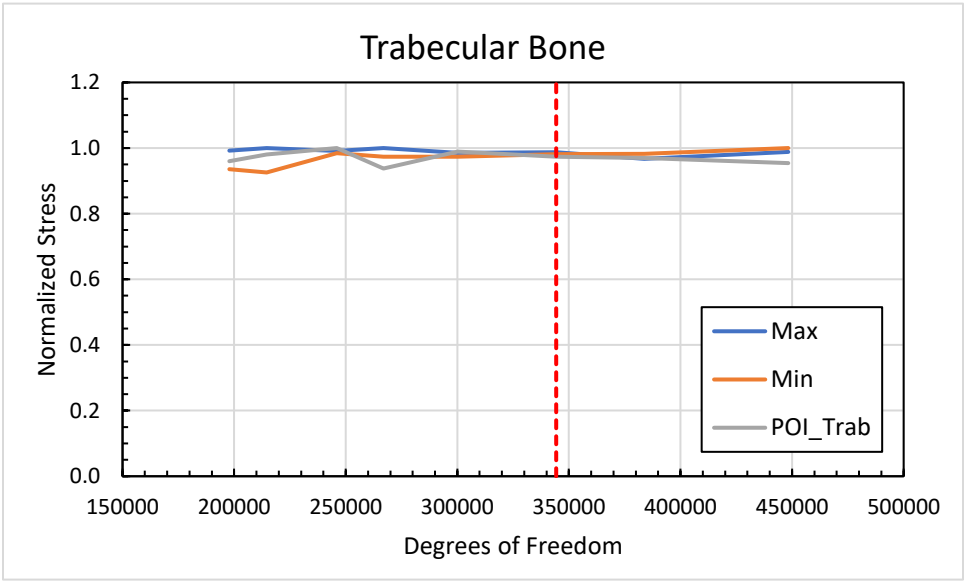
Trabecular Bone
Normalized Stress
1.2
1.0
0.8
0.6
0.4
0.2
0.0
150000
200000
250000
300000
350000
400000
450000
500000
Degrees of Freedom
Max
Min
POI_Trab

## Appendix B: Resectioned Tibia Convergence

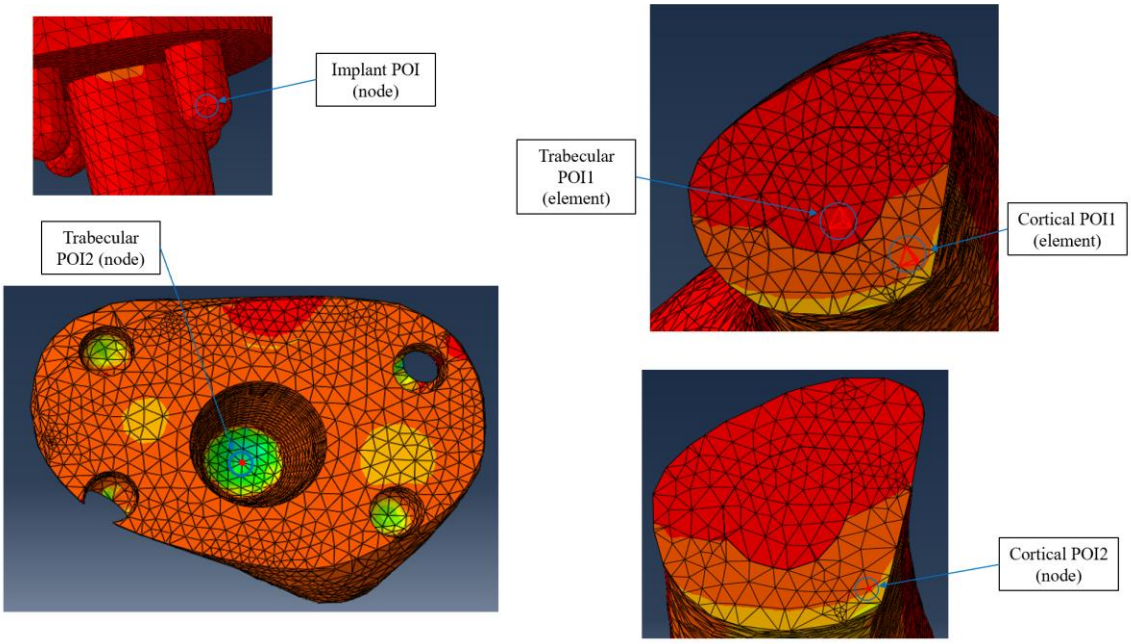


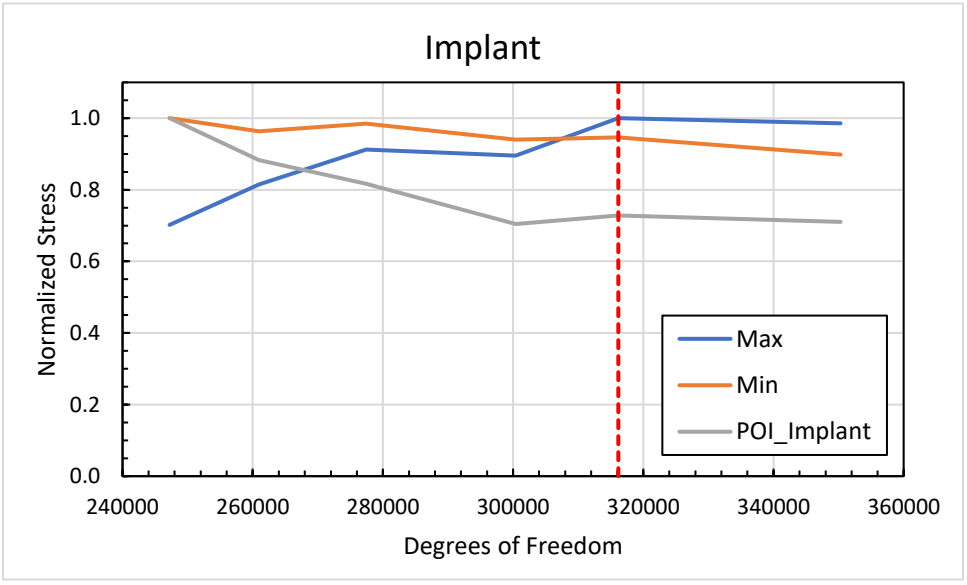

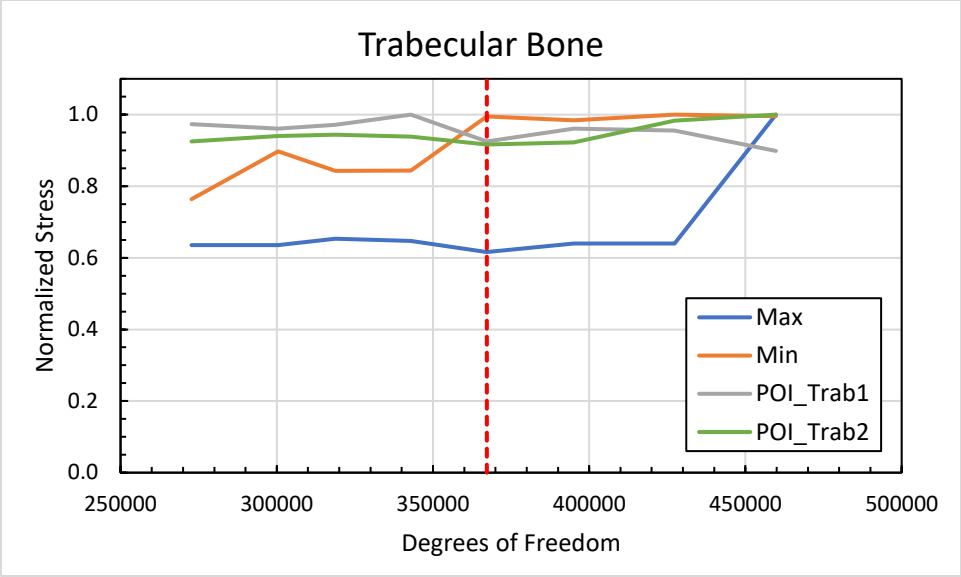
Trabecular Bone
Normalized Stress
1.0
0.8
0.6
0.4
0.2
0.0
250000
300000
350000
400000
450000
500000
Degrees of Freedom
Max
Min
POI_Trab1
POI_Trab2

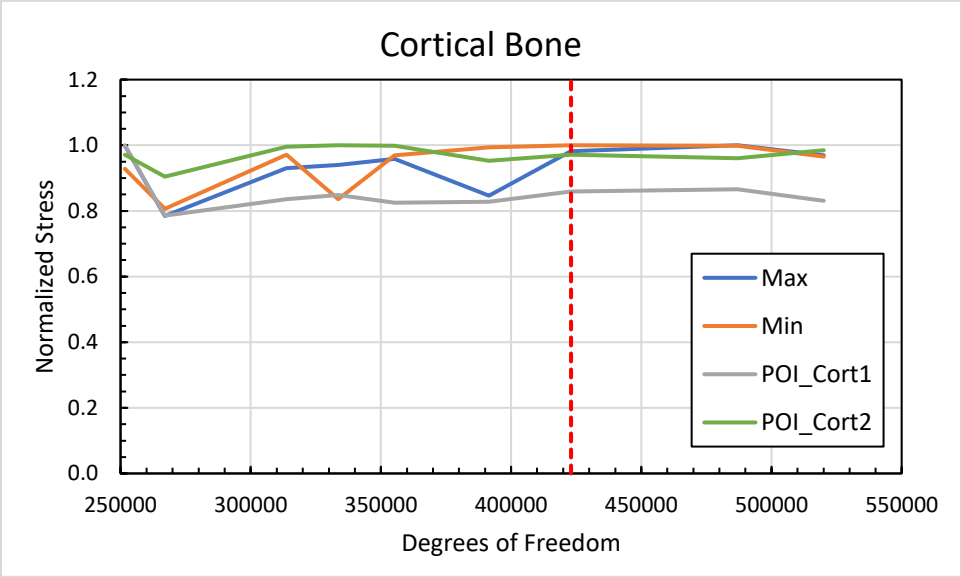
Cortical Bone
Normalized Stress
1.2
1.0
0.8
0.6
0.4
0.2
0.0
250000
300000
350000
400000
450000
500000
550000
Degrees of Freedom
Max
Min
POI_Cort1
POI_Cort2

## Appendix C: Global Results for Optimal Coefficient of Friction

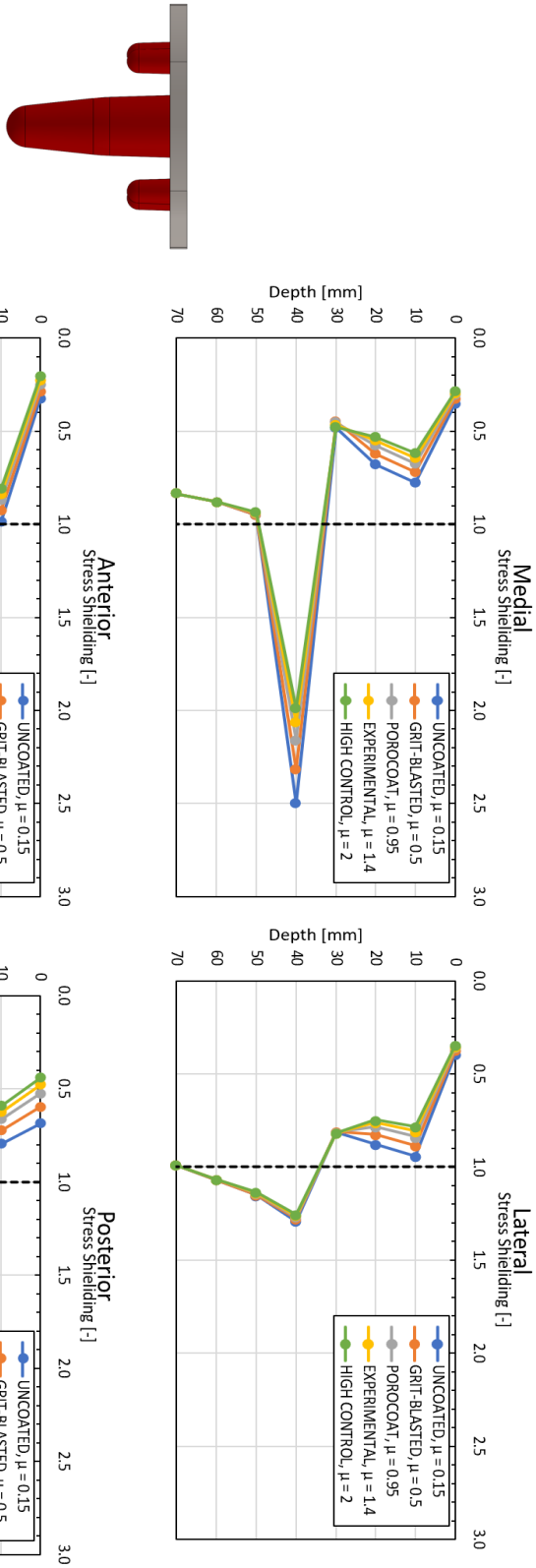

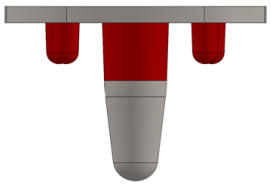

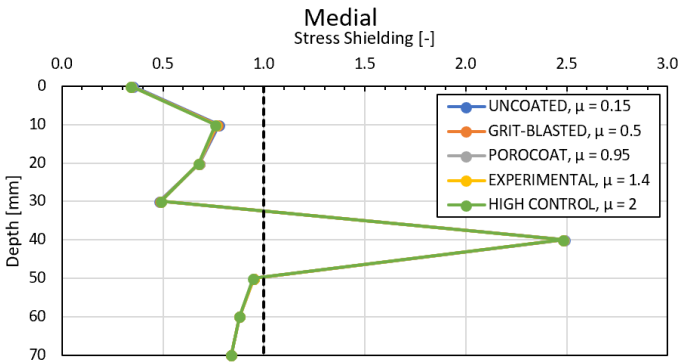
Medial
Stress Shielding [-]
0.0
0.5
1.0
1.5
2.0
2.5
3.0
0
10
20
30
40
50
60
70
Depth [mm]
UNCOATED, μ = 0.15
GRIT-BLASTED, μ = 0.5
POROCOAT, μ = 0.95
EXPERIMENTAL, μ = 1.4
HIGH CONTROL, μ = 2

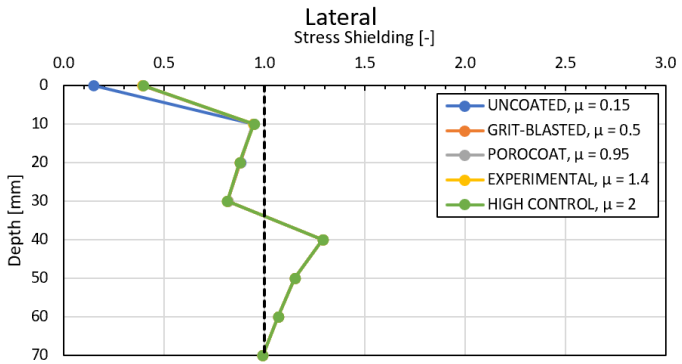
Lateral
Stress Shielding [-]
0.0
0.5
1.0
1.5
2.0
2.5
3.0
0
10
20
30
40
50
60
70
Depth [mm]
UNCOATED, μ = 0.15
GRIT-BLASTED, μ = 0.5
POROCOAT, μ = 0.95
EXPERIMENTAL, μ = 1.4
HIGH CONTROL, μ = 2

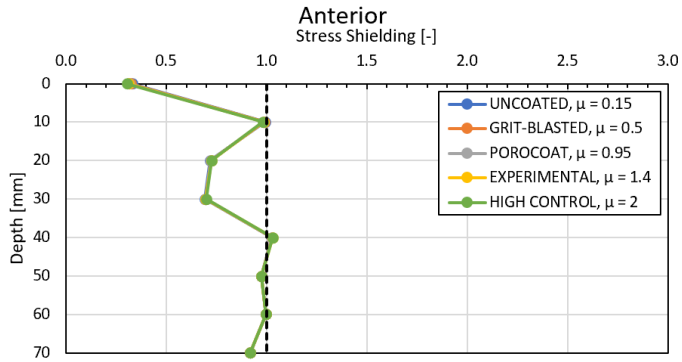
Anterior
Stress Shielding [-]
0.0
0.5
1.0
1.5
2.0
2.5
3.0
0
10
20
30
40
50
60
70
Depth [mm]
UNCOATED, μ = 0.15
GRIT-BLASTED, μ = 0.5
POROCOAT, μ = 0.95
EXPERIMENTAL, μ = 1.4
HIGH CONTROL, μ = 2

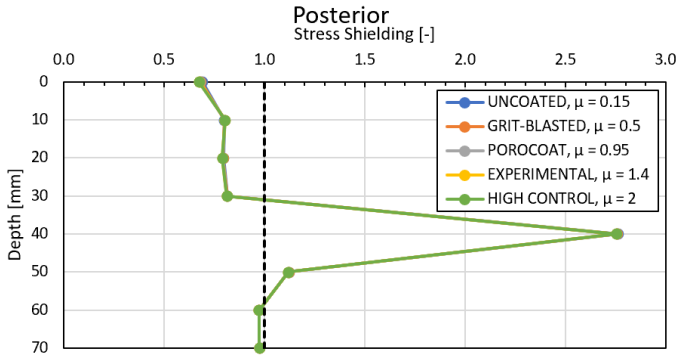
Posterior
Stress Shielding [-]
0.0
0.5
1.0
1.5
2.0
2.5
3.0
0
10
20
30
40
50
60
70
Depth [mm]
UNCOATED, μ = 0.15
GRIT-BLASTED, μ = 0.5
POROCOAT, μ = 0.95
EXPERIMENTAL, μ = 1.4
HIGH CONTROL, μ = 2

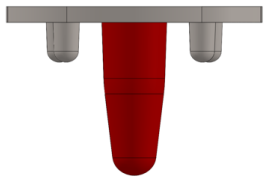

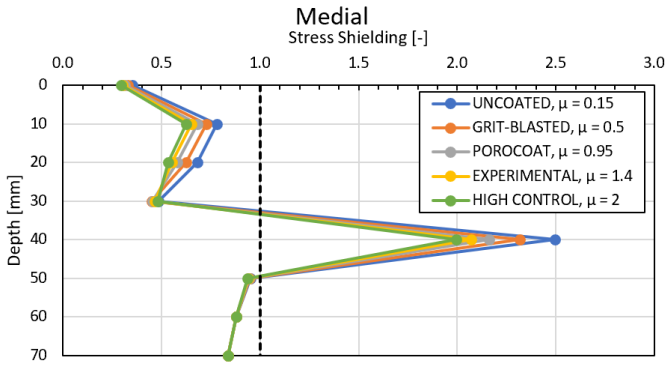
Medial
Stress Shielding [-]
Depth [mm]
UNCOATED, μ = 0.15
GRIT-BLASTED, μ = 0.5
POROCOAT, μ = 0.95
EXPERIMENTAL, μ = 1.4
HIGH CONTROL, μ = 2

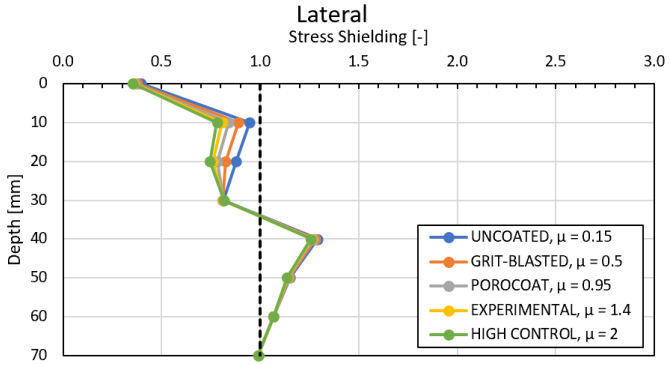
Lateral
Stress Shielding [-]
Depth [mm]
UNCOATED, μ = 0.15
GRIT-BLASTED, μ = 0.5
POROCOAT, μ = 0.95
EXPERIMENTAL, μ = 1.4
HIGH CONTROL, μ = 2

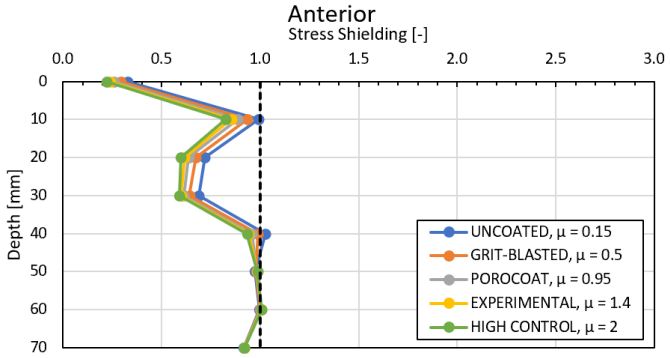
Anterior
Stress Shielding [-]
Depth [mm]
UNCOATED, μ = 0.15
GRIT-BLASTED, μ = 0.5
POROCOAT, μ = 0.95
EXPERIMENTAL, μ = 1.4
HIGH CONTROL, μ = 2

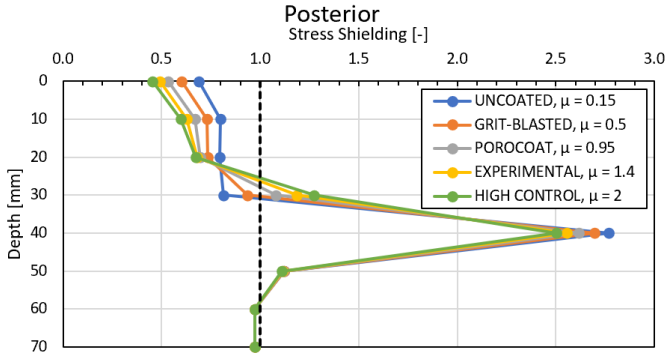
Posterior
Stress Shielding [-]
Depth [mm]
UNCOATED, μ = 0.15
GRIT-BLASTED, μ = 0.5
POROCOAT, μ = 0.95
EXPERIMENTAL, μ = 1.4
HIGH CONTROL, μ = 2

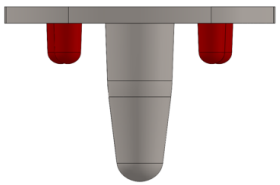

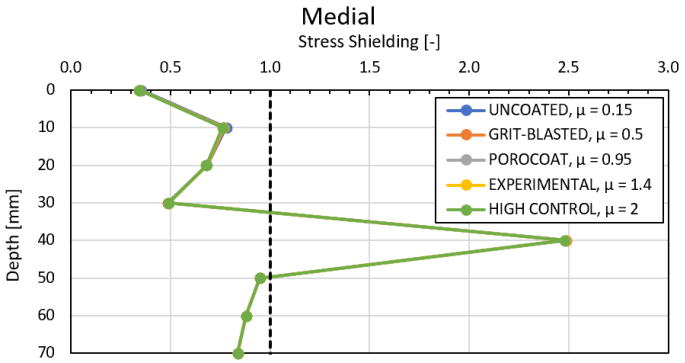
Medial
Stress Shielding [-]
0.0
0.5
1.0
1.5
2.0
2.5
3.0
0
10
20
30
40
50
60
70
Depth [mm]
UNCOATED, μ = 0.15
GRIT-BLASTED, μ = 0.5
POROCOAT, μ = 0.95
EXPERIMENTAL, μ = 1.4
HIGH CONTROL, μ = 2

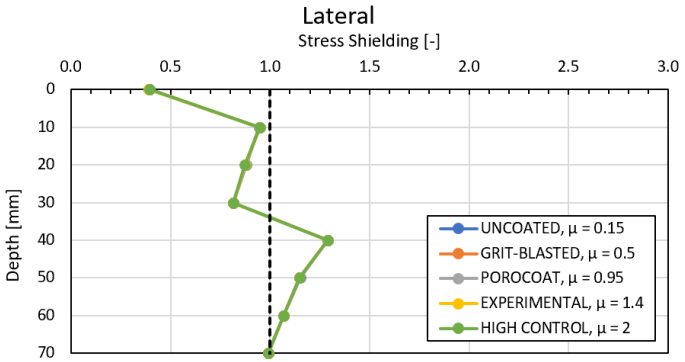
Lateral
Stress Shielding [-]
0.0
0.5
1.0
1.5
2.0
2.5
3.0
0
10
20
30
40
50
60
70
Depth [mm]
UNCOATED, μ = 0.15
GRIT-BLASTED, μ = 0.5
POROCOAT, μ = 0.95
EXPERIMENTAL, μ = 1.4
HIGH CONTROL, μ = 2

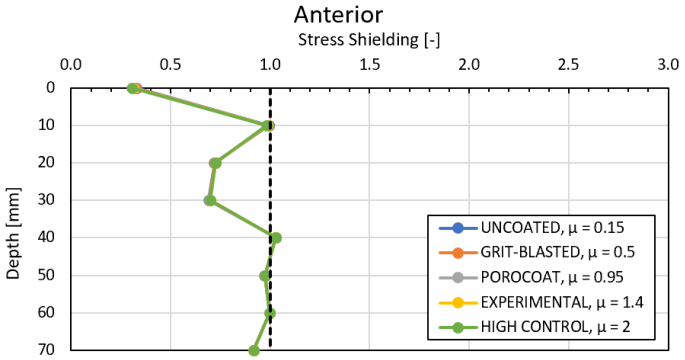
Anterior
Stress Shielding [-]
0.0
0.5
1.0
1.5
2.0
2.5
3.0
0
10
20
30
40
50
60
70
Depth [mm]
UNCOATED, μ = 0.15
GRIT-BLASTED, μ = 0.5
POROCOAT, μ = 0.95
EXPERIMENTAL, μ = 1.4
HIGH CONTROL, μ = 2

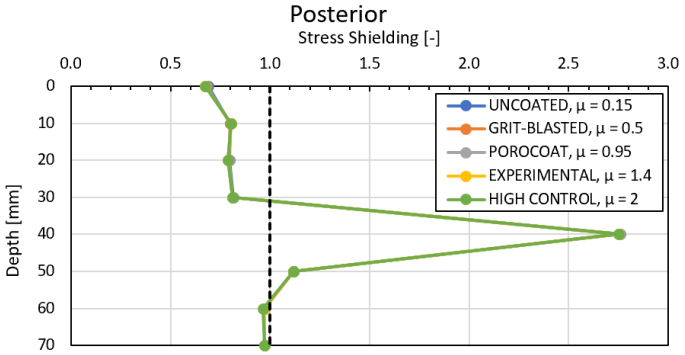
Posterior
Stress Shielding [-]
0.0
0.5
1.0
1.5
2.0
2.5
3.0
0
10
20
30
40
50
60
70
Depth [mm]
UNCOATED, μ = 0.15
GRIT-BLASTED, μ = 0.5
POROCOAT, μ = 0.95
EXPERIMENTAL, μ = 1.4
HIGH CONTROL, μ = 2

## Appendix D: Global Results for Optimal Coating Location

Grit Blasted
(μ = 0.5)

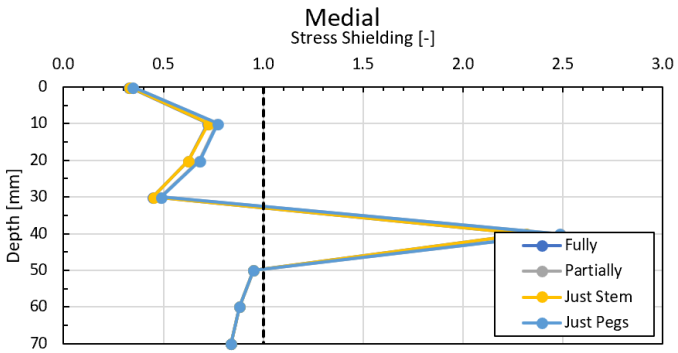


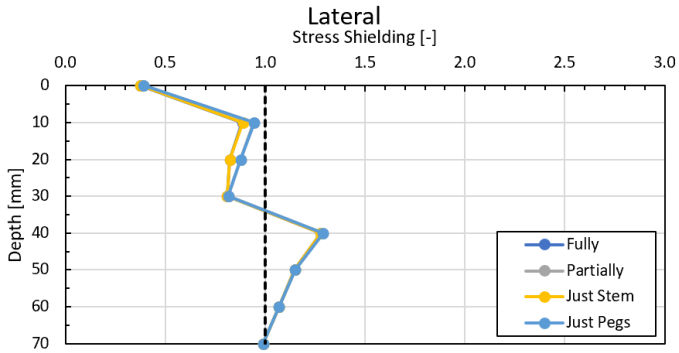


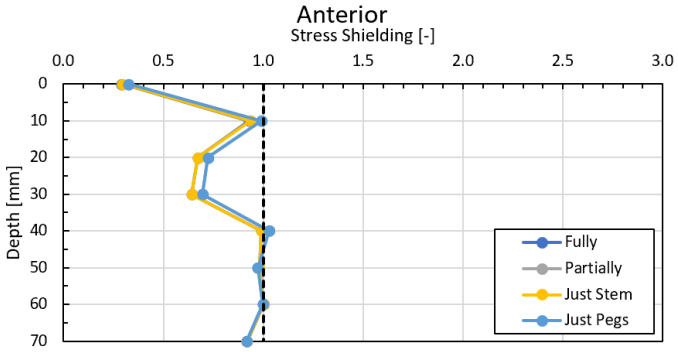


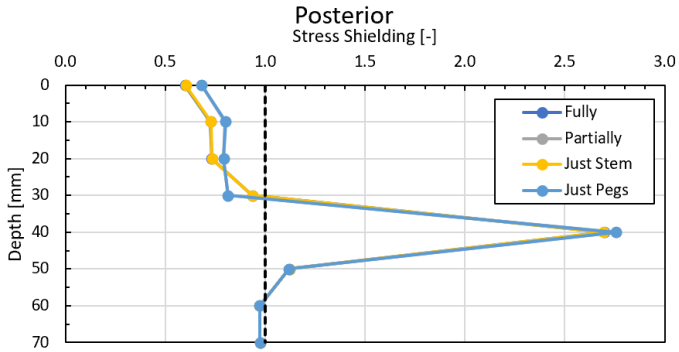

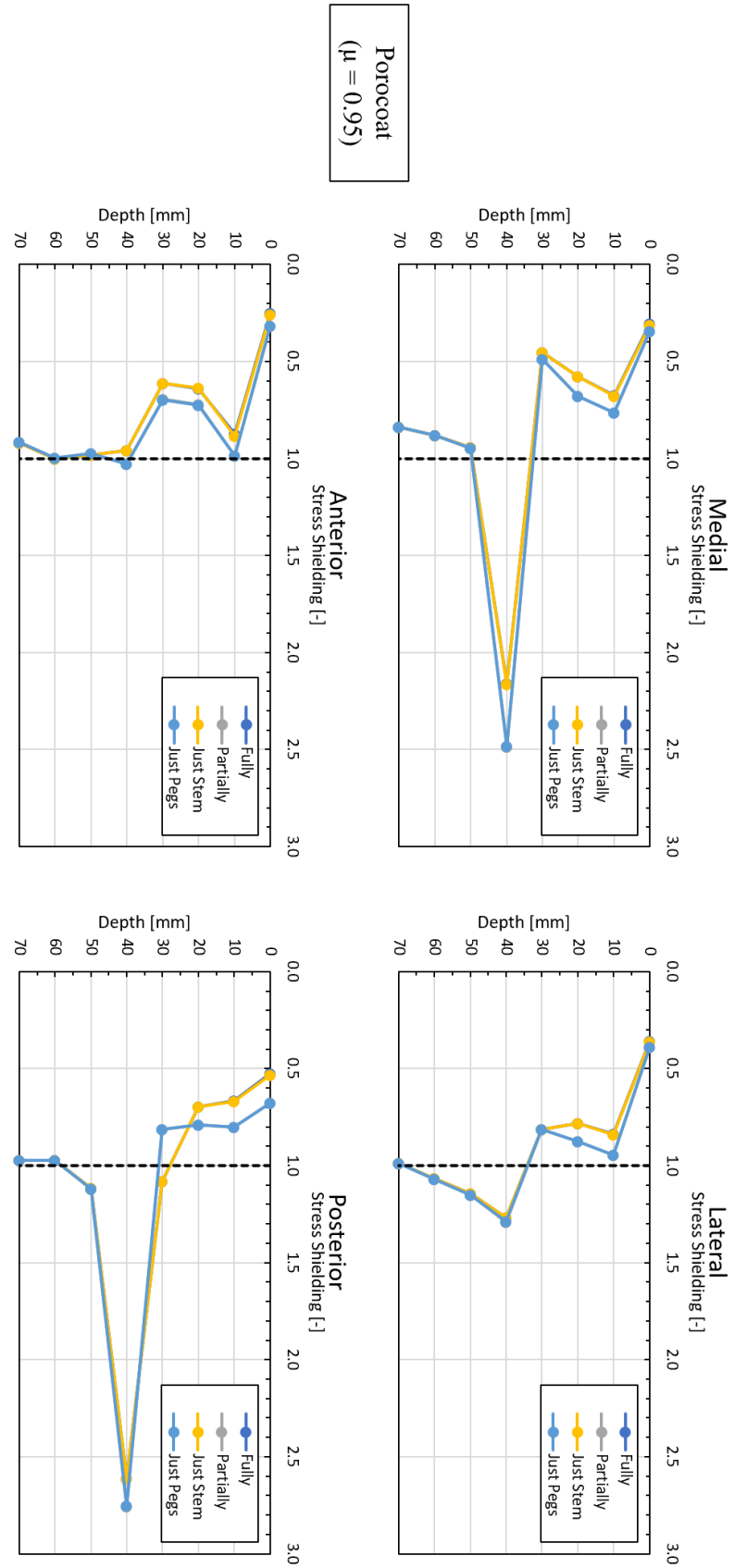
Porocoat
(μ = 0.95)
Medial
Stress Shielding [-]
Depth [mm]
Lateral
Anterior
Posterior
Fully
Partially
Just Stem
Just Pegs

Experimental
(μ = 1.4)

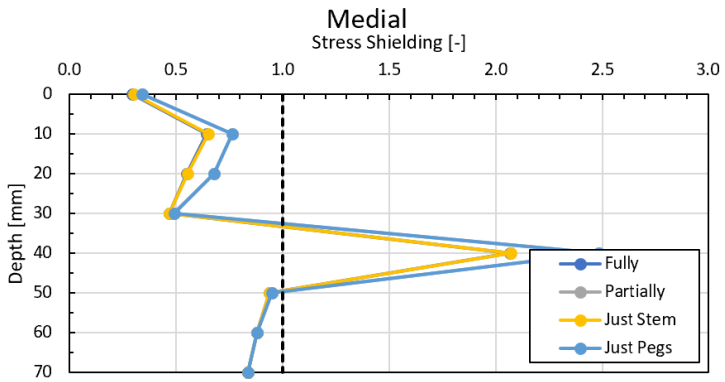


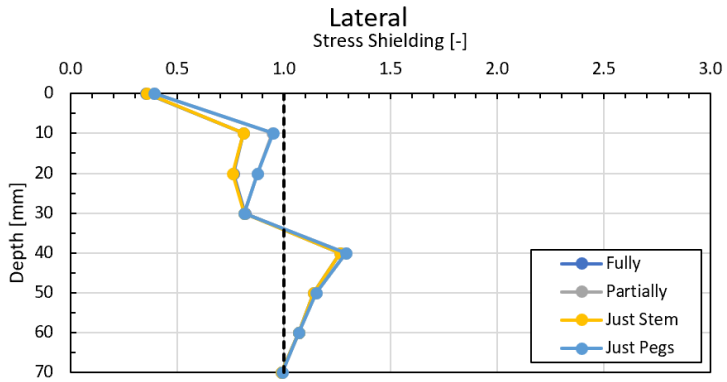


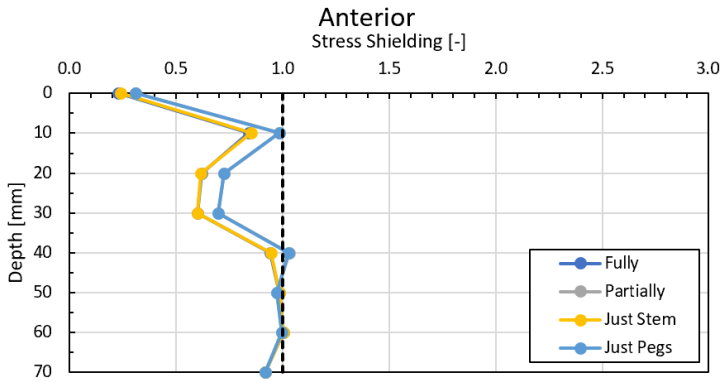


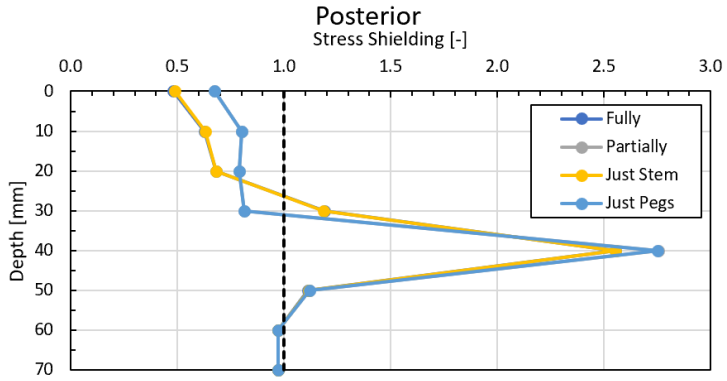

High Control
(μ = 2)